Review of Boundary Conditions and Investigation Towards the Development of a Growth Model: a Lattice Boltzmann Method Approach

Doctoral Thesis

Albert Puig Arànega

Departament d'Enginyeria Mecànica

Universitat Rovira i Virgili

Tarragona, October 2016

UNIVERSITAT ROVIRA I VIRGILI
REVIEW OF BOUNDARY CONDITIONS AND INVESTIGATION TOWARDS THE DEVELOPMENT OF A GROWTH MODEL: A LATTICE
BOLTZMANN METHOD APPROACH
Albert Puig Arànega

Review of Boundary Conditions and Investigation Towards the Development of a Growth Model: a Lattice Boltzmann Method Approach

Doctoral Thesis

Albert Puig Arànega

Supervised by:

Prof. Clara Salueña

Prof. Ildefonso Cuesta

Dr. Salvatore Cito

Departament d'Enginyeria Mecànica

Universitat Rovira i Virgili

Tarragona, October 2016

UNIVERSITAT ROVIRA I VIRGILI
REVIEW OF BOUNDARY CONDITIONS AND INVESTIGATION TOWARDS THE DEVELOPMENT OF A GROWTH MODEL: A LATTICE
BOLTZMANN METHOD APPROACH
Albert Puig Arànega

**UNIVERSITAT
ROVIRA i VIRGILI**

I STATE that the present study, entitled "Review of Boundary Conditions and Investigation Towards the Development of a Growth Model: a Lattice Boltzmann Method Approach", presented by Albert Puig Arànega for the award of the degree of Doctor, has been carried out under my supervision at the Department Mechanical Engineering of Universitat Rovira i Virgili.

Tarragona, 11 July, 2016

Prof. Clara Salueña   Prof. Ildefonso Cuesta   Dr. Salvatore Cito

UNIVERSITAT ROVIRA I VIRGILI
REVIEW OF BOUNDARY CONDITIONS AND INVESTIGATION TOWARDS THE DEVELOPMENT OF A GROWTH MODEL: A LATTICE
BOLTZMANN METHOD APPROACH
Albert Puig Arànega

Agraïments

M'agradaria començar donant les gràcies als supervisors de la meva tesi. Al Dr. Ildefonso Cuesta, per escollir-me i per guiar-me sobretot durant la primera etapa de la tesi. Al Dr. Salvatore Cito, ja que va ser una gran incorporació i va ser el responsable d'introduir-me en el món de l'hemodinàmica. Considero que m'ha enriquit molt tant en l'àmbit acadèmic com en l'àmbit personal. I a la Dra. Clara Salueña, la qual li agraeixo profundament tota la dedicació, atenció i paciència que ha tingut amb mi.

Vull també agrair el suport del Departament d'Enginyeria Mecànica de la Universitat Rovira i Virgili, i particularment del grup de recerca *Experiments, Computation and Modelization in Fluid Mechanics and Turbulence* ('ECoMMFiT'). A ells els dec la beca predoctoral i la possibilitat d'enriquir la meva experiència acadèmica.

A tots els col·legues de doctorat o ja doctorats, per tots els bons moments passats. A Jonathan, per les llargues i productives converses i pel seu esperit crític. A Javi, per acompanyar-me durant tot el doctorat en el tema de LBM.

Als integrants del *ilustrísimo club de caballeros*: Javi, Valen, Irene, Maria, Noe i David els quals vull fer menció especial a aquest últim per ser un company i amfitrió immillorables.

Als col·legues de Riudoms i de la carrera, per estar sempre allà.

A la meva família, en especial als meus pares, que sempre m'han recolzat i animat en els moments més difícils. Sense ells no hauria pogut arribar fins aquí.

A la meva amiga i parella, Elena. Ets la meva inspiració i raó principal de la meva felicitat.

I finalment, als membres del tribunal per acceptar, avaluar i participar en la cloenda de la tesi.

REVIEW OF BOUNDARY CONDITIONS AND INVESTIGATION TOWARDS THE DEVELOPMENT OF A GROWTH MODEL: A LATTICE
BOLTZMANN METHOD APPROACH
Albert Puig Arànega

Abstract

The lattice Boltzmann method (LBM) is a computational fluid dynamics technique that is rapidly earning popularity due to its inherent properties: it deals with complex geometries with relative ease, it is computationally easy to implement and it can be effectively used with massive parallel computing tools. This features make the lattice Boltzmann method a powerful alternative to be considered in many applications –porous media, hemodynamics, multiphase flows, etc. However, the method is still not entirely established in the scientific community due to its relatively late appearance. In addition, the method is still under the development of new features and is in constant evolution. One known topic that is still under active research are the boundary conditions: some of them will be reviewed and analysed in this thesis.

On the other hand, the method also is known to be restrained in several ways. For example, the method is limited to deal with low Mach numbers (Ma < 0.3). The method is isothermal, and hence, it is limited only to low temperature variations. The passive scalar transport model presents also restrictions to high Schmidt/Prandtl numbers, as the scales of the hydrodynamic and passive scalar transport events can be of different orders of magnitude, which at some extent can demand unfeasible amounts of computational resources. While there are other techniques and methods that can be coupled with the LBM to appease such problems, there is not much information about the actual limits of the applicability of the LBM passive scalar model for high Schmidt problems. A good scenario to test the extent of the limitations that arise from a multi-scale problem can be the development of a growth model fully in LBM and focused in the thrombosis process.

This thesis starts with an introductory part with an analysis of its fundamental theory, derivation of its governing equations and shows the link between the method and the the Navier-Stokes equations in an intelligible and simple way. We also provide a passive scalar-based transport model that solves the advection-diffusion equation with the intention to develop a thrombosis event. We end this part by adding the current state of the art of the thrombosis model, specially focused when the LBM plays a significant role in it.

viii

The research of this thesis is composed of two parts. The first one presents the analysis of the physical impact of using reflecting or non-reflecting boundary conditions. The test case is a developed flow in a channel with a square obstacle located in the centre. The performance of each combination of boundary conditions is assessed by calculating the forces exerted by the fluid on the obstacle surface. The overall study is presented as a parametric study using different Reynolds numbers ($50 \leq Re \leq 150$), aspect ratios of the channel ($\frac{1}{8}, \frac{1}{16}$), angles of incidence ($0°, 15.3°$ and $45°$), inlet/outlet boundary condition combinations, including Equilibrium, Zou/He and Characteristic boundary conditions. In addition, we develop an ill-posed algorithm to set non-reflecting boundary conditions at both inlet and outlet. We conclude this part of the research by deeply analysing two different characteristic boundary approaches at the outlet: the *Local One Dimensional Inviscid* equations, and Thompson.

In the last part of the investigation, we develop a passive scalar-based solute transport model in LBM for high Schmidt numbers (≈ 23 and ≈ 1220). We propose a simple hemodynamic scenario that consists of a two dimensional confined channel with a width similar to a human coronary artery diameter (3mm). Only the platelets are considered as the driven solute and therefore, we add a force term to the transport equation that governs the platelet concentration to reproduce the margination effect that they experiment in the blood flow. Finally, we develop a first order reaction boundary condition which mimics a vessel rupture that triggers the coagulation. The results give an excellent agreement of numerical platelet reaction rates and the theoretical values for both Schmidt numbers considered and sets the basis for a full LBM growth model in such conditions.

Resumen

El método *lattice Boltzmann* (LBM) es una técnica de computación de dinámica de fluidos (CFD) que está ganando popularidad rápidamente debido a sus inherentes propiedades: trata formas geométricas complejas con relativa facilidad, es computacionalmente fácil de implementar y se puede usar con herramientas de paralelización de forma eficaz. Estas características lo convierten en una potente alternativa para ser considerado en varias aplicaciones –medios porosos, hemodinámica, fluidos multifásicos, etc. No obstante, este método no está enteramente establecido en la comunidad científica debido a su relativa tardía aparición. Además, el método está todavía en constante evolución. Un aspecto que aún es objeto activo de investigación es el desarrollo de condiciones de frontera. En esta tesis se revisarán y analizarán algunas de ellas.

Aparte de las propiedades mencionadas, el método también posee importantes limitaciones. Por ejemplo, es un método diseñado para flujos subsónicos (Ma < 0.3). Es esencialmente isotérmico, por lo que solo tolera pequeñas variaciones de temperatura. El modelo de transporte basado en un escalar pásivo presenta restricciones para elevados números de Schmidt y Prandtl debido a la gran diferencia de escalas en las que se desarrollan los diferentes mecanismos de difusión térmica o material, con respecto a la de momento. Esta diferencia puede llegar a demandar un esfuerzo computacional inasumible. Aunque existen diferentes técnicas y métodos que se acoplan al LBM para mitigar esos problemas, no hay consenso general sobre cuál es el límite del LBM en problemas de altos números de Schmidt y Prandtl. Un escenario apropiado para probar las limitaciones de este método es el de un episodio de trombosis como problema con múltiples escalas de tiempo.

Esta memoria consiste en una primera parte de introducción, seguido de los fundamentos del método así como su relación con las ecuaciones de Navier-Stokes de forma inteligible y simple. También se añaden otras implementaciones como el modelo de transporte basado en un escalar pasivo, el cálculo de fuerzas sobre superficies de objetos y del esfuerzo cortante, todas ellas importantes para poder desarrollar un modelo de trombosis. Finalizamos la parte de la teoría con el actual estado del arte de los modelos de trombosis, enfocándolo especialmente sobre aquellos en los que el LBM tiene un papel significativo.

x

La parte de investigación de la tesis esta compuesta de dos partes claramente diferenciadas. La primera de ellas presenta el análisis del efecto que se produce al utilizar condiciones de frontera reflexivas o no-reflexivas. El caso de estudio consiste en el flujo a través de un obstáculo orientable en la línia central de un canal bidimensional. Se evalúa el rendimiento de las posibles combinaciones de condiciones de frontera calculando las fuerzas que el flujo ejerce sobre la superfície del obstáculo. El estudio global se presenta en forma de estudio paramétrico utilizando diferentes números de Reynolds ($50 \leq Re \leq 150$), relaciones de aspecto del canal ($\frac{1}{8}, \frac{1}{16}$), ángulos de incidencia ($0°, 15.3°$ and $45°$) y combinaciones de condiciones de frontera, incluyendo entre ellas las de Equilibrio, Zou/He y las condiciones de frontera características. Adicionalmente, desarrolamos un algoritmo basado en este caso concreto capaz de establecer una condicion de frontera no-reflexiva tanto en la entrada como en la salida. Finalizamos esta parte de investigación con un análisis mas profundo de dos tipos de condiciones de frontera características: las *LODI* y la condición de frontera de Thompson.

En la última parte de la tesis, desarrollamos un modelo de transporte de materia basado en un escalar pasivo a altos números de Schmidt (≈ 60 y ≈ 1220). Proponemos con ese modelo un escenario hemodinámico que tiene como caso de estudio un canal bidimensional con un diámetro similar al de una típica arteria coronaria humana (3mm). Considerando las plaquetas como un escalar pasivo, implementamos un término de fuerza que las desplace lateralmente hacia la pared tal y como pasaría en condiciones normales en la sangre. Este efecto de agrupamiento en las paredes se denomina marginación de las plaquetas. Finalmente, desarrollamos un modelo de reacción superficial de primer orden para que tras un evento de rotura de la pared del canal, se pueda desencadenar la trombosis. Los resultados preliminares de la razón de reacción para estos altos números de Schmidt coinciden muy bien con los valores analíticos. Con estos resultados se abre la posibilidad de generar un modelo integral en LBM con parte hidrodinámica y parte de transporte y reacción para realizar simulaciones de trombosis.

Table of contents

List of figures

UNIVERSITAT ROVIRA I VIRGILI
REVIEW OF BOUNDARY CONDITIONS AND INVESTIGATION TOWARDS THE DEVELOPMENT OF A GROWTH MODEL: A LATTICE
BOLTZMANN METHOD APPROACH
Albert Puig Arànega

xiv   List of figures

List of figures

List of tables

Symbols

Roman Symbols

ΔC_L mean peak-to-peak lift coefficient

L   characteristic wave amplitude

M   diagonal matrix with local eigenvalues

S   coefficient matrix for the diagonalization of A

T   coefficient matrix for the diagonalization of B

I   identity matrix

$\mathrm{d}\vec{x}_n$ normal distance between a boundary and a fluid node

$\vec{c}$ thermal particle speed

$\vec{U}$ macroscopic variable

$\vec{u}$ macroscopic velocity

$\vec{v}$ particle propagation speed

$\vec{x}$ space position

$\vec{x}_b$ wall node attached to a fluid node

$\vec{x}_f$ fluid node attached to a wall node

$\vec{x}_w$ exact position of a boundary wall

A coefficient matrix

a constant related to the scale of the particle collisions

AR aspect ratio

xx   Symbols

B	coefficient matrix
C	solute concentration
c_0	mean thermal particle speed
C_D	drag coefficient
C_d	instantaneous drag coefficient
C_L	lift coefficient
C_l	instantaneous lift coefficient
c_s	speed of sound
$C_{p,eq}$	initial platelet concentration profile
$C_{p,eq}(\vec{x}, R)$	platelet potential field, depending on space and radius
D	solute diffusion coefficient
D_e	enhanced diffusivity
D_{th}	thermal diffusion coefficient
E	total kinetic energy
F	body force
f	density distribution function
F_D	drag force
F_L	lift force
f_v	vortex frequency
F_α	force vector
g	density distribution function for the passive scalar
h	characteristic projected length
j	momentum density
k	parameter to keep checkerboard instabilities

Symbols xxi

k_d constant related to the enhanced diffusion model

k_{rt} binding kinetic constant

k_{th} Boltzmann constant of particle thermal diffusion

L characteristic length

l_f mean free path

L_r/h recirculation length ratio

L_y channel diameter

M moment matrix

m_j distribution functions in the moment space

M_{cd} margination conditioning parameter

N edge length of square obstacle

N nodes that has a nondimensional characteristic length

n constant related to the enhanced diffusivity

N'' mass flux

N_t number of time steps that has a nondimensional characteristic time

p pressure

Q blood flow

R channel radius

R specific gas constant

R_{eq} equivalent sphere radius of the particle

S relaxation rate matrix

s_j element j of the relaxation rate matrix S

S_p sink term for platelets

$S_{\alpha\beta}$ shear rate tensor

Sf	surface
T	temperature
t	time
$S_{\alpha\beta}$	shear rate tensor
Da	Damkhöler number
Kn	Knudsen number
Ma	Mach number
Re	Reynolds number
Sc	Schmidt number
Sh	Sherwood number
St	Strouhal number

Greek Symbols

β	constant for the tanh function used in the platelet profile
Δ	discrete unitary increment
δ_c	mass transport boundary layer
δ_f	reactive surface length
δ_p	constant for the tanh function used in the platelet profile
$\delta_{\alpha\beta}$	Kronecker delta
$\dot{\gamma}$	scalar shear rate
ε	internal energy
Λ	diagonal matrix with local eigenvalues
λ	constant for the tanh function used in the platelet profile
λ_i	ith element from the vector of eigenvalues Λ
ω_i	weight coefficient

Symbols xxiii

μ	dynamic viscosity
ν	kinematic viscosity
ω	relaxation rate
ϕ	hematocrit
Π	momentum flux
ρ	macroscopic density
σ	shear stress
τ	relaxation time
θ	obstacle incidence angle
Ω	collision matrix
$\vec{\ell}_i^\top$	ith row of S
$\vec{\xi}$	lattice propagation speed
$\vec{\xi}_i$	set of lattice propagation speeds with i elements
$\vec{\zeta}$	drift term for platelet margination

Superscripts

a^{eq}	equilibrium value of a
a^{in}	variable a as an input
a^{neq}	non-equilibrium part of variable a
a^{out}	variable a as an output

Subscripts

a_c	variable a addressed to the passive scalar algorithm for the solute transport model
a_d	nondimensional variable of a
a_p	physical variable of a
a_p	variable a addressed to platelets

a_0 reference/unperturbed value of a

$a_{\alpha\beta}$ tensor of variable a

a_{lb} variable a in lattice units

a_{max} peak value of variable a

a_{rw} local value of variable a at the reacting wall

Other Symbols and Operators

δt nondimensional lattice time

δx nondimensional lattice space

$\hat{a}$ alternative nondimensional form of variable a

$\nabla\cdot$ divergence differential operator

∇ gradient differential operator

$\nabla_{\vec{v}}$ velocity gradient differential operator

Ω collision operator

∂a partial derivative of a

$\mathrm{d}a$ derivative of a

$\tilde{a}$ post-collision value of a

$\vec{a}$ variable a is an array

$a_{\bar{i}}$ specular direction of a_i

$a_{\bar{i}}$ opposite direction of a_i

Chapter 1

Introduction

The lattice Boltzmann method (LBM) is a non-conventional computational fluid dynamics (CFD) method, introduced in the literature in the late 80s [47] as alternative to traditional CFD methods. Traditional CFD methods are based on numerical solution of Navier-Stokes equations (NS) which are solved using finite difference, finite volume or finite element methods. The NS equations are partial differential equations that describe the temporal evolution of fluid flow considering macroscopic variables.

In the context of variables, the term *macroscopic variables* refers to physical properties associated with the continuum hypothesis (e.g. pressure, density, viscosity, etc), while the term *microscopic*, which can be defined as a framework that cannot be seen or it is hardly visible to the human eye due to its dimensions. In fluid dynamics, if the scale is small enough, one can start to observe discontinuities on the previously smooth, macroscopic variables of the fluid, and thus, the continuum hypothesis ceases to be acceptable. These discontinuities are particles that are distinguishable at this framework, and the magnitude of the mean free path of collision for these particles starts to compete with the characteristic length of the system, which means that the Knudsen number is now at bigger than 0.1. An example of a microscopic variable could be a system of particles (atoms, molecules) that are confined in a volume. Each of these particles will have its own velocity and direction. In addition, these particles can eventually collide with the solid boundaries of the system of even with other particles, which alter both velocity and directions of these particles. If we were able to observe the system at this diminute scale, one would only see a bunch of particles travelling relatively at a speed of the order of k_BT, where k_B is the Boltzmann constant and T is the temperature of the medium. If one particle of that system were tracked, it would show an erratic trajectory, constantly changing its direction due to the impacts with other particles. Therefore, we can theoretically define the behavior of a fluid system by gathering both the velocity and the position of each particle and compute their

temporal evolution by developing an operator to describe all of the collision events that will take place. Such operator can be for example, for ideal gases, the Newton's laws of motion, or even more complicated models of collision that might include further degrees of freedom of the particles, such as rotation or vibration. Anyway, it is quite senseless to attempt such a pretentious calculation in any industrial approach, due to the titanic computational effort that simulating a very little portion of the fluid would demand. For example, to predict the behavior of 1 ml of water at room conditions, we would have to compute the microscopic variables of more than 3×10^{22} molecules. Hence, this fact strongly encourages the usage of simulation methods that compute the fluid as a global and *smoother* system, using the macroscopic variables.

Both macroscopic and microscopic worlds are connected. Both perspectives give us the same relevant information, that is the *fluid behavior*. The difference between these two approaches are the variables considered, and with them, the level of detail of the fluid. The macroscopic variables are a statistical estimation of the microscopic ones. For example, the variable density describes the mass value (where the mass is a certain amount of particles) over a certain volume. This is, of course, an approximation due to the fact that, even at rest, the particles of a fluid are always in constant motion, colliding and travelling around. So it is really easy to see that if one counts the number of particles over the same volume in two different instants, there exists the possibility that we will not get the same exact number of particles, and thus there will be density variations. That is why, in the microscopic scale, we can define a macroscopic variable as an estimation that can carry statistic noise. The same happens with the linear momentum of the fluid, which can be considered as an average of the velocity of all the particles within a certain portion of the fluid. In fact, it is proven that the NS equations can be derived from other more elemental equations [13] as both scales are linked.

Between the macroscopic and microscopic scales exists a transitional scale, the *mesoscopic scale*. At this scale, instead of monitoring each particle or considering a continuum medium, the framework focuses on groups of particles, or *particle distributions*. The main variable used in this case is the distribution function $f(\vec{x}, \vec{v}, t)$, which denotes the probability of finding a particle at a certain position, velocity, and time. We will discuss more features of this variable in Sec. 2.1.1. The *Boltzmann equation* (BE) is the one that describes the evolution of the particle distribution function with the time and is the cornerstone of the LBM. As with the microscopic scale, the Boltzmann equation can be connected to the NS equations (see Sec. 2.1.2), which means that the BE can be used to model the fluid behavior as if the NS equations were directly used.

The roots of the LBM come from the lattice gas cellular automata (LGCA), which is based on a microscopic approach (i.e., it deals with single particles) and in the

kinetic theory of gases. The core of this method consists in colliding and streaming each single particle along a set of discrete directions available in the considered lattice configuration. The simple collision events consider perfectly elastic collisions between spherical particles. Although this method was able to reproduce the NS equations with a very efficient code, it adds noticeable statistical noise [64]. This was highly undesired in fluid-mechanical applications, as simulations do not reach any particular steady state.

Unlike its predecessor, the LBM could overcome the LGCA issues, keeping a similar approach as the former model. Instead of considering particles as single entities on each node, it considers distributions of particles. Thus, we talk about probabilities of finding a certain number of particles in a particular state. This is the main feature that converts the LBM into a mesoscopic instead of a microscopic method. The LBM still uses the core of the method i.e. the streaming and the collision of particles at each time step and each node. However, the difference between the LGCA method relies on the fact that particles are statistically treated with a probability according to their state in the control volume. By discretizing the BE and applying a correct collision operator we can develop a model able to simulate the fluid behaviour by means of the lattice Boltzmann equation (LBE).

Certainly, we have a tool at our disposal that can simulate fluids, but, why and when is it worth to use the LBM in detriment of other former CFD methods? The answer to this question obviously relies on the nature of the system to be simulated. Nonetheless, the LBM outperforms other CFD methods:

- It is *computationally efficient*: it is an explicit method (first order in time), and its core only deals with linear operations.

- It is *versatile*: it is easy to be implemented for different applications, such as porous media, multiphase, multicomponent flows. It is normally used with uniform square lattices, which is excellent for computational memory efficiency and it facilitates the development of algorithms for complex or moving geometries.

- It is suitable for *parallel computing*: its local computational implementation perfectly matches with the parallel computational processing tools (OpenMP® or Graphic Processing Units [GPU]), which can highly extend its applicability to more demanding and complex systems.

Despite these many advantages, the method is not flawless. For example, it is limited to work in the subsonic range (Ma < 0.3)*. Additionally, the method is isother-

---

*this affirmation is only relative to a simple and most popular LBE approximation. With higher order schemes of the LBM, it is nowadays possible to reach velocities up to Ma = 2, e.g.,[73].

mal in nature, and therefore, it is only possible to couple thermal and hydrodynamic models with a very limited range of temperature variations (keeping the speed of sound constant) [28]. A common technique is to couple both models adding an additional distribution function that models a passive scalar which is advected by the flow velocity, recovering the heat (or mass) transport equation.

Thesis goals

Two are the main goals in this thesis which are briefly summarised,

i) to advance in the knowledge and implementation of LBM boundary conditions. This constitutes a relevant problem on its own, as boundary conditions are naturally imposed in CFD simulations on the hydrodynamic fields, density, velocity, temperature, instead of the particle distribution functions, which are the simulated variables in the LBM. The streaming-collision events at the core of the method make the fluid slightly compressible, this is why even in the low sub-sonic regime, boundary reflections can introduce spurious effects in the flow velocity and the forces experienced by objects immersed in the fluid. Different types of boundary conditions and their combination have been used traditionally with this method, and understanding the effects produced following their implementation is of primary importance.

ii) to carry out research in the applied field of hemodynamics, paying special attention to the modelling of platelet behaviour. On one side, we propose a novel LBM approach to model platelet margination, which is the near-wall migration of platelets in arteries. The proposed model is based on the phenomenological model provided by Eckstein and Belgacem [19]. On the other side, the thesis collects a set of tools that are relevant to develop a growth model for platelets in the LBM. This includes a validated surface reaction in similar conditions than in a human coronary artery or a computational region algorithm to transform reacted platelets into a solid thrombus.

Thesis structure

The thesis is arranged in the following chapters:

- Chapter 2 is devoted to giving further details of the LBM. We provide an introductory part where we analyse the LBM and derive its fundamental equations.

UNIVERSITAT ROVIRA I VIRGILI
REVIEW OF BOUNDARY CONDITIONS AND INVESTIGATION TOWARDS THE DEVELOPMENT OF A GROWTH MODEL: A LATTICE
BOLTZMANN METHOD APPROACH
Albert Puig Arànega

5

We also facilitate the information about the link between the LBM equations and the classical Navier-Stokes equations. Additionally, this chapter offers a brief state of the art of the LBM research related to biological flows, specifically with the thrombosis phenomenon and the role of platelets in this process.

- Chapter 3 reports all the different LBM boundary conditions used in this work. This dedicated chapter introduces, classifies and properly analyses each of the different algorithms used to model the boundary conditions used in this thesis.

- Chapter 4 reports a comparison of reflective *vs*. non-reflective boundary conditions and their performance. It contains the results of a parametric study on the lift and drag forces experienced by an object immersed in the flow, and analyses the efficiency of different sets of inlet/outlet boundary conditions upon different Reynolds numbers, domain dimensions and angle of incidence of the obstacle.

- Chapter 5 reports the results obtained for a transport and reaction model based on the passive scalar technique. The simulation domain is a closed channel having the dimensions of a hypothetical coronary artery. The results are validated and discussed and a possible. The chapter ends with the most remarkable conclusions, a description of the following steps to improve the tools and to develop the growth model, and a possible future working environment for the complete model.

- Chapter 6 resumes all the remarks obtained during the previous chapters and also gives a brief conclusion to the thesis.

Published works and conferences

Journal Articles

Albert Puig-Arànega, Javier Burgos, Salvatore Cito, Ildefonso Cuesta and Clara Salueña. "Analysis of reflective and non-reflective boundary conditions in LBM simulations of flow past an obstacle in a channel", International Journal of Computational Fluid Dynamics, 2016, 29:9-10, pp436-446. DOI:10.1080/10618562.2015.1111341

Conference Contributions

Albert Puig, Javier Burgos, Clara Salueña, Ildefonso Cuesta, "Analysis of flow past a square cylinder with different angles of incidence with several open boundary conditions using the Lattice Boltzmann Method", 10th International Conference for

Mesoscopic Methods in Engineering and Science, Oxford (United Kingdom), 2013. Oral presentation.

Albert Puig, Javier Burgos, Clara Salueña, Ildefonso Cuesta, "Parametric study of artery aneurysms by the Lattice Boltzmann Method", 10th Doctoral Day Poster Exhibition, Tarragona (Spain), 2013.

Albert Puig, Javier Burgos, Clara Salueña, Ildefonso Cuesta, Salvatore Cito, "Simulation of thrombosis using Michaelis-Menten based binding kinetics with Lattice Boltzmann Method", 11th Doctoral Day Poster Exhibition, Tarragona (Spain), 2014.

Chapter 2

Fundamental Theory

2.1 Theory of the Lattice Boltzmann Method

The kinetic gas theory describes the behavior of a gas by considering it as a system of particles. Such particles are atoms and molecules that, even at macroscopic rest (equilibrium state), collide with each other at velocities that can surpass the speed of sound. It is easy to imagine that it is not possible nowadays to theoretically apply this kinetic theory at the macroscopic level, as one must deal with a frame of more than 10^{22} particles. Specifically, to implement such theorem in the tangible reality, one would have to consider the position $\vec{x}$, velocity $\vec{v}$ in space and the internal energy for each particle.

Instead of this detailed microscopic approach, the following section describes the behavior of particles with a simpler approach. We will consider clusters of monoatomic particles (no inner energy associated and typical from ideal gases), which will behave as a macroscopic system. Nonetheless, each of the quantifiable macroscopic variables (density, velocity) is bounded to the momentum and the density of the particles that the cluster gathers. Summarizing, all of the macroscopic variables will be dependent on an elemental variable, and with it, the approach shifts from a microscopic to a mesoscopic point of view.

2.1.1 Density Distribution Function

The density distribution function $f(\vec{x},\vec{v},t)$ (we will often use f instead of the longer notation of $f(\vec{x},\vec{v},t)$) is a variable that describes the mass density of particles in a given control volume at a certain spot $\vec{x}$, differential particle velocity range $[\vec{v},\vec{v}+d\vec{v}]$ and time t. This variable is observable in the called phase–space. By applying the moments on the density distribution function one can recover the macroscopic variables. A

moment is basically a velocity integral of f weighted over every possible particle velocity. This step is obviously crucial to reach a reasonable understanding of the system evolution. The used moments, which are able to recover the macroscopic properties can be used in different orders to gather different macroscopic variables. The zeroth order moment is

$$\rho(\vec{x},t) = \int f(\vec{x},\vec{v},t) \mathrm{d}\vec{v},\tag{2.1}$$

where the distribution function is integrated over all possible velocities and weighted with $\vec{v}^0$, which finally gives the macroscopic density ρ. Thus, the integration limits will be from 0 to infinite, but for simplicity we are not going to specify them.

When the distribution function is integrated with $\vec{v}$ as weight gives the momentum,

$$\rho\vec{u}(\vec{x},t) = \int \vec{v}f(\vec{x},\vec{v},t) \mathrm{d}\vec{v},\tag{2.2}$$

where $\vec{u}$ is the macroscopic velocity of the control volume.

If instead, f is weighted with $\frac{|\vec{v}|^2}{2}$, the result gives the total kinetic energy E,

$$\rho E(\vec{x},t) = \int \frac{|\vec{v}|^2}{2} f(\vec{x},\vec{v},t) \mathrm{d}\vec{v},\tag{2.3}$$

which accounts for the purely translational motion of the fluid ($\frac{1}{2}|\vec{u}|^2$) plus the internal energy ε due to the thermal vibration of the particles which is independent of the bulk velocity,

$$\rho E = \rho \left(\varepsilon + \frac{1}{2}|\vec{u}|^2 \right),\tag{2.4}$$

The internal energy can be derived from the fluctuational part of the velocity, defined as the thermal particle velocity,

$$\vec{c} = \vec{v} - \vec{u}.\tag{2.5}$$

The first order moment of f weighted with $\vec{c}$ is

$$\int \vec{c}f\mathrm{d}\vec{v} = \int \vec{v}f\mathrm{d}\vec{v} - u \int f\mathrm{d}\vec{v} = \rho u - \rho u = 0.\tag{2.6}$$

From Eq. 2.6, one can mathematically infer that the thermal molecular speed does not contribute to the momentum. Therefore, the distribution of the thermal molecular speed is essentially symmetrical.

The second order moment gives the momentum flux tensor,

$$\rho u_\alpha u_\beta + p\delta_{\alpha\beta} - \sigma_{\alpha\beta} = \int v_\alpha v_\beta f\mathrm{d}\vec{v} = \Pi_{\alpha\beta},\tag{2.7}$$

and the second order central moment relative to the bulk velocity $\vec{u}$, which corresponds to the stress tensor is

$$p\delta_{\alpha\beta} - \sigma_{\alpha\beta} = \int (v_\alpha - u_\alpha)(v_\beta - u_\beta)f\mathrm{d}\vec{v}, \tag{2.8}$$

where $\sigma_{\alpha\beta}$ is the shear stress tensor, and $p\delta_{\alpha\beta}$ is the normal stress tensor.

2.1.2 The Boltzmann Equation

Ludwig Boltzmann stated that, in a moving reference system, the rate change of the density distribution function is determined by

$$\frac{\partial f}{\partial t} + \vec{v} \cdot \nabla f + \frac{\vec{F}}{\rho} \cdot \nabla_{\vec{v}} f = \Omega(f). \tag{2.9}$$

The Boltzmann equation (BE) (Eq. 2.9) statistically considers the behavior of a thermodynamic system that generally is not in its equilibrium state. Such system is defined by the aforementioned density distribution function $f(\vec{x}, \vec{v}, t)$ in a phase space that takes into account the position $\vec{x}$ and its velocity $\vec{v}$. A principal statement consists in considering three density distribution terms in a moving reference system that modifies f. An external force term, diffusive term and the particle-particle collision term. The first term in Eq. 2.9 is the change rate of f in a time step. The second term is the advection of the particles, the third term of Eq. 2.9 is the external force $\vec{F}$ which depends directly on the mass density ρ. On the right hand side of Eq. 2.9 we have $\Omega(f)$ representing the collision term. The only contribution that can change the direction of the velocities for f is the collision term. When the control volume is in an equilibrium state, the collision operator becomes zero. We will further discuss this latter assumption in Secs. 2.1.3 and 2.1.4.

We now analyse the nature and applicability of the BE. The zeroth order of Eq. 2.9 must recover the mass conservation equation,

$$\frac{\partial}{\partial t} \int f\mathrm{d}\vec{v} + \nabla \cdot \int \vec{v}f\mathrm{d}\vec{v} + \frac{\vec{F}}{\rho} \cdot \int \nabla_{\vec{v}} f\mathrm{d}\vec{v} = \int \Omega(f)\mathrm{d}\vec{v}, \tag{2.10}$$

since the integral $\int \nabla_{\vec{v}} f\mathrm{d}\vec{v} = 0$, and the collision operator is invariant (see Eq. 2.24 below), by combining Eqs. 2.1 and 2.2 the zeroth order of Eq. 2.10 is the continuity equation,

$$\frac{\partial}{\partial t} \int f\mathrm{d}\vec{v} + \nabla \cdot \int \vec{v}f\mathrm{d}\vec{v} = \int \Omega(f)\mathrm{d}\vec{v} =$$
$$\frac{\partial \rho}{\partial t} + \nabla(\rho\vec{u}) = 0. \tag{2.11}$$

Now using the same procedure as in Eq. 2.10 for the first order moment of the BE, one has

$$\frac{\partial}{\partial t}\int \vec{v} f \mathrm{d}\vec{v} + \nabla \cdot \int v_\alpha v_\beta f \mathrm{d}\vec{v} + \frac{\vec{F}}{\rho} \cdot \int v_\alpha \nabla_{v_\beta} f \mathrm{d}\vec{v} = \int \vec{v} \Omega(f) \mathrm{d}\vec{v}, \tag{2.12}$$

where the integral $\int v_\alpha \nabla_{v_\beta} f \mathrm{d}\vec{v} = -\int \frac{\partial v_\alpha}{\partial v_\beta} f \mathrm{d}\vec{v} = -\rho \delta_{\alpha\beta}$, $\delta_{\alpha\beta}$ being the Kronecker delta.

The equation that results from combining Eq. 2.2, Eq. 2.7 and Eq. 2.12 leads to

$$\frac{\partial \rho \vec{v}}{\partial t} + \nabla \cdot \Pi_{\alpha\beta} - \vec{F} = 0. \tag{2.13}$$

This latter formulation can be expressed as the Cauchy momentum equation

$$\frac{\partial \rho \vec{v}}{\partial t} + \nabla \cdot \rho \vec{v_\alpha} \vec{v_\beta} = -\nabla \cdot \vec{p} + \nabla \cdot \sigma_{\alpha\beta} + \vec{F}. \tag{2.14}$$

2.1.3 Equilibrium Distribution Function

The equilibrium distribution function, namely f^{eq}, is an important element that contributes on the relaxation of the distribution function in the LBM. In a system of particles in local equilibrium state, that it has been unperturbed for a reasonable long time, there is no significant redistribution of density and momentum, which means that the density distribution remains unchanged over time. In other words, the collision operator $\Omega(f)$ should be zero. The mathematical expression without external forces Eq. 2.9 becomes

$$\frac{\partial f}{\partial t} + \vec{v} \cdot \nabla f = \Omega(f) = 0, \tag{2.15}$$

A given particle system in equilibrium has a velocity distribution that is statistically predictable. In a two dimensional ideal gas, the distribution function in equilibrium responds to the Maxwell–Boltzmann distribution

$$\begin{aligned} f^{eq}(\rho, \vec{v}, \vec{u}) &= \frac{\rho}{(2\pi RT)} \exp\left(-\frac{(\vec{v}-\vec{u})^2}{2RT}\right) \\ &= \frac{\rho}{(2\pi RT)} \exp\left(-\frac{\vec{v} \cdot \vec{v} - 2\vec{v} \cdot \vec{u} + \vec{u} \cdot \vec{u}}{2RT}\right). \end{aligned} \tag{2.16}$$

From here, we will eventually shorten the $f^{eq}(\rho, \vec{v}, \vec{u})$ into f^{eq}. Moreover, under the assumption that f^{eq} is a normal distribution, the speed of sound $c_s = \sqrt{RT}$ is the standard deviation. We are assuming an ideal gas and the fact that the LBM is fundamentally isothermal, so that the speed of sound will be kept constant, as T is

constant. Eq. 2.16 is left as

$$f^{eq} = \frac{\rho}{(2\pi c_s^2)} \exp\left(-\frac{\vec{v}\cdot\vec{v} - 2\vec{v}\cdot\vec{u} + \vec{u}\cdot\vec{u}}{2c_s^2}\right). \tag{2.17}$$

The exponential term of the f^{eq} in Eq. 2.17 can be approximated with polynomials by applying an expansion of the velocity up to the second order, reaching the following expression

$$f^{eq} \approx \frac{\rho}{(2\pi c_s^2)} e^{-(\vec{v}\cdot\vec{v})/2c_s^2} \cdot \left(1 + \frac{\vec{v}\cdot\vec{u}}{c_s^2} + \frac{(\vec{v}\cdot\vec{u})^2}{2c_s^4} + \frac{\vec{u}\cdot\vec{u}}{2c_s^2}\right). \tag{2.18}$$

Note that this approximation is only valid for low Mach numbers ($\mathrm{Ma} = u/c_s \leq 0.3$) and therefore the system will only accept weak compressions.

Then, by means of a Gauss-Hermite quadrature, the velocity space can be converted from a continuum into a discrete set of velocities with number i (details on the Gauss-Hermite quadrature [32]). The term $\frac{1}{2\pi c_s^2} e^{-\frac{1}{2}\frac{\vec{c}^2}{c_s^2}}$ is linearized to the weight variable ω_i,

$$f_i^{eq}(\rho,\vec{u}) = \rho\omega_i\left(1 + \frac{\vec{v}\cdot\vec{u}}{c_s^2} + \frac{(\vec{v}\cdot\vec{u})^2}{2c_s^4} + \frac{\vec{u}\cdot\vec{u}}{2c_s^2}\right). \tag{2.19}$$

From Eq. 2.19 one can note that the variable $f^{eq}(\rho,\vec{u},\vec{v})$ has been converted into $f_i^{eq}(\rho,\vec{u})$. We will later discuss the discretized Boltzmann equation in time and in space in Sec. 2.1.5. For the purpose of this section, we will continue with the continuum form of f and f^{eq}.

Now we show the raw normal moments and the central moments of f^{eq}. The zeroth and first order raw moments are equal to Eq.2.1 and Eq.2.2,

$$\rho = \int f^{eq}(\rho,\vec{u},\vec{v})d\vec{v}, \tag{2.20a}$$

$$\rho\vec{u} = \int \vec{v}f^{eq}(\rho,\vec{u},\vec{v})d\vec{v} \tag{2.20b}$$

The first central moment of f^{eq} is also the same as Eq. 2.6

$$\int \vec{c}f^{eq}d\vec{v} = \int \vec{v}f^{eq}d\vec{v} - \vec{u}\int f^{eq}d\vec{v} = \rho\vec{u} - \rho\vec{u} = 0. \tag{2.21}$$

The second order central moment is developed as [65]

$$\int c_\alpha c_\beta f^{eq}d\vec{v} = p\delta_{\alpha\beta}, \tag{2.22}$$

this latter derivation is important as it clearly states that, under equilibrium conditions, the second order moment will only perceive the contribution of normal forces. This can be clarified by checking Eq. 2.8, where the stress tensor does contain both normal and shear contributions. It is also intuitive to think that if the given distribution functions at a given node are at equilibrium, it means that they are fully relaxed —they only exert pressure.

On the other hand, the energy moment (weighted with $\frac{|\vec{c}|^2}{2}$) is calculated combining Eq. 2.4 and Eq. 2.3,

$$
\begin{aligned}
\frac{1}{2}\int |\vec{c}|^2 f^{eq}\mathrm{d}\vec{v} &= \frac{1}{2}\int (v-u)(v-u)f^{eq}\mathrm{d}\vec{v} \\
&= \frac{1}{2}\int |v|^2 f^{eq}\mathrm{d}\vec{v} + \frac{1}{2}|u|^2\int f^{eq}\mathrm{d}\vec{v} - u\int v f^{eq}\mathrm{d}\vec{v} \\
&= \rho E + \frac{1}{2}\rho |u|^2 - \rho |u|^2 \\
&= \rho \varepsilon
\end{aligned}
\tag{2.23}
$$

Which relates the thermal particle velocity and the temperature with the internal energy of the control volume, that is directly related to the temperature.

2.1.4   Collision Operator

The collision term specified in Eq. 2.9 is a rather complex integral that describes the rate of change of the particle distribution function produced by collisions. The result of this integral is discussed by Chapman and Cowling [12].

We skip the derivation process of the collision integral and focus on the results. The integral of the collision operator has some conservation properties. $\Omega(f)$ satisfies:

$$\text{Mass conservation} \qquad \int \Omega(f)\mathrm{d}\vec{v} = 0 \tag{2.24a}$$

$$\text{Momentum conservation} \qquad \int \vec{v}\Omega(f)\mathrm{d}\vec{v} = 0 \tag{2.24b}$$

$$\text{Energy conservation} \qquad \int |\vec{v}|^2\Omega(f)\mathrm{d}\vec{v} = 0 \tag{2.24c}$$

Additionally, the collision term must approach the density distribution function towards its equilibrium state. In the LBM, the collision operator is greatly simplified for practical and computational reasons. The two analysed forms of $\Omega(f)$ are the Bhatnagar–Gross–Krook and the Multiple Relaxation Time approaches (MRT). Unlike the original collision operator, both models are able to thermalize the mesoscopic par-

ticles in a control volume towards equilibrium without considering each two-particle collision in detail.

The generalized equation with the matrix collision operator [34] is,

$$f_i(\vec{x}+\vec{v}_i\delta t, t+\delta t) - f_i(\vec{x},t) = -\sum_j \Omega_{ij}(f_j(\vec{x},t) - f_j^{eq}(\vec{x},t)). \qquad (2.25)$$

Note that this equation is already discretized and the particle propagation speed has become the discretized lattice propagation speed. In Sec. 2.1.5 we analyse the discretized lattice Boltzmann equation with this formulation as the final result.

BGK model

The Bhatnagar–Gross–Krook model, popularly named as BGK, is linear approximation of the collision operator from Eq. 2.25. The collision operator is given in Eq. 2.26,

$$\Omega(f) = -\omega(f - f_{eq}) = -\frac{c}{l_f}(f - f_{eq}), \qquad (2.26)$$

where ω is the relaxation rate and l_f is the mean free path. It can be inferred that this collision operator will satisfy the conservation of mass, momentum and energy stated in Eq. 2.24 since the analysed moments of f^{eq} are the same as f for the same macroscopic variables. It is also intuitive to see that if there are no changes on temperature, this characteristic frequency towards the thermalization of f will be linear in this model. However, in LBM, the dimensionless relaxation rate is not derived from this theorem. Instead, ω is determined from the viscous properties of the fluid (see Sec. 2.1.5). Additionally, the distance between the groups of particles is also determined by the lattice spacing, and not by their mean free path.

Multiple Relaxation Time model

The Multiple Relaxation Time model (MRT) is a generalized collision operator that takes the form of a matrix in the evolution equation of the LBM (see Eq. 2.25). It further decomposes the f_i of the phase space into a q-dimensional space, called the moment space. The collision matrix Ω from Eq. 2.25 becomes the q × q matrix, where q is the number of velocities of the set (more details of the velocity sets in Sec. 2.1.6). This matrix considers the hydrodynamic moments, (typically the density, the momentum density and several second order tensors), but also considers some non-hydrodynamic moments. Such moments appear for example in the D2Q9 model because there are more possible velocities than possible hydrodynamic moments. Therefore some non-hydrodynamic moments are invoked to fill in the relaxation time

matrix and there is no general well-posed condition to specify them. Nevertheless, it is usual to set the non-hydrodynamic relaxation times close to one, but there are other techniques that allow to set the optimal values for these moments [8, 42]. Despite the fact that this approach differs from the kinetic gas theory basis, it provides better stability and accuracy than the LBGK method in most cases [16, 42].

For simplicity, we provide the already discretized MRT-D2Q9 general evolution equation

$$f_i(\vec{x} + \vec{\xi}_i \Delta t, t + \Delta t) - f_i(\vec{x}, t) = \Delta t [M^{-1} \cdot S_j \cdot (m_j(\vec{x}, t) - m_j^{eq}(\vec{x}, t))]_i, \qquad (2.27)$$

where the subscripts j and i refer to the index of the moment and the discrete velocity, respectively.

m_j and m_j^{eq} are the transformed distribution functions and equilibrium distribution functions into the moment space, respectively.

$$m_j(\vec{x}, t) = M \cdot f_j \qquad m_j^{eq}(\vec{x}, t) = M \cdot f_j^{eq} \qquad (2.28)$$

and the moment matrix M is defined as

$$M = \begin{pmatrix} 1 & 1 & 1 & 1 & 1 & 1 & 1 & 1 & 1 \\ -4 & -1 & -1 & -1 & -1 & 2 & 2 & 2 & 2 \\ 4 & -2 & -2 & -2 & -2 & 1 & 1 & 1 & 1 \\ 0 & 1 & 0 & -1 & 0 & 1 & -1 & -1 & 1 \\ 0 & -2 & 0 & 2 & 0 & 1 & -1 & -1 & 1 \\ 0 & 0 & 1 & 0 & -1 & 1 & 1 & -1 & -1 \\ 0 & 0 & -2 & 0 & 2 & 1 & 1 & -1 & -1 \\ 0 & 1 & -1 & 1 & -1 & 0 & 0 & 0 & 0 \\ 0 & 0 & 0 & 0 & 0 & 1 & -1 & 1 & -1 \end{pmatrix}, \qquad (2.29)$$

where M is the orthonormalized moment-based matrix (using the Gram-Schmidt procedure), which comes from a linear combination of the following moment set [42]

$$\left(M_0, M_x, M_y, M_{x^2}, M_{xy}, M_{y^2}, M_{x^2 y}, M_{xy^2}, M_{x^2 y^2} \right)'. \qquad (2.30)$$

The distribution function at equilibrium in the moment space m_j^{eq} is

$$
\begin{aligned}
m_0^{eq} &= \rho \\
m_1^{eq} &= -2\rho + (j_x^2 + j_y^2) \\
m_2^{eq} &= \rho - 3(j_x^2 + j_y^2) \\
m_3^{eq} &= j_x \\
m_4^{eq} &= -j_x \\
m_5^{eq} &= j_y \\
m_6^{eq} &= -j_y \\
m_7^{eq} &= j_x^2 - j_y^2 \\
m_8^{eq} &= j_x \cdot j_y
\end{aligned}
\qquad , \qquad (2.31)
$$

where j is the local momentum density $j = \vec{u}\rho$. Note that 2.31 refers to the incompressible MRT model. The MRT scheme starts with the diagonalization of the collision matrix

$$
\Omega = M^{-1}SM \qquad (2.32)
$$

where M is used to project the density distribution functions onto the moment space. Then, we apply the relaxation to all the moments. The conversion of f into the moment space is performed using Eq. 2.28. The following equation describes the collision which is done in the moment space

$$
m_j^{out} = m_j^{in} + s_j(m_j^{in} - m_j^{eq}). \qquad (2.33)
$$

Finally, the m^{out}s are converted back to the f space, and the collision process is completed.

The relaxation time τ is consists of a diagonal matrix $S = \text{diag}(s_j)$ with dimensions $q \times q$. The generalized relaxation rates are [61] are

$$s_0 = 1.0 \tag{2.34a}$$

$$s_1 = \frac{1}{(2\mu' + 0.5)} \tag{2.34b}$$

$$s_2 = s_1 \tag{2.34c}$$

$$s_3 = 1.0 \tag{2.34d}$$

$$s_4 = 1.2 \tag{2.34e}$$

$$s_5 = 1.0 \tag{2.34f}$$

$$s_6 = s_4 \tag{2.34g}$$

$$s_7 = \frac{1}{\tau} \tag{2.34h}$$

$$s_8 = s_7 \tag{2.34i}$$

$$\tag{2.34j}$$

where s_0, s_3 and s_5 are arbitrarily set to 1, because they will not have significance on the simulation due to the fact that they refer to the conservation of mass and momentum, and the values of these equilibrium moments are always the same ($m_j^{eq} = m_j$). The coefficient μ' is the bulk viscosity, and both s_1 and s_2 can alternatively be fixed to other values (close to 1) as we assume an incompressible LBM model. s_4 and s_6 are chosen from values used by other authors (e.g. [37, 44, 45, 59]). Alternatively, d'Humières [18] proposed the 'magic relaxation rates' for the s_4 and s_6 in order to damp slip velocity errors at the boundaries.

Finally, we see that s_7 and s_8 are relaxation rates related with the viscosity of the fluid.

As a particular case, the BGK collision model can be recovered from the MRT model by setting all the S diagonal elements to the single relaxation rate τ^{-1}

$$S = \frac{1}{\tau}\mathbf{I}, \tag{2.35}$$

where $\mathbf{I}$ is the $q \times q$ identity matrix.

2.1.5   Discretized Lattice Boltzmann Equation

The first step to discretize the Boltzmann equation is to work in the dimensionless units. We consider the Boltzmann Equation without the force term

$$\frac{\partial f}{\partial t} + \vec{v} \cdot \nabla f = \Omega(f), \tag{2.36}$$

By adding the BGK model in Eq. 2.26 we obtain

$$\frac{\partial f}{\partial t} + \vec{v} \cdot \nabla f = -\frac{c_0}{l_f}(f - f_{eq}), \tag{2.37}$$

where we can associate the particle collision rate as the ratio of the mean thermal particle speed c_0 with the mean free path l_f. A characteristic length L is added with the mean thermal particle speed c_0 and ρ as a set of variables to nondimensionalize Eq. 2.37, which results in the following expression

$$\frac{\partial \hat{f}}{\partial \hat{t}} + \hat{\vec{\xi}} \cdot \nabla \hat{f} = -\frac{1}{\text{Kn}}(\hat{f} - \hat{f}^{eq}), \tag{2.38}$$

where

$$\hat{x} = \frac{x}{L} \tag{2.39a}$$

$$\hat{t} = \frac{t \cdot c_0}{L} \tag{2.39b}$$

$$\frac{l_f}{L} = \text{Kn} \tag{2.39c}$$

$$\hat{\vec{\xi}} = \frac{\vec{v}}{c_0} \tag{2.39d}$$

$$\hat{f} = \frac{f \cdot c_0{}^3}{\rho^3}, \tag{2.39e}$$

The nondimensional phase space and time variables $(\hat{x}, \hat{\vec{\xi}}, \hat{t})$ are converted into the lattice values, which conveniently change the propagation speed into the lattice propagation speed $\vec{\xi}$, the magnitude of which is unity in a uniform grid. This procedure is further developed in Sec. 2.1.7.

Then again, (as in Sec. 2.1.3 and Sec. 2.1.4), we discretize f and $\vec{\xi}$ into arrays of i velocity directions. Then a first order finite differences and a forward time step

approximation [61] is applied at Eq. 2.38, resulting in

$$\frac{f_i(\vec{x},t+\Delta t)-f_i(\vec{x},t)}{\Delta t}+\vec{\xi}_i \cdot \frac{f(\vec{x}+\Delta t \cdot \vec{\xi},t+\Delta t)-f(\vec{x},t+\Delta t)}{\Delta t \vec{\xi}_i}=-\omega(f_i(\vec{x},t)-f_i^{eq}).$$

(2.40)

This formula can be further elaborated knowing that the magnitude of the propagation speed is the rate of the propagation of f over a unit of lattice spacing at each unit of time spacing $\left(\xi=\frac{\Delta x}{\Delta t}\right)$.

Moreover, with the assumption of an isothermal ideal gas ($p=\rho c_s^2$ and $\gamma=1$), Eq. 2.40 becomes

$$f_i(\vec{x}+\Delta t \vec{\xi},t+\Delta t)-f_i(\vec{x},t)+=-\frac{\Delta t}{\tau}(f_i(\vec{x},t)-f_i^{eq}),$$

(2.41)

where f_i^{eq} is taken from Eq. 2.19 and τ is the lattice relaxation time. From Eq. 2.41 the core of the LBM algorithm is foreshadowed: the left hand side describes the propagation of the distribution function according the discretized directions in a time step, and the right hand side describes the change of the distribution function, that tends towards equilibrium with a relaxation time τ.

By performing a Chapman-Enskog expansion of Eq. 2.41 with a perturbation of the order of the Knudsen number Kn, the Navier-Stokes equations can be recovered with a kinematic viscosity related to the relaxation time [13]

$$\nu=\left(\tau-\frac{1}{2}\right)c_s^2.$$

(2.42)

where ν is the kinematic viscosity of the fluid.

2.1.6 Velocity Sets

We now seek to define the lattice configuration in order to transform the LBE into the LBM. From Eq. 2.41 we take into account that the continuous velocity is discretized and coupled with grid and time. The velocity discretization models are called Finite Discrete Velocity Models (FDVM). The most used notation to sort the different FDVMs is D<x>Q<y>, where "x" is the number of dimensions and "y" is the number of possible directions of the grid. Commonly, these models also include a null velocity component which is normally indexed as the 0th direction.

In a uniform grid, all the lattice spaces must be equidistant and additionally, a grid must fulfill symmetry in order to satisfactorily recover from the moments the macroscopic equations. In a discretized formalism, this is done by means of weighted summations with the weighting factor ω_i.
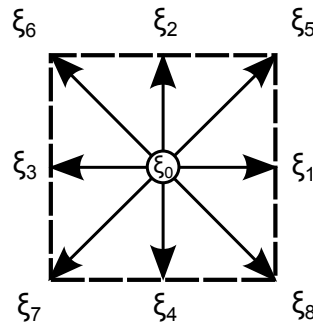
Fig. 2.1 D2Q9 model.

The D2Q9 model is the preferred FDVM in this thesis to solve the hydrodynamics of the flow. As its name indicates, it considers 9 possible velocity directions in a two dimensional space. This set sorts the velocity magnitudes into three possible levels, which are the null, orthogonal, and diagonal velocity magnitudes. From these three velocity magnitudes along with the speed of sound c_s, we can build a set of 4 equations with 4 variables [29]. Hence, the set of variables which fulfills the system of equations is shown at table 2.1. Solving the system of equations results in

Table 2.1 Set of D2Q9 velocities with its corresponding weight coefficients

i	$\vec{\xi}_i$	ω_i
0	(0, 0)	4/9
1	(1, 0)	1/9
2	(0, 1)	1/9
3	(-1, 0)	1/9
4	(0,-1)	1/9
5	(1, 1)	1/36
6	(-1, 1)	1/36
7	(-1,-1)	1/36
8	(1,-1)	1/36

$\omega_0 = 4/9, \omega_{1-4} = 1/9, \omega_{5-8} = 1/36, c_s = c_0/\sqrt{3}$.

We can further express the particle directions from Table 2.1 with aid of the vectors expressed in Eq. 2.43,

$$\vec{\xi}_i = \begin{cases} (0,0) & \text{for } i = 0 \\ \left(\cos\left(\left[\frac{\pi}{2}(i-1)\right]\right), \sin\left(\left[\frac{\pi}{2}(i-1)\right]\right)\right) \cdot c & \text{for } i \in 1-4 \\ \left(\cos\left(\left[\frac{\pi}{4}(2i-9)\right]\right), \sin\left(\left[\frac{\pi}{4}(2i-9)\right]\right)\right) \cdot c \cdot \sqrt{2} & \text{for } i \in 5-9, \end{cases} \quad (2.43)$$

A sketch of how the velocities are distributed for the D2Q9 model is shown at Fig. 2.1. Knowing the speed of sound, the thermal propagation velocity can be derived,

$$c_s = \sqrt{RT} = \frac{c_0}{\sqrt{3}} \quad \longrightarrow \quad c_0 = \sqrt{3RT}. \tag{2.44}$$

The pressure in the LBM for an ideal, incompressible gas is

$$p = \rho RT = \rho c_s^2 = \frac{\rho}{3}. \tag{2.45}$$

Eq. 2.44 is added to Eq. 2.19, resulting in the used f^{eq} for the LBGK method with the D2Q9 velocity set.

$$f_i^{eq} = \rho \omega_i \left(1 + 3 \frac{\vec{\xi}_i \cdot \vec{u}}{c_0^2} + \frac{9}{2} \frac{(\vec{\xi}_i \cdot \vec{u})^2}{c_0^4} - \frac{3}{2} \frac{\vec{u} \cdot \vec{u}}{c_0^2} \right), \tag{2.46}$$

Where $\vec{u}$ and ρ can be recovered with the sum expressed by the appropriate moments,

$$\rho(\vec{x}, t) = \sum_i f_i(\vec{x}, t) \tag{2.47}$$

$$\rho(\vec{x}, t) \vec{u}(\vec{x}, t) = \sum_i \vec{\xi}_i f_i(\vec{x}, t) \quad \longrightarrow \quad \vec{u} = \frac{\sum_i \vec{\xi}_i f_i(\vec{x}, t)}{\rho(\vec{x}, t)} \tag{2.48}$$

2.1.7 Dimensional analysis

As we know, the LBM formalism is not built upon direct physical variables. Instead it uses the so-called 'lattice units' that come from a transformation of the nondimensional quantities. The lattice framework is constrained by the assumption of incompressibility, which states that the Mach number must be kept under 0.3, and moreover, we already know that the speed of sound in the LBM is constant to $c/\sqrt{3}$. In order to understand the process of conversion of the physical variables to these 'lattice' variables, we follow and briefly explain the work proposed by Lätt [43].

First of all one must take into account three possible systems. The *physical system*, which is normally the relevant system in real applications as it expresses all the desired magnitudes of the variables in physical units (e.g. SI units). The *nondimensional system*, which is very useful in numeric simulations as it the most used system to validate the results in a dimensionless form with the respective benchmarks. Such system is also useful as an abstraction tool, because this system has a higher degree of freedom due to the characteristic variable connection between the two systems. In other words, a physical system is normally a closed one with defined magnitudes of the desired variables, however, the dimensionless system has infinite plausible possibilities, as the characteristic variables can be varied. It is also important to mention that the nondimensional numbers (e.g. Reynolds number) describe certain aspects of a system

as a whole, such as the degree of turbulence in the case of the Reynolds, and these aspects can be achieved with multiple combinations of their conforming variables. Finally, the *discrete system* is the one used to calculate the outcome and to set the input parameters of the simulations, which in our thesis, it is done with the LBM. It is important to emphasize that the nondimensional numbers are the ones that act as bridge between systems, and they must be equal when changing from a system to another. In other words the Reynolds taken from the physical units must be the same as with the Reynolds of the lattice units or the Reynolds with the nondimensional system. As an example, we will explain the process to move from a physical system to a system with lattice units.

First of all, one needs to know that we use a set of characteristic variables to move from the physical system to the nondimensional system. We choose a characteristic velocity $u_{0,p}$ and a characteristic length $L_{0,p}$. Our first step is to recover the variables in the Navier-Stokes equations in the nondimensional form. Let us first take a look at the incompressible Navier-Stokes equation without force term in physical units

$$\frac{\partial}{\partial t_p}u_p + (u_p \cdot \nabla_p)u_p = -\frac{1}{\rho_{0,p}}\nabla_p p_p + v\nabla_p^2 u_p, \tag{2.49}$$

where the subscript '0' means a reference value, the subscript 'p' means physical unit. The pressure p can be recovered from 2.45.

We first connect the physical units with their nondimensional values using the aforementioned characteristic variables.

$$\text{Re}_p = \frac{u_{0,p}L_{0,p}}{v_p} \qquad t_{0,p} = \frac{L_{0,p}}{u_{0,p}} \qquad L_p = L_d L_{0,p} \qquad u_p = u_d u_{0,p} \qquad \rho_p = \rho_d \rho_{0,p}, \tag{2.50}$$

We can infer

$$t_{0,d} = \frac{t_{0,p}}{t_{0,p}} \qquad L_{0,d} = \frac{L_{0,p}}{L_{0,p}} \qquad u_{0,d} = \frac{u_{0,p}}{u_{0,p}} \qquad \text{Re}_d = \frac{u_{0,d}L_{0,d}}{v_d} \tag{2.51}$$

From this derivation, we can directly associate the nondimensional viscosity v_d with Re_d as we can infer from Eq. 2.51 that the nondimensional reference values are always unity in the defined system and therefore $v_d = \frac{1}{\text{Re}}$.

The discretization of the nondimensional variables is performed firstly defining δx and δt, which refer to the nondimensional lattice space and time, respectively.

$$\delta t = \frac{1}{N_t} \qquad \delta x = \frac{1}{N} \tag{2.52}$$

where N and N_t are the number of nodes that conform the nondimensional characteristic length and the number of time steps needed to reach the nondimensional reference time. The choice of these parameters is bound to provide a sufficient resolution able to dissipate the weak-compressions that the LBM needs to do to calculate the density and momentum. A known constraint of these parameters is $\delta t \simeq \delta x^2$. This constraint is applied in order to keep the compressibility errors (velocity close to Ma) in the same order as the lattice errors (grid resolution) in a hypothetical refining/coarsening of the grid.

We can transform all relevant nondimensional variables into lattice units using this combination of these stated parameters and basic dimensional manipulation.

$$t_d = t_{lb}\delta t \qquad L_d = L_{lb}\delta x \qquad u_{0,d} = u_{lb}\frac{\delta x}{\delta t} \qquad v_d = v_{lb}\frac{\delta x^2}{\delta t} \qquad (2.53)$$

and knowing that the reference nondimensional velocity is unity (Eq. 2.51, we can state

$$u_{lb} = \frac{\delta t}{\delta x}. \qquad (2.54)$$

where the subscript 'lb' refers to lattice units.

The parameters Δx and Δt in Sec. 2.1.5 are the lattice spacing units. In other words, one can define them as the transformation of the dimensionless spacing and time resolution into lattice units. This can be done with the assumption of constant lattice spacing (uniform grid) with the following definition using the same procedure as in Eq. 2.53

$$\Delta x = \frac{\delta x}{\delta x} = 1 \quad \text{and} \quad \Delta t = \frac{\delta t}{\delta t} = 1. \qquad (2.55)$$

2.2 Computational Details

The previous section provided a reasonable theoretical framework of the LBM. In this section, we seek to put this knowledge into practice and to give an explanation of how to computationally implement the LBM in a computer.

The LBM stores the relevant simulation data at every node of the grid. Each node contains the information of the array of f_is, and the number of elements of this array corresponds to the number of velocities of the chosen FDVM. This information is dynamic and is propagated at every time step to the neighbouring nodes (at exception of the direction ξ_0, that remains on the same node due to its null speed). It is also possible to recover the macroscopic properties of the fluid in each node by applying Eqs. 2.47, 2.48 and also 2.42.
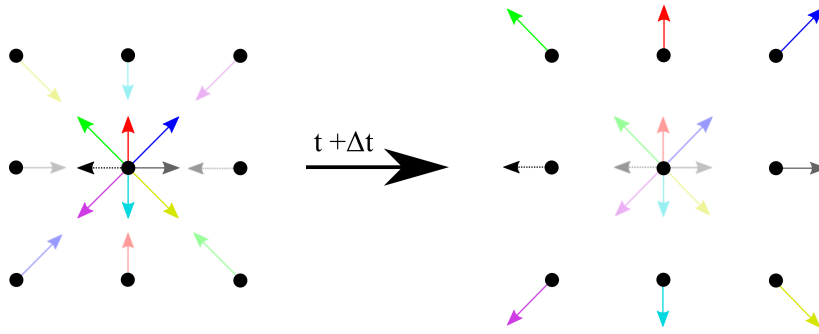
Fig. 2.2 Propagation step for a D2Q9 model.
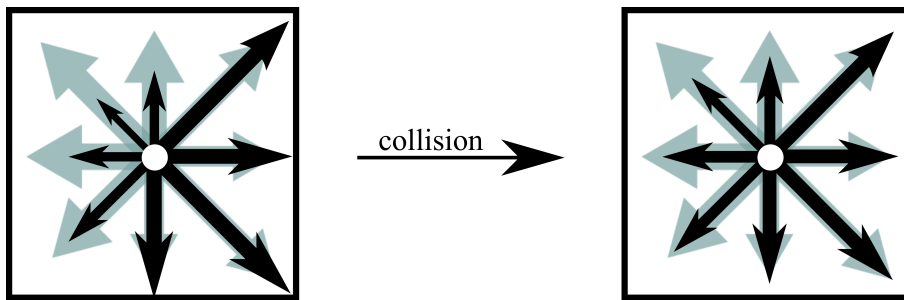
Fig. 2.3 Collision step for a D2Q9 model.

The core of the LBM algorithm consists in the *propagation* step and the *collision* step. To simplify, we show Eq. 2.41 split into these two steps, respectively.

$$f_i(\vec{x}+\vec{\xi}_i\Delta t, t+\Delta t) = \tilde{f}_i(\vec{x},t), \qquad (2.56a)$$

$$\tilde{f}_i(\vec{x},t) = f_i(\vec{x},t) + \frac{1}{\tau}(f_i^{eq}(\rho,\vec{u}) - f_i(\vec{x},t)) \qquad (2.56b)$$

where $\tilde{f}_i$ is the post-collision distribution function. Eq. 2.56a represents the propagation of the density distribution functions to their corresponding neighbouring nodes, located at $x + \Delta t\vec{\xi}_i$. Fig. 2.2 shows an example of the propagation step of a node (central black dot) relative to the attached nodes (outer black dots). Each differently coloured arrow represents a f_i in a certain direction. The semi-transparent coloured arrows are these f_is that will be moved to the central node after the streaming process, while the opaque coloured arrows represent the f_is that will propagate to the outer nodes. After the propagation step ($t + \Delta t$), the semi-transparent arrows are all shifted to the central node, and the opaque arrows now are moved to the neighbouring nodes keeping their previous directions (see the right image of Fig. 2.2. Also note that for simplicity, the magnitudes of the represented f_is in this example are all equal. Eq. 2.56b describes

the collision process. The distribution functions are modified towards its equilibrium values f_i^{eq} with a defined relaxation rate. A visual example is shown at Fig. 2.3. Black arrows are the values of each f_i, and the grey arrows are the $f_i^{eq}(\rho, \vec{u})$ values previously determined by means of Eq. 2.46 and the local macroscopic properties. On the left side of Fig. 2.3 we see all the f_i values at a given node prior to the collision and additionally we see their corresponding equilibrium values (the grey arrows). On the right side of the figure, after applying the collision step, the magnitudes of all the f_i values get visibly closer to the f_i^{eq} values.

In a typical simulation, collision and propagation steps, which represent the core of the simulation, are repeated in a closed loop to generate the desired evolution of the system, in an iterative process until a desired state is reached. In order to give a better understanding of the LBM computational algorithm, we provide a scheme of the complete computational sequence in Fig. 2.4. In order to start with the simulation, an initial state (generally the macroscopic variables) needs to be specified. Subsequently, the algorithm calculates the f_i^{eq}s with Eq. 2.46, and then the initial condition is completed by setting $f_i = f_i^{eq}$. From this point, the main loop starts and computes the f_is that are in the boundary domains and recalculates the macroscopic properties. The simulation reaches the collision step, and finally, the streaming step, which is the last part of the loop. Once is finished, the simulation restarts the loop until a specified criterion stops the simulation. Meanwhile, a periodic output can be specified to gather relevant information about the simulation. We will extensively discuss the boundary condition treatments in Chapter 3.

2.3   Secondary variables

In the previous sections, we have presented the core of the hydrodynamic LBM. We now proceed to describe other tools and implementations to give the LBM an added value, and to enable a physical interpretation to some of the simulation outputs.

The density and velocity contours of the outputs alone do not give us enough information of what happens in a simulation. In this section we provide details of the procedure used to get additional properties of the flow that are relevant for the interpretation of our results.

2.3.1   Force exerted on a bluff body and drag and lift coefficients

We aim to calculate the hydrodynamic force of a fluid exerted onto a fixed immersed body in the LBM. Let us consider a two-dimensional closed channel (see Fig. 2.5) with a velocity inlet and a pressure outlet BC as an example. It is obvious that the square
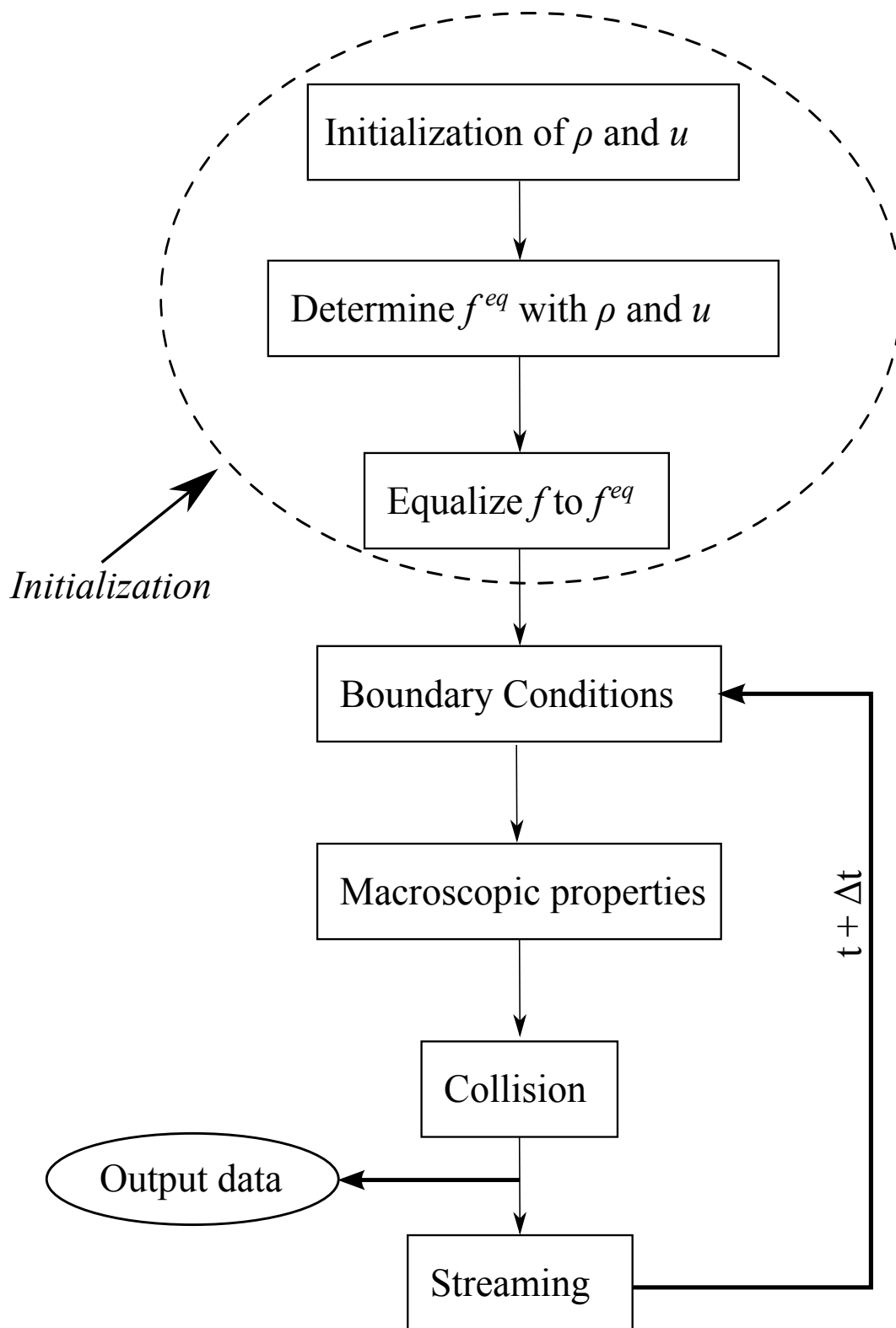
Fig. 2.4 Scheme of the lattice Boltzmann method algorithm.
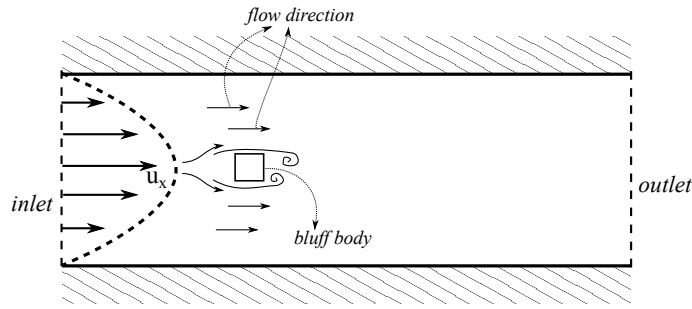
Fig. 2.5 Scheme of a closed channel with a velocity
inlet (left) and a pressure outlet (right).

obstacle placed in the channel will experiment a drag force in the direction of the fluid. In addition, a vertical force can be significant when the degree of turbulence of the flow reaches a critical value, that is a critical Reynolds. In order to proceed with our investigation we calculate these forces exerted on the fluid with an exclusive technique for LBM, which was first proposed by Ladd [41] and is named *momentum exchange method* (MEM). This explicit method calculates the force vector on a surface solely by the use of the distribution functions. The method consists in, for a desired surface Sf, summing up all of the f_is that are going to be streamed from a fluid node towards a boundary node $\vec{x}_b$ and all of the f_is that come from a boundary and go towards a fluid node $\vec{x}_f$. The mathematical expression leads to

$$F_\alpha = \sum_{\vec{x}_b \in Sf} \xi_{i,\alpha}(\tilde{f}_i(\vec{x}_f,t) + \tilde{f}_{\bar{i}}(\vec{x}_b,t)), \tag{2.57}$$

where α is the component of the force F considered and $f_{\bar{i}}$ is the opposite direction of f_i.

While this is the general form, the implementation is a lot simpler when the wall boundary is straight, placed right in the middle between two nodes and when the mid-way Bounce-Back (BB) is used. The following expression is obtained,

$$F_\alpha = 2 \sum_{\vec{x}_f \in Sf} \xi_{i,\alpha} \tilde{f}_i(\vec{x}_f,t). \tag{2.58}$$

Subsequently, the drag and lift coefficients can be calculated knowing Eq. 2.57 and Eq. 2.59

$$C_D = \frac{F_D}{\rho u_{max}^2 h}, \qquad C_L = \frac{F_L}{\rho u_{max}^2 h}, \tag{2.59}$$

where F_D and F_L are respectively, the axial and transverse components (with respect to the flow) of the force, h is the projected length of the incidence of the obstacle on the direction of the flow, and C_D and C_L are the drag and lift coefficients, respectively.

2.3.2   Strouhal number

During the simulations we encounter a periodic generation of vorticity on the wake of the obstacle at Chapter 4. In order to validate and verify if the vortex rate is in agreement with the benchmarks, the Strouhal number is used

$$St = \frac{h f_v}{u_{max}} \tag{2.60}$$

where u_{max} is the peak velocity, h is the characteristic projected length, and f is the vortex frequency.

This vortex frequency f_v can be numerically obtained by applying a fast Fourier transform (FFT) to the lift coefficient output data (Eq. 2.59, right).

2.3.3   Shear stress and shear rate

As seen in Sec. 2.1.1, the central second moment of f leads to the stress tensor (Eq. 2.8), from which one can separate the normal force and the shear force contributions. It is worth to mention that the shear stress is also locally calculated with the non-equilibrium part of the distribution functions [49],

$$\sigma_{\alpha\beta}(\vec{x},t) = \left(1 - \frac{1}{\tau}\right) \sum_i f_i^{neq}(\vec{x},t) \left(\xi_{i,\alpha}\xi_{i,\beta} - \frac{1}{2}\vec{\xi}_i \cdot \vec{\xi}_i \delta_{\alpha\beta}\right), \tag{2.61}$$

where $\sigma_{\alpha\beta}$ is the shear stress tensor, and $f_i^{neq}(\vec{x},t)$ is the non-equilibrium part of f ($f^{neq} = f - f^{eq}$). In our framework we consider an incompressible, Newtonian fluid. From this assumption, we can relate the shear stress and the shear rate directly by a proportional relation

$$S_{\alpha\beta}(\vec{x},t) = \frac{\sigma_{\alpha\beta}(\vec{x},t)}{2\rho\nu} = \left(\frac{3}{2\rho\tau}\right) \sum_i f_i^{neq}(\vec{x},t) \left(\xi_{i,\alpha}\xi_{i,\beta} - \frac{1}{2}(\vec{\xi}_i \cdot \vec{\xi}_i)\delta_{\alpha\beta}\right), \tag{2.62}$$

where $S_{\alpha\beta}$ is the shear rate tensor which can be then transformed into a scalar

$$\dot{\gamma}(\vec{x},t) = 2\sum \sqrt{S_{\alpha\beta} \cdot S_{\alpha\beta}}. \tag{2.63}$$

2.4   LBM passive scalar model

LBM is also useful to simulate systems where a passive scalar that acts as a solute in a fluid system is transported using the advection-diffusion equation (ADE) [13].

$$\frac{\partial C}{\partial t} + \nabla \cdot (\vec{u}C) - \nabla \cdot (D\nabla C) = S \tag{2.64}$$

where C is the solute concentration, $\vec{u}$ is the local velocity and D is the diffusivity of the solute species C.

The passive scalar is coupled to the flow field by the advective term at Eq. 2.64.

In order to fulfill the governing ADE in the LBM framework, we use a similar procedure as that used in Sec. 2.1. In this case, we introduce a new density distribution function for the concentration g, from which we recover the local concentration by applying the corresponding zeroth moment. First of all let us consider the discretized evolution equation with a general collision operator

$$g_i(\vec{x} + \vec{\xi}_i \delta t, t + \delta t) = \tilde{g}_i(\vec{x}, t) + \sum_j \Omega_{ij,c}(g_j(\vec{x}, t) - g_j^{eq}(\vec{x}, t)) \tag{2.65}$$

where the collision operators $\Omega_{ij,c}$ can be taken as in Sec. 2.1.4. The collision operators of SRT and MRT read, respectively,

$$\Omega_{ij,C} = -\frac{1}{\tau_c} \tag{2.66}$$

$$\Omega_{ij,C} = -M_c^{-1} S_c M_c \tag{2.67}$$

where τ_c is the relaxation time for the species C, M_c is the moment matrix and S_c is the matrix with the relaxation times for each individual moment.

The macroscopic concentration C can be recovered with the zeroth order moment as in Eq. 2.47

$$C(\vec{x}, t) = \sum_i g_i(\vec{x}, t). \tag{2.68}$$

For a SRT model, the evolution equation reads

$$g_i(\vec{x} + \vec{\xi}_i \delta t, t + \delta t) = \tilde{g}_i(\vec{x}, t) - \frac{1}{\tau_c}(g_i(\vec{x}, t) - g_i^{eq}(\vec{x}, t)) \tag{2.69}$$

while for the MRT model it reads

$$g_i(\vec{x} + \vec{\xi}_i \delta t, t + \delta t) = \tilde{g}_i(\vec{x}, t) - M_c^{-1} S_{C,j}(m_{j,c}(\vec{x}, t) - m_{j,c}^{eq}(\vec{x}, t)). \tag{2.70}$$
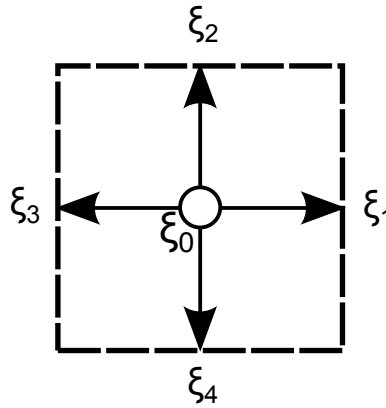
Fig. 2.6 Finite discrete velocity model "D2Q5".

Both of these equations have the same structure as Eqs. 2.41 and 2.27.

In this section, nevertheless, we will focus on developing the MRT model, as it is more stable than the SRT model and we will definitely need that plus of stability. For this purpose, we consider the D2Q5 model (see Fig. 2.6) for the concentration because, unlike the case of the momentum transfer equation, it is enough to recover the macroscopic concentrations with it. The velocity set of the D2Q5 model is

$$\xi_i = \begin{cases} (0,0) & \text{for} \quad i = 0 \\ \left(\cos\left(\left[\frac{\pi}{2}(i-1)\right]\right), \sin\left(\left[\frac{\pi}{2}(i-1)\right]\right)\right) \cdot c & \text{for} \quad i \in 1-4 \end{cases} \tag{2.71}$$

We consider the moment matrix M_c [45, 53]

$$M_c = \begin{pmatrix} 1 & 1 & 1 & 1 & 1 \\ 0 & 1 & 0 & -1 & 0 \\ 0 & 0 & 1 & 0 & -1 \\ -4 & 1 & 1 & 1 & 1 \\ 0 & 1 & -1 & 1 & -1 \end{pmatrix}, \tag{2.72}$$

where the relaxation time τ_c is related to the mass diffusivity of species C

$$D_c = \frac{(4+k)}{10}\left(\tau_c - \frac{1}{2}\right). \tag{2.73}$$

The quantities $m_{j,c}$ in Eq. 2.70 are the distribution functions in the moment space, which are obtained with the transformation matrix $M_{j,c} \cdot g_j = m_{j,c}$. The equilibrium

moments for Eq. 2.70 are

$$
\begin{aligned}
m_{0,c}^{eq} &= C \\
m_{1,c}^{eq} &= u_x C \\
m_{2,c}^{eq} &= u_y C \;, \\
m_{3,c}^{eq} &= kC \\
m_{4,c}^{eq} &= 0
\end{aligned}
\tag{2.74}
$$

where k is a parameter that needs to be smaller than one in order to keep the simulation from "checkerboard" instabilities [70].

The relaxation matrix is

$$
s_{0,c} = 0 \tag{2.75a}
$$

$$
s_{1,c} = \frac{1}{\tau_c} \tag{2.75b}
$$

$$
s_{2,c} = \frac{1}{\tau_c} \tag{2.75c}
$$

$$
s_{3,c} = \frac{1}{\dfrac{1}{6(\tau_c - 0.5)} + 0.5} \tag{2.75d}
$$

$$
s_{4,c} = s_3 \tag{2.75e}
$$

$$
\tag{2.75f}
$$

As in the MRT procedure to compute the flow field, this one can also be converted into the SRT model by equating the elements of the diagonal relaxation time matrix to $\frac{1}{\tau_c}$,

$$
S_c = \frac{1}{\tau_c} \mathbf{I}. \tag{2.76}
$$

2.5   Growth model for platelets

We have seen throughout this chapter some implementations that aim to compute variables like forces on a boundary, or local shear forces in a LBM model. The additional target of these implementations is to enhance the passive scalar model for LBM. Now we try to develop a good set of tools to implement a full growth model for human platelets. The model adopts some general rules that can be useful for other applications such as dendritic growth [50] or clogging in porous media through mass transport and reaction [77].

Blood is a colloidal system composed of mainly plasma and blood cells. As a matter of fact, this mixture is a very complex system to predict due to its sensitivity to many factors. Numerous hemodynamic computations and experimental set ups

have been trying to understand and predict the blood cell distribution under diverse conditions [20, 24, 68].

It is proven that the platelets experiment a lateral migration towards the vessel walls. A well established hypothesis states that platelets passively migrate to the walls in response to the combination of the flow shear rate and the red blood cells (RBCs) presence [27], which are much bigger than platelets. Specifically, the shear rate enhances the RBCs to deform and they tend to concentrate on the center of the vessels. Thus the platelets tend to stay close to the walls, due to the fact that the available volume fraction at the centerline of the channel is mostly occupied by the red blood cells.

When it comes to study the hydrodynamic flow and blood cell transport, one possible way is to consider the RBCs and the platelets as physical entities that interact reciprocally with the fluid. One accurate and popular technique is called the immersed boundary method (IBM). This technique, which is also used in LBM [15, 21, 22], uses a Lagrangian grid for each considered particle membrane in the system and models the interaction of the forces exerted on each membrane separately. Nevertheless, there are also other techniques that use the advection-diffusion equation to determine the platelet transport as a continuum solute mixed with the plasma, due to the low Stokes number of platelets. This is obviously an approximation and does not consider the possible interactions of the platelets with the hydrodynamic field.

The platelet transport problem becomes much more complicated when is coupled with a clotting process. There exist extensive reviews about the state of the art of this problem [14, 74]. Specifically, Cito et al. state that LBM is suitable to deal with this multi-scale problem. Focusing on the LBM, Bernsdorf et al. [9] provide an "aging" clot model based on tracking a passive scalar transport with governing advection-diffusion equations (ADE). A similar work by Harrison et al. [31] traces the age of the platelets and its concentration to create the clotting phenomenon. In another work, Harrinson et al. consider another aging clotting model that also requires of the shear stress threshold for the activation of platelets [30]. The aggregation of RBCs was also considered in the LBM by means of a shear stress threshold clotting model for stented arteries with aneurysms using a passive-scalar suspension model RBC transport [56]. Recently, Malaspinas et al. presented a work where the clotting platelet function is implicitly considered with the modeling of several proteins with a Lagrangian point particle model where, in order to make this a feasible problem, the transport of these point-like particles was determined with a first order Euler scheme in detriment of the ADE.

Most of the LBM cited works are preliminary clotting models that can be eventually applied to the coagulation of blood. These approaches additionally need to simplify

the reaction cascade that takes place and only consider a primary platelet plug with an heuristic model –the triggers are the shear rate and aging factors instead of the reaction of the chemical species that participate in blood clotting processes, such as thrombin, von Willebrand factor, collagen, etc.

On top of that, it is non-trivial to couple both hydrodynamic and solute transport LBM meshes in the range of typical human artery diameters (1cm-0.1mm), due to the difference of scales between both processes (both relaxation times are 2-3 orders of magnitude distant). This issue is a consequence of a very high Péclet number which is translated into a very thin material transport boundary layer and this ends up in elevating the computational resources required for an acceptable accuracy of the mass transport at the walls.

As a result, many different approaches have been coupled to the lattice Boltzmann method to deal with the species transport, treated as passive scalars or by tracking the suspended particles individually, while the LBM computes the hydrodynamics of the system. On the other side, this problem of scale separation is not so relevant when the scale of the problem is reduced to lesser physical problems, such as stenosed arterioles [25].

It is still needed to explore the feasibility, development and understanding of the limitations of using the LBM within this framework. Therefore, in this thesis, we consider the coupling of the hydrodynamic and passive scalar models in LBM for a human coronary artery. We will describe the developed tools towards the creation of a preliminary growth model suitable for thrombus formation in the following sections.

2.5.1 Enhanced diffusion

A colloidal system under shear forces can experiment changes in its hydrodynamic state (shear thinning) and the diffusion of the species. The constant (e.g., shear independent) diffusion for a given species is,

$$D_{th} = \frac{k_{th}T}{6\pi\mu R_{eq}}, \tag{2.77}$$

where k_{th} is the Boltzmann constant, μ is the dynamic viscosity of the fluid and R_{eq} refers to the radius of the equivalent sphere of the particle. Hence, this thermal diffusion is not sufficient to describe the solute transport in a particulate suspension. In fact, the diffusion of the platelets is enhanced with the shear rate of the fluid [69, 71]. Zydney and Colton [80] developed a mathematical model to describe this concept. The correlation reads

$$D_e = k_d a^2 \phi(1-\phi)^n \dot{\gamma} + D_{th}, \tag{2.78}$$

where ϕ is the local hematocrit, a and k_d are constants related to the scale of the particle collisions and to the enhanced diffusion, respectively, and n is another constant within $0.5 \leq n \leq 1.1$.

The platelets present a spontaneous peak concentration near the artery vessels, which coincides with the maximum shear rate zone of a blood vessel. If this model is applied, one can infer that the maximum diffusion will also be located close to the wall. Therefore, something else must be pushing against the diffusion flux to create such concentration gradients near the wall, we discuss this issue in the section below.

2.5.2   Margination effect

It is proven that the distribution of blood cells in the arteries is bound to a specific pattern which differs from the elementary uniform concentration, typical of a diffusive/convective system. Platelets are rigid and discoid particles that are transported along the blood vessels with a pulsated flow. Such flow is laminar and has a significant shear rate which will depend mainly on the size of the vessel and the flow rate. In fact, if the platelets are examined without the presence of the RBCs, they also experiment a noticeable lateral migration from the centre of the channel due to the called Segré-Silberberg effect [1]. After adding the RBCs to the system, platelets are further pushed to the walls and can reach proportions of 17 times the average concentration of platelets near the wall. This fact stresses the necessity to model with non-uniform distributions of platelets when considering the blood clotting process as a reaction-diffusion problem, as there are strong gradients of concentration at the walls. On the other hand, RBCs collide and are deformed at a rate that is described mainly by the shear rate, and present a higher concentration at the centre of the channel [27, 38, 68]. In summary, platelets passively migrate to the walls in response to the shear rate, the viscosity, and the hematocrit conditions. In fact, it is remarkable that this natural behaviour is crucial for an effective coagulation and preservation of RBCs when a vessel rupture occurs. There exist some techniques that mimic this concentration distributions. Eckstein and Belgacem were the first ever to implement a drift term as an additional term for the Fick's law related to a potential field. Bark et al. [38] used a similar approach for both the platelets and the RBCs which included a drift term in the ADE. A different approach was used by Zàvodszky et al., which applied a fictitious force based on the negative gradient of the shear stress. In this thesis, we develop a drift force model based on the potential field, by explicitly applying a force term on the distribution functions of the species.

$$\vec{\zeta}_i(C_{p,eq}) = D_p(\vec{x})\frac{1}{C_{p,eq}(\vec{x},R)}\frac{\partial C_{p,eq}(\vec{x},R)}{\partial x}M_{cd},\tag{2.79}$$

where $\vec{\zeta}_i(C_{p,eq})$ is the drift term, M_{cd} is a conditioning constant that amplifies the drift term and $C_{p,eq}$ is the potential field where the platelets would go spontaneously. We arbitrarily set the potential field for the platelets to be as in Bark's work [38]

$$C_{p,eq}(y,R) = \left(\frac{4\beta^2 \bar{C}_p}{(1+\tanh\left[\beta\left(y/R - \delta_p\right)\right])\lambda\left[2\beta^2 - e^{2\beta(\delta_p - 1)}(2\beta - e^{2\beta} + 1)\right]} \right), \tag{2.80}$$

where R is the non-occluded width of the channel, β and δ are constants used to shape the hyperbolic tangent, y denotes the radial vertical position and λ is a normalisation constant that scales the total surface averaged concentration to unity in non-dimensional units. We can see that the distribution of platelets will only depend on the transversal position y and the total radius R.

This potential concentration profile can be considered as time dependent as long as there is any source that modifies the radius of the channel, such as a thrombosis phenomenon (see Sec. 2.5.3). It is important to remark that this drift term is only considered for the lateral migration, and hence, the axial contributions have not been taken into account in this model.

The calculated drift term is then considered as a source term added to the collision step of the lattice Boltzmann algorithm,

$$\tilde{g}_i(\vec{x},t) = g_i(\vec{x},t) + \sum_j \left(\Omega_{ij}(g_j(\vec{x},t) - g_j^{eq}(\rho,\vec{u})) \right) + \omega_i \vec{\zeta}_i(C_{p,eq})C_p(\vec{x},t). \tag{2.81}$$

As we can see in Eq. 2.81, the drift term is applied explicitly to the vertical distribution functions. Note that $\vec{\zeta}_i$ is dependent on the i-direction considered. This means that the magnitude of the drift term changes over the different considered g_is. This can provoke a mass imbalance, which is very likely to happen due to the hyperbolic nature of $C_{p,eq}$. To solve this issue we consider a second order centred stencil for the spatial derivatives in Eq. 2.79. With this differential stencil and regarding that only the vertical directions are considered, we can guarantee that the drift term is invariant. To exemplify this latter statement, if we imagine our D2Q5 model, there are only two directions with vertical components available in this model, hence the centred approximation will only change the sign of $\vec{\zeta}$ from one direction to another. In other words, it will subtract some value $\vec{\zeta}_i$ from g_i and add this very same value to $g_{\bar{i}}$, keeping the mass balance (same concentration) unchanged.

2.5.3   Thrombosis phenomenon

We aim to develop a growth model able to recreate at some extent a thrombosis model using both hydrodynamic and solute transport models in LBM. We will give a brief review of the phenomenon of thrombosis and we will propose the tools for a possible implementation of this phenomenon in LBM.

Thrombosis is the formation of a blood clot (thrombus) inside a blood vessel of the circulatory system. This phenomenon normally occurs during the coagulation process, which this latter is triggered when a blood vessel is damaged. The blood clot that forms during the coagulation is normally reabsorbed in a healthy blood vessel. However, the thrombosis has the risk of total occlusion of the vessel if it happens in an artery with the atherosclerosis disease. A total occlusion of an artery can be deadly in certain areas of the vascular system (e.g., in a human coronary artery or inside the brain blood vessels).

Along with thromboembolism (a dislodged thrombus that occludes another down-stream artery), the thrombosis-derived diseases are currently the first cause of human death over the world. It is certainly obvious that it is a priority to invest more research to deeply understand the thrombosis phenomenon. Specifically, we want to focus our study on the platelets, which play an active role during the coagulation.

Platelets move within the arteries, where in normal conditions, present a near-wall excess due to their natural lateral migration (see Sec. 2.5.2). This phenomenon enhances their clotting ability. When there is physical tissue damage, the exposed part of the subendothelium contains high amounts of collagen and von Willebrand factor that, in contact with platelets, cause them to get stuck and activated. Gradually, platelets stack and cover the damaged area in the coagulation step called *deposition*. Then, platelets become activated with the aforementioned coagulation factors. They change their shape, expand in a branch-wise way and release other coagulation factors that enhance the attraction and deposition of more platelets. These coagulation factors, mainly thrombin, further activate the resting platelets that are stuck on the damaged region, leading to a feedbacked reaction which is called thrombin burst. As a result, a significant amount of platelets and other blood cells get stuck in an loose primary plug in the called *aggregation* step. Finally, due to the vasoconstriction and the plug volume itself, the shear rate is gradually augmented in the damaged zone, leading to the activation of other coagulation factors (mainly fibrin) that stabilise the clot. After hemostasis is finally reached, the clot is gradually dissolved by plasmin and later reabsorbed by the body, leaving the damaged zone prepared to be fully repaired.

Platelets are therefore only the tip of the iceberg of a much more complex process, which involves the understanding of multiple topics, such as hydrodynamics, bind-

ing reaction kinetics, multicomponent flow, membrane interaction, etc. Despite the platelets, there are more than a dozen of other factors involved in the regulation of the clotting process. Hence it is usual to find works that partially reduce this coagulation cascade into the main agonists: platelets and thrombin. An example can be the work by Bedekar et al. [7], which uses the transport equations to model the platelets (whether they are resting, activated or bound to a surface), thrombin, prothrombin and antithrombin, which intend to mimic the platelet steps of deposition and aggregation. In another different approach of thrombus growth modelling, Bark et al. [6] proposed an interesting way to simplify a significant part of the coagulation phenomenon. They provided a correlation based *in vitro* experiments of an stenosed tube with an reactive part. This experimental fit relates the lag time of platelets to reach the aggregation step to a power law function dependent to the shear rate. They assume that the platelets need a time in order to be deposited and subsequently be activated in order to start the thrombin burst phenomenon that conforms the aggregation step. As a result, their model accurately fits the experimental results with a relatively easy approach. Later on, in another work, Bark et al. [38] used the same technique combined with a computational model to describe the thrombus growth under several stenosis and elevated shear rates using the ADE with platelets and RBCs. For the reader's information, it was also previously stated that the platelets adhesion is enhanced with the shear stress [2].

In our model, we will describe the coagulation process by considering the platelets as a continuum solute species, using the Eq. 2.64 as the governing equation and considering a source term S_p as a sink of platelet concentration. The source term can be considered as a first order reaction sink term

$$S_p = k_{rt}C_{p,rw} \, , \tag{2.82}$$

where k_{rt} is the reaction rate constant. The reaction takes place at the fluid nodes attached to the wall nodes that are either thrombus or the "damaged surface" nodes. This sink term S_p is considered as a flux of platelets that deposits on the reactive fluid nodes.

Since we assume the platelets to be a continuum medium with a relatively low Stokes number, the reaction rate can be also decoupled from the hydrodynamics. The derivation of S_p becomes straightforward by assuming that each node is a perfectly mixed batch reactor. The reaction term is explicitly calculated in the LBM with a Neumann boundary condition, which is discussed later in Chapter 3.

In such conditions, the Sherwood number is typically used to describe the transport at the boundary wall

$$\text{Sh}(\vec{x}) = \frac{N''(\vec{x})\delta_f}{C_0 D_p},\tag{2.83}$$

where $\text{Sh}(\vec{x})$ is the local Sherwood, $N''(\vec{x})$ is the local mass flux due to the reaction (S_p), δ_f is the active surface length where the reaction occurs, C_0 is the concentration out of the mass transport boundary layer and D_p is the diffusion coefficient of the platelets. The Sh indicates the overall mass transport rate over the diffusion rate.

We can analytically determine the Sherwood number assuming a constant shear rate on the mass transport boundary layer [3, 57] to validate the proposed reaction-advection-diffusion model.

$$\left.\begin{array}{c} \text{Sh}(\vec{x}_d) = \text{Da}\dfrac{3^{3/2}}{2\pi}\int_0^\infty \dfrac{exp[-(\alpha b)]^3}{1+b+b^2}db \\[2mm] \alpha = \dfrac{\Gamma(1/3)}{3^{1/3}\Gamma(2/3)}\left(\dfrac{\text{Da}^3}{\text{Re}_{\delta_f}^2\,\text{Sc}}\vec{x}_d\right) \end{array}\right\},\tag{2.84}$$

where $\text{Da} = \frac{k_{rt}C_0}{D_p}$ is the Damkhöler number, $\text{Re}_{\delta_f} = \left(\frac{\dot{\gamma}}{\nu}\right)^{1/2}\delta_f$ is the Reynolds number based on the shear rate of the model and the surface reaction length, Γ is the Gamma function, ν is the kinematic viscosity of the blood, $\text{Sc} = \nu/D_p$ is the Schmidt number of the model and $\vec{x}_d$ is the nondimensional position of the reactive surface.

This correlation is limited to a steady state and constant shear rate. We assume that the mass transport boundary layer is much smaller than the momentum boundary layer, and therefore this assumption is presumed to be valid.

Once the platelet reaction rate is controlled and validated, we move forward to the last essential step to develop a basic thrombosis model: the transformation of the reacted platelet species into a solid static boundary attached to the wall surface/thrombus.

The depletion of platelets (the sink term) can be counted and accumulated at each time step in a separate memory grid during the simulation. When the accumulated volume fraction of platelets in a reactive node reaches the 80% the node is converted into a thrombus node. The 80% threshold corresponds to the packing factor of the platelets [72]. Fig 2.7 describes the computational scheme of the reactive wall conversion to thrombus wall. From Fig. 2.7, the white coloured cells correspond to the normal fluid nodes, the grey coloured cells correspond to the reactive zones and the yellow coloured cells are either the thrombus or the vessel wall. In the fluid zone, the normal hydrodynamics and the former Eq. 2.81 without reaction are applied. On the non-reactive wall channel nodes, normal mid-way no-slip BB is applied, and finally, on the reactive nodes (thrombus or active nodes), the reaction boundary condition is applied with the procedure explained in Sec. 3.2.1. The total accumulated platelet
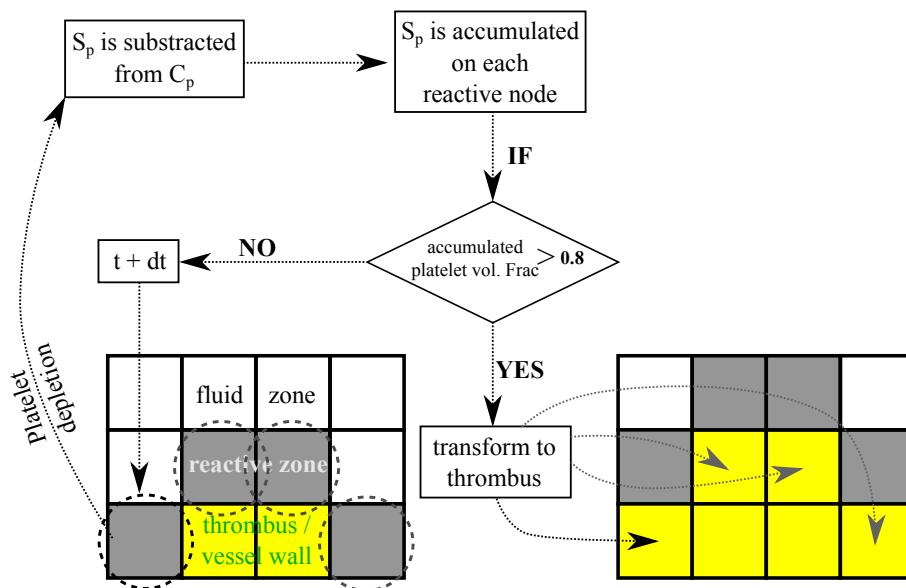
Fig. 2.7 Sketch of the computational region. From a fluid node towards a thrombus node.

concentration is transformed into volume and divided by the volume of a fictitious cell (taking into account the lattice spacing Δx from Sec. 2.1.7).

2.6 Code and tools

The simulations performed for this thesis were done in *FORTRAN 90* inspired on the Palabos code [46]. Drag and lift forces and the Strouhal number were obtained by importing the data into the open-source SCILAB® software, and the results were visually enhanced by using the plotting tool GNUplot®. The visualisations of the streamlines, the velocity, density and concentration fields were displayed using the open-source software Paraview® software.

The recirculation length was obtained by measuring the distance between the centre of the obstacle and the stagnation point behind the two vortexes at the rear of the obstacle. This stagnation point is determined by means of the velocity streamlines displayed in Paraview®, and then presented by means of the GNUplot® tool.

Chapter 3

LBM Boundary Conditions

The purpose of the computational fluid dynamic (CFD) simulations is to predict the behaviour of a desired fluid system. Such systems usually are at a non-steady state that can be provoked by many factors (e.g. bluff objects, domain limits, high turbulence). The calculation of the flow properties at a boundary node can not be done using the same procedure as for inner nodes; appropriate boundary conditions need to be specified for the hydrodynamic problem to be well-posed and therefore the elemental equations governing the fluid dynamics can not be applied at the boundaries. Numerically, the boundaries of a given domain are generally crucial and need to be carefully treated in order to mitigate possible artificial errors. Indeed, LBM is not exempt of this issue.

As a matter of fact, an ideal LBM BC would be able to provide macroscopic values at the boundary nodes as if they were calculated by the elemental fluid equations without generating any perturbation. However this is theoretically impossible to achieve, as the problem is underdetermined due to the lack of information that is inherent to such domain boundaries. We show Fig. 3.1 as an illustrative example of what happens with the information at the boundaries of a simulation domain in the LBM. In the streaming step, the values of the *non-existing incoming velocity populations* from the outside of the computational domain need to be artificially generated in order to calculate the macroscopic variables, and therefore, to proceed with the simulation. The magnitude of these new distribution functions needs to be in concordance with the information from the bulk in order to minimise the impact of the boundary on the simulation. There exist many types of boundary conditions that efficiently generate or modify the f_i values. The complexity of the implementation of these BCs will depend on the nature of the system and the desired accuracy of the fluid properties at the boundary. There are usually two ways to obtain the unknown populations coming from the boundaries. One can first fix or predict a desired set of
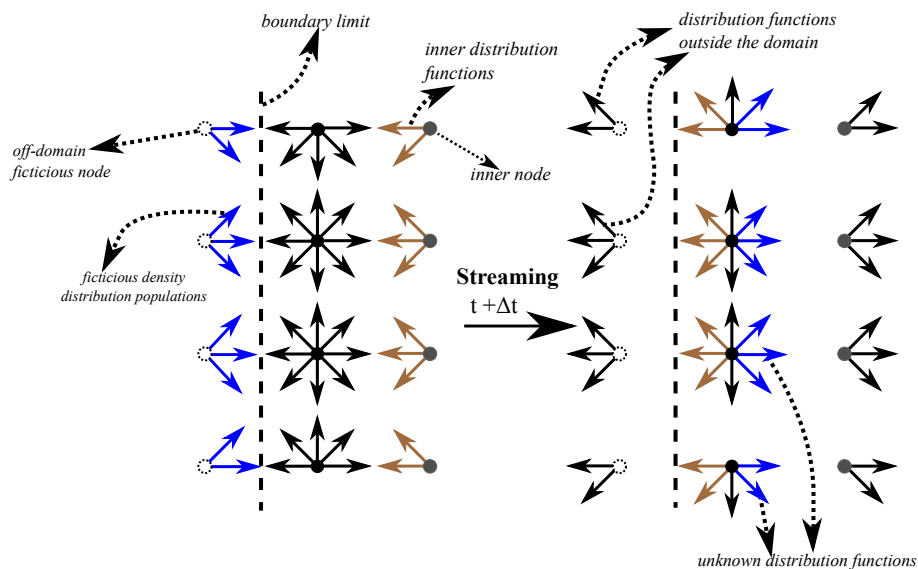
Fig. 3.1 Density distribution functions before and after the streaming
step at a given boundary.

macroscopic properties at the boundary node and then calculate the corresponding
unknown populations. The other way is just to take the opposite path. First, one can
calculate the unknown populations under some assumptions and then the macroscopic
properties are normally computed with Eqs. 2.47, 2.48 and 2.68.

Throughout this thesis, we have used a significant amount of different BCs. There-
fore, we found relevant to dedicate a separate chapter for them. We first introduce
a general classification of the BCs, which applies to the whole field of CFD and we
subsequently list and describe each of the BCs used in our approach.

3.1   Classification of boundary conditions

In CFD problems, BCs can be classified in four categories. Firstly, the *periodic
boundary conditions*, which are relatively easy to implement. Due to its simplicity,
they are often used in tests and preliminary simulations. The purpose of this type of
BC is to transport the populations that are about to leave the domain to the opposite
site of the domain in the direction of motion (see Fig. 3.2). Its is a well-known way
to reproduce a part of a whole, homogeneous system in a smaller domain, which
can reduce dramatically the required computational effort. The *Dirichlet boundary
condition*, which is probably the most popular type, fixes a macroscopic variable at the
boundary $-\vec{U}$, for example,

$$\vec{U}(\vec{x}_w) = a, \tag{3.1}$$
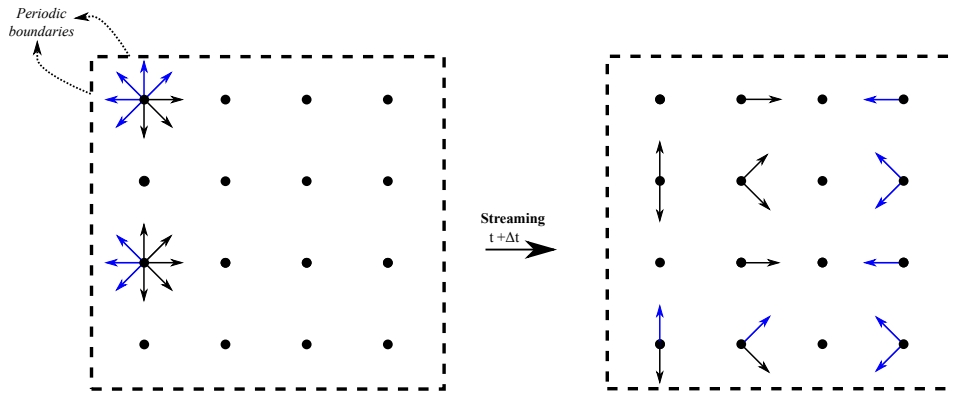
Fig. 3.2 Density distribution functions before and after the streaming step at a given periodic boundary.

where a is a predefined value and $\vec{x}_w$ is the local position of the boundary wall. They are vastly used for flow velocity BCs, as well as in pressure BCs or even to mimic walls, with the so called no-slip BC, which sets the velocity at the boundary to zero $(\vec{u}(\vec{x}_w) = 0)$.

On the other side, the *Neumann boundary condition* fixes the derivatives of $\vec{U}$ to a fixed value, as shown at Eq. 3.2

$$\frac{\mathrm{d}\vec{U}(\vec{x}_w)}{\mathrm{d}\vec{x}_n} = a, \tag{3.2}$$

where again a is a predefined value, $\mathrm{d}\vec{x}_n$ is the normal distance between the fluid node $\vec{x}_f$ and the physical location of the boundary wall $\vec{x}_w$. Neumann boundary conditions are normally used as a flux condition, such as sources or sinks of $\vec{U}$ (e.g. reaction heat, reaction of a solute, adiabatic walls, etc).

The last group is that of more complex boundary conditions, also called *third type boundary conditions* such as the *Robin boundary conditions*. The Robin BCs determine a boundary value problem by solving a linear combination of a Neumann and a Dirichlet BCs. The mathematical form of the Robin is expressed in Eq. 3.3, respectively.

$$a_1 \frac{\mathrm{d}\vec{U}(\vec{x}_w)}{\mathrm{d}\vec{x}_n} + a_2 \vec{U}(\vec{x}_w) = a_3, \tag{3.3}$$

where a_1, a_2, a_3, a_4, a_5 are constants. One popular Robin BC can be a convective BC.

There exist other more complex boundary conditions that are classified in *higher order types*, but we will skip its explanation as they are not used in this thesis.

3.2 Bounce-back/specular boundary conditions

In the LBM, there is an explicit way to set a wall, which is done by means of different types of *bounce-back rules*. This implementation consists in generating the unknown population values directly from the outgoing density distribution functions. Another important feature from this implementation is that it can provide second order accuracy when the boundary is exactly in the middle of a link between two nodes [26]. Lets then further analyse the possible types of bounce-back (BB), specular reflection rules and their corresponding features.

One popular and straightforward way to determine the unknown distributions with the BB rule is to to do a *full-way* bounce-back. This technique basically applies to the outgoing populations that cross the solid boundary. After reaching a wall node ("ghost node" in Figs. 3.3), these populations are reoriented and sent back to the domain in the next streaming step. The incoming populations from the ghost nodes conform the aforementioned unknown populations. This method therefore demands of two streaming steps to fulfil both no-slip and free-slip BCs. This feature can be clearly understood by looking at Figs. 3.3 and 3.4, respectively. For a no-slip wall (see Fig. 3.3), the blue arrows in the rightmost picture are the result of the outgoing populations from the leftmost picture. Even though this scheme is popular for its simplicity, it is not flawless, as it is not strictly mass-conservative. This is due to the delay of a full time step elapsed between the leaving of the outgoing populations and the corresponding entering of the incoming populations. Thus, these incoming and outgoing populations do not need to necessarily be the same, and therefore, they can differ in magnitude when the no-slip condition is completed,

$$f_{\bar{i}}(\vec{x}_b, t) = \tilde{f}_i(\vec{x}_b, t), \tag{3.4}$$

where $\vec{x}_b$ is the wall node which is attached to a fluid node, $\bar{i}$ is the opposite direction of the velocity i, and $\tilde{f}$ represents the post-collision distribution function. Therefore, this method just changes the direction of $f_i(\vec{x}_b, t)$ into $f_{\bar{i}}(\vec{x}_b, t)$ in an algorithm that is fully independent of the streaming step. For a free-slip case, the same treatment is applied, but instead of a total reflection, the outgoing populations are reoriented with a specular reflection (see Fig. 3.4). The effect of this reflection is equivalent to setting the normal velocity component to zero and the gradient of the transversal velocity to zero, which can be interpreted as a Dirichlet BC for the normal velocity component, and a Neumann BC for the parallel velocity component. The computational formulation is similar to Eq. 3.4,

$$f_{\bar{\bar{i}}}(\vec{x}_b, t) = \tilde{f}_i(\vec{x}_b, t), \tag{3.5}$$
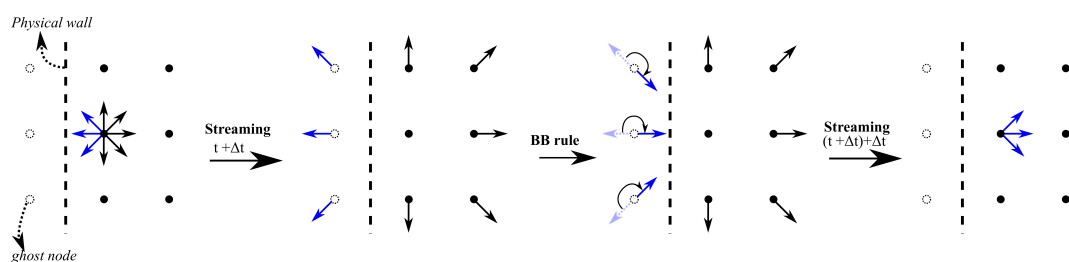
Fig. 3.3 Full-way bounce-back scheme on a no-slip wall.
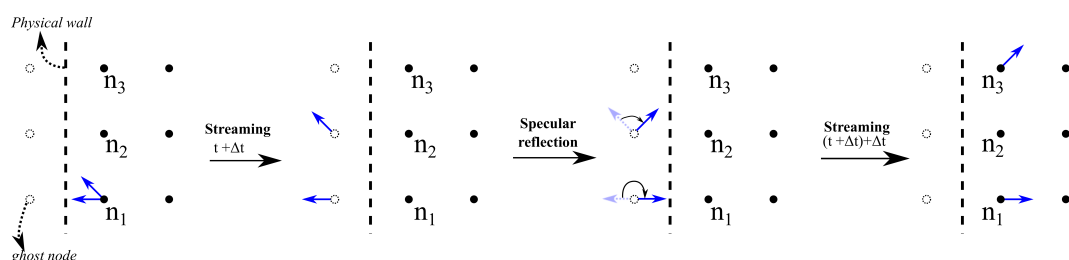
Fig. 3.4 Full-way bounce-back scheme on a free-slip wall.

where $\bar{\bar{i}}$ represents the specular reflection of the i direction, according to the orientation of the boundary. In summary, we can assume that in addition to its simplicity and its independence from other routines, the full-way BB scheme provides a fully local computational procedure. Nevertheless, one can notice that this procedure is done on a node out of the fluid domain. Another feature of full-way BB method is that the distribution functions that are under this BB rule *skip* the collision step. Unlike the full-way BB, the *mid-way* BB does conserve the mass balance at the boundary. In this case, the BB rule is directly applied within a single streaming step, which means that the particle distribution will travel a distance of a full node. Therefore, as its name suggests, the mid-way BB rule considers that the physical boundary is located right in the middle between the fluid node and the ghost node. This fact makes the mid-way BB to be second order accurate in space. We show in Figs. 3.5 and 3.6 sketches of how the midway scheme works. In fact, during the computational routine, this scheme is performed during each streaming step. The outgoing populations (blue arrows) are stored. Subsequently, the streaming step is performed for all the other populations, and finally, the stored populations that leave the domain are reoriented and replaced in the prescribed directions.

The procedure of the mid-way no-slip BC is fully local and fulfils the idea of *bouncing back* the particles to their original node in one single stage. However, Fig. 3.6 reveals that the free-slip BC with this scheme is forced to be non-local, as the density distributions that have a direction component parallel to the boundary are
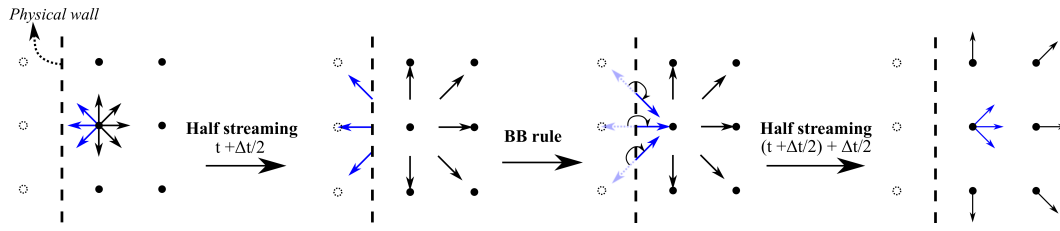
Fig. 3.5 Mid-way bounce-back rule on a no-slip wall.
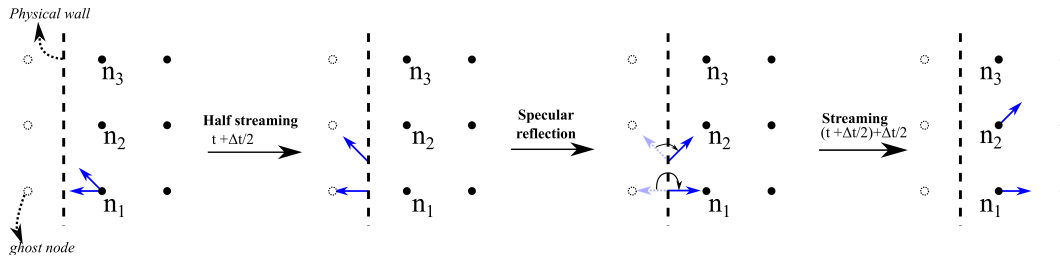
Fig. 3.6 Mid-way bounce-back rule scheme on a free-slip wall.

streamed back towards different nodes. Specifically, with the mid-way technique, the f_is with velocities with a parallel component to the wall are shifted one node at the end of the specular reflection procedure (from n_1 to n_2). The general formulation of the mid-way no-slip BB was proposed by Ladd [41]

$$f_{\bar{i}}(\vec{x}_f, t + \Delta t) = \tilde{f}_i(\vec{x}_f, t) - 6\omega\rho(\vec{\xi}_i \cdot \vec{u}_w), \tag{3.6}$$

where $\vec{x}_f$ is a fluid node attached to a wall node, and $\vec{u}_w$ is the velocity of the wall. If we consider a steady wall ($\vec{u}_w = 0$), the right term is nullified. It is important to notice that the no-slip mid-way BB with a steady wall is applicable to both hydrodynamic and passive scalar distribution functions,

$$h_{\bar{i}}(\vec{x}_f, t + \Delta t) = \tilde{h}_i(\vec{x}_f, t), \tag{3.7}$$

where h_i can be either f_i for momentum transfer problems, or g_i for heat or mass transport processes. Meanwhile, if we want to fix a certain value of a passive scalar C at the wall, the anti-bounceback condition can be used [70],

$$g_{\bar{i}}(\vec{x}_f, t + \Delta t) = -\tilde{g}_i(\vec{x}_f, t) + \frac{4+k}{10} C_w * \left(1 + \frac{4+k}{10}(\vec{\xi}_i \cdot \vec{u}_w)\right), \tag{3.8}$$

where C_w is the concentration at the wall. For the reader's interest, note that the right hand side of Eqs. 3.6, 3.7 and 3.8 contains a Δt, which means that the midway bounce-back is applied *during* the streaming step.

The expression for a free-slip boundary condition with the midway BB scheme is

$$h_{\bar{i}}(\vec{x}_f + \Delta T_i, t + \Delta t) = \tilde{h}_i(\vec{x}_f, t), \tag{3.9}$$

where ΔT_i is the distance to the destination node. This distance is one (in lattice Boltzmann units) when the direction i has a parallel velocity component with respect to the wall, and has a null value when i is normal to the boundary.

The specular reflection not only can act as a free-slip wall, but can also be used as a mirror boundary condition for axisymmetric problems (used in Sec. 5.4).

3.2.1   Boundary condition for surface reaction

We use a Neumann boundary condition to set a flux of reactant at a boundary. Briefly explained, the value of the concentration on the wall is determined, and the unknown distribution functions are calculated.

Firstly let us consider the final step and we will trace back all the necessary variables used in the process. We use the same anti-bounceback rule reported in 3.8 for a reactive wall

$$g_{\bar{i}}(\vec{x}_f, t + \Delta t) = -\tilde{g}_i(\vec{x}_f, t) + \frac{4+k}{10}C_{rw}, \tag{3.10}$$

where C_{rw} is the concentration on the physical reactive wall. The concentration on the wall is the key variable for the mid-way BB rule (3.10). Due to the mid-way BB rule, we know that the location of C_{rw} is the midpoint between the fluid node and the wall node. C_{rw} can be approximated with a first order finite difference scheme. Additionally, in a steady state and near the wall, we can approximate the fluxes in a control volume as

$$-D_p\frac{\mathrm{d}C}{\mathrm{d}\vec{x}_n} = N''(\vec{x}) = S_p = -D_p\frac{C_f - C_{rw}}{-0.5\mathrm{d}\vec{x}_n}, \tag{3.11}$$

S_p is the sink term mentioned in Sec. 2.82. C_f represents the concentration at the fluid node attached to a reactive wall, after subtracting the reacted part with the assumption that the wall acts as a perfectly mixed batch reactor and D_p is the platelet diffusion coefficient. The concentration C_f can be expressed as

$$C_f = C'_f(1 - k_{rt}), \tag{3.12}$$

where C_f' is the concentration at the fluid node before the subtraction of the sink term. The local flux $N''(\vec{x})$ in Eq. 3.11 is obtained numerically by means of

$$N''(\vec{x}) = k_{rt} C_f'(\vec{x}). \qquad (3.13)$$

The reaction flux is the local subtracted concentration from the fluid cell next to a reactive wall and at each time step.

Combining the Eqs. 3.11, 3.13 and 3.12 we obtain

$$C_{rw}(\vec{x}) = C_f - \frac{C_f(\vec{x}) k_{rt} * 0.5 \mathrm{d}y}{D_p}. \qquad (3.14)$$

This is a plausible approximation of C_{rw} which neglects the advective transport near the wall and the axial diffusion.

3.2.2 Second order bounce-back for curved walls

After understanding the bounce-back algorithm, one can notice that it has some limitations. The wall boundary needs to be a straight wall placed exactly between two nodes in order to be second order accurate in space. When any simple BB rule is used into a non-straight wall with an off-lattice node, it just degenerates its accuracy [52], as the simulation will interpret the boundary in a staircase-like shape (See Fig. 3.7). The fluid nodes attached to the boundary have at least one velocity direction towards the wall nodes, with corresponding particle distribution functions that should be bounced back. These fluid-solid links are seen in Fig. 3.7, where the green nodes are the ones which will hydrodynamically act as effective wall in the simulation. For this purpose, several second order bounce-back stencils for curved boundary geometries have been developed and contrasted [52]. Filippova and Hänel [23] first proposed a second order BB that intended to interpolate the resulting bounced velocity distribution function with a fictitious f^{eq^*} and the current value of the f at the boundary. This method was then improved by Mei, Luo and Shyy (often referred as MLS bounce-back [48]) who corrected the instability present when the wall node was very close to the physical location wall. We first show the notation used for the calculations in Fig. 3.8: $\vec{x}_b$ denotes a wall node attached to a fluid node $\vec{x}_f$, Δ is the normalised distance between the physical wall node (yellow nodes) and the boundary fluid node (red node), relative to the distance of the corresponding fluid-solid link (δx), and $\vec{x}_w$ denotes the physical wall nodes. These $\vec{x}_w$ can be off-lattice locations and they are computationally stored in a Lagrangian array. This array is afterwards used to calculate the distance between

Fig. 3.7 Mid-way bounce-back rule applied on an arbitrary curved wall.

Fig. 3.8 Mei et al. bounce-back rule applied on an arbitrary curved wall.

the fluid node and the physical wall Δ,

$$\Delta = \frac{|\vec{x}_f - \vec{x}_w|}{|\vec{x}_f - \vec{x}_b|}. \tag{3.15}$$

The mathematical expression for the MLS-BB takes the following form

$$\tilde{f}_{\bar{i}}(\vec{x}_b,t) = (1-\chi)\tilde{f}_i(\vec{x}_f,t) + \chi f_{\bar{i}}^{eq^*}(\vec{x}_b,t) - 2\omega_i \rho \frac{3}{c^2}(\vec{\xi}_{\bar{i}} \cdot \vec{u}_w), \tag{3.16}$$

where the fictitious equilibrium distribution function f^{eq^*} is

$$f_{\bar{i}}^{eq^*}(\vec{x}_b,t) = \omega_i \rho(\vec{x}_f,t)\left[1 + \frac{3}{c^2}\vec{\xi}_{\bar{i}} \cdot \vec{u}_{bf} + \frac{9}{2c^4}(\vec{\xi}_{\bar{i}} \cdot \vec{u}_f)^2 - \frac{3}{2c^2}\vec{u}_f \cdot \vec{u}_f\right]. \tag{3.17}$$

Here $\vec{u}_f \equiv \vec{u}(\vec{x}_f,t)$ is the velocity at the fluid boundary node $\vec{x}_f$, and finally, $\vec{u}_{bf}$ and χ are proposed to be

$$\begin{cases} \vec{u}_{bf} = \frac{(\delta-1)\vec{u}_f}{\Delta} + \frac{\vec{u}_w}{\Delta} & \text{and} \quad \chi = \frac{2\Delta-1}{\tau}, & \text{for} \quad \Delta \geq \frac{1}{2} \\[3mm] \vec{u}_{bf} = \vec{u}_f & \text{and} \quad \chi = \frac{2\Delta-1}{\tau-2}, & \text{for} \quad \Delta < \frac{1}{2} \end{cases} . \tag{3.18}$$

There are several other approaches that deal with off-lattice boundaries with second order accuracy ([10, 78]), only the MLS-BB method has been explained here as it is the one used in this thesis, and besides, it is found to be the one that minimises the errors in laminar regimes [52].

3.3   Simple inlet/outlet boundary conditions

So far we have reviewed boundary conditions focused on the wall treatment*. The presented methods directly produce new values for the unknown distribution functions from the outgoing ones. The methods from this section will calculate the unknown f_is more elaborately. This fact responds to the necessity of fixing a desired macroscopic value/gradient at the open boundary. We will better discuss this issue in detail by analysing these inlet/outlet BCs.

---

*It is important to stress that the bounce-back rules analysed at Eqs. 3.6, 3.8 can be used also as an inlet BC, as soon as you set a velocity value according to the hydrodynamic flux at the wall.

3.3.1   Equilibrium boundary condition

The equilibrium boundary condition (EBC) was first proposed by [75] and consists in replacing the missing f_is with their corresponding equilibrium values. Having in mind that this method is only first order accurate, added to the fact that the provided values do not consider shear forces (see Sec. 2.1.3), we consequently avoid the use of this BC at inlets, as it would provide an incorrect solution whenever we would try to fix a shear flow (Poiseuille flow, constant shear, etc). Hence, the outlet for this BC is formulated as

$$f_i = f_i^{eq}(\rho_0, \vec{u}(\vec{x}_b - \Delta x)) \tag{3.19}$$

where Δx represents the normal distance from the fluid node to the boundary location $(\vec{x}_b)$.

3.3.2   Zou/He boundary conditions

The idea of the Zou/He BC (ZH-BC) [79] is similar to the BB rule. However, only the non-equilibrium part of the outgoing distributions is bounced back, which is formally expressed as

$$f_i - f_i^{eq} = f_{\bar{i}} - f_{\bar{i}}^{eq}. \tag{3.20}$$

To facilitate the understanding of this procedure, we will focus on an example of unknown populations to be determined at the inlet and outlet boundaries in Fig. 3.9.

     The missing populations for our inlet/outlet are highlighted in blue at Fig. 3.9. The channel has no-slip horizontal walls at the top and the bottom, with a developed incoming flow on the left boundary as the inlet, and the corresponding outlet on the right. Typically, this problem is dealt with a Dirichlet condition where the velocity is fixed at the inlet and the pressure is fixed at the outlet. We rely on the macroscopic LBM averages (Eq. 2.47, Eq. 2.48) and the non-equilibrium assumptions from the ZH-BC approach to conform a determined system of linear algebraic equations. We start with the inlet BC, by identifying the missing populations, f_1, f_5, f_8.

     We remark that we have four unknown variables f_1, f_5, f_8, ρ as we know the two velocity components. We set a trivial horizontal $\vec{u} = (u_x, 0)$ and write the following system of equations,

$$f_1 - f_1^{eq} = f_3 - f_3^{eq} \quad \rightarrow \quad f_1 = f_3 + (f_1^{eq} - f_3^{eq}) = f_3 + \frac{2}{3}\rho u_x \tag{3.21}$$

$$u_x = \frac{\sum_i f_i \xi_{i,x}}{\rho} \quad \text{and} \quad u_y = \frac{\sum_i f_i \xi_{i,y}}{\rho} \tag{3.22}$$
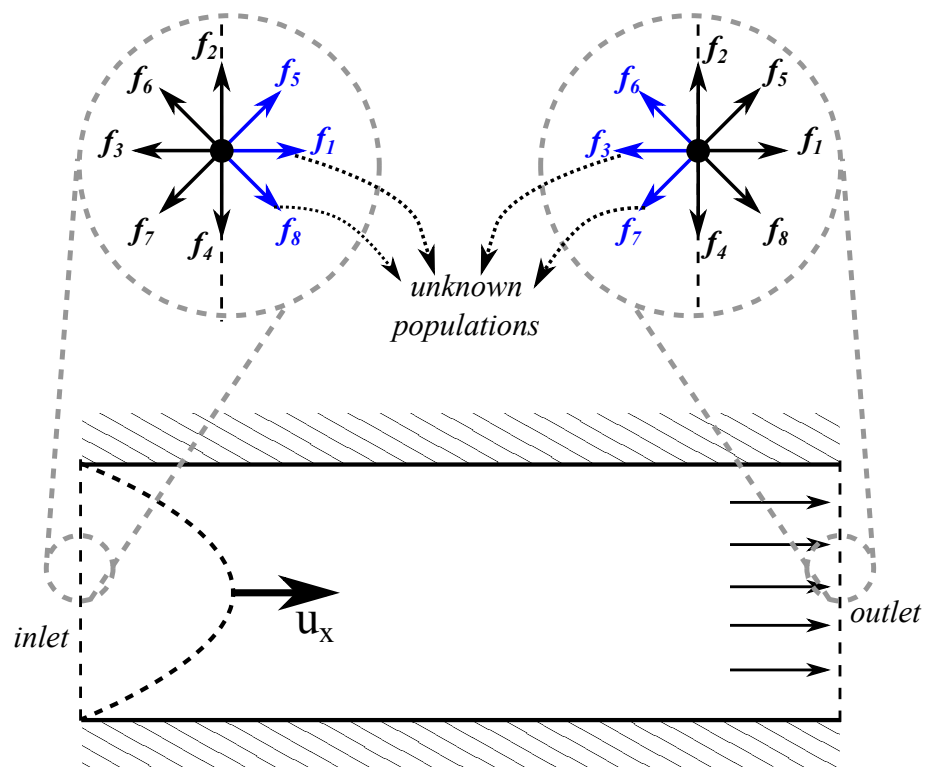
Fig. 3.9 Unknown distribution functions for a vertical boundary as
inlet/outlet with the D2Q9 discrete velocity set.

$$\rho = \sum_i f_i. \tag{3.23}$$

We can obtain the value of ρ by combining Eq. 3.23 and Eq. 3.22, where we can get rid of the three unknown

$$f_1 + f_5 + f_8 = \rho - (f_0 + f_2 + f_3 + f_4 + f_6 + f_7) = \rho u_x + f_3 + f_6 + f_7. \tag{3.24}$$

The resulting density is

$$\rho = \frac{f_0 + f_2 + f_4 + 2(f_3 + f_6 + f_7)}{1 - u_x}. \tag{3.25}$$

Hence we can combine Eq. 3.21 and Eqs. 3.22 to determine the missing fs

$$f_1 = f_3 + \frac{2}{3}\rho u_x \tag{3.26}$$

$$f_5 = f_7 - \frac{1}{2}(f_2 - f_4) + \frac{1}{6}\rho u_x \tag{3.27}$$

$$f_8 = f_6 + \frac{1}{2}(f_2 - f_4) + \frac{1}{6}\rho u_x. \tag{3.28}$$

At the outlet we set the pressure boundary condition, and additionally, set the vertical velocity to zero ($u_y = 0$) to have a determined system of equations. Hence,

$$u_x = \frac{f_0 + f_2 + f_4 + 2(f_1 + f_5 + f_8)}{\rho} - 1. \tag{3.29}$$

and the unknown populations at the outlet are obtained combining Eqs. 3.21 and 3.22

$$f_3 = f_3 - \frac{2}{3}\rho u_x \tag{3.30}$$

$$f_6 = f_8 + \frac{1}{2}(f_2 - f_4) - \frac{1}{6}\rho u_x \tag{3.31}$$

$$f_7 = f_5 - \frac{1}{2}(f_2 - f_4) - \frac{1}{6}\rho u_x. \tag{3.32}$$

3.4   Characteristic boundary condition

In the aforementioned inlet/outlet BCs, it is common to find that density perturbations due to compressibility effects inherent to the method propagate in the system and are reflected on the boundaries back to the domain. Any simple Dirichlet inlet velocity or outlet pressure BC is not able to absorb these pressure waves, as they have one of the macroscopic variables tied to a desired state. This issue can be problematic as these waves can interact with the surrounding obstacles and other boundaries of the domain. Therefore, a perfect flow BC (for inlet/outlet) should avoid the reflection of these pressure waves in order to avoid a possible degeneration of the accuracy of the model. However, we clearly stated that there is no perfect non-reflecting boundary condition (NRBC) due to the lack of information on the boundaries of the domain (Fig. 3.1). Regarding this issue, we introduce a popular BC scheme that can reduce significantly these undesired density and velocity reflections.

The characteristic boundary condition (CBC) computes the macroscopic properties of the fluid ($\vec{U}(\rho, u_x, u_y)$) at each timestep by solving a hyperbolic system of equations at the boundaries, and in addition assuming that the incoming pressure waves from the outside of the domain are set to zero. These assumptions lead to a set of inviscid constitutive equations resembling the Euler equations. Since we use an isothermal LB model, there is no point in solving the energy equation in this system,

$$\frac{\partial \vec{U}}{\partial t} + A \frac{\partial \vec{U}}{\partial x} + B \frac{\partial \vec{U}}{\partial y} = 0, \tag{3.33}$$

where $\vec{U}$ is the vector of the macroscopic variables of the system and the coefficient matrices A and B are given by

$$A = \begin{pmatrix} u_x & \rho & 0 \\ \frac{c_s^2}{\rho} & u_x & 0 \\ 0 & 0 & u_x \end{pmatrix}, \qquad B = \begin{pmatrix} u_y & 0 & \rho \\ 0 & u_y & 0 \\ \frac{c_s^2}{\rho} & 0 & u_y \end{pmatrix}, \qquad \vec{U} = \begin{pmatrix} \rho \\ u_x \\ u_y \end{pmatrix}. \tag{3.34}$$

Here u_x, u_y are the velocity components in the x and y direction, respectively, and ρ is the density. Matrices A and B can be diagonalized,

$$SAS^{-1} = \Lambda, \qquad TBT^{-1} = M, \tag{3.35}$$

where Λ and M are diagonal matrices with local eigenvalues

$$\Lambda = diag(u_x - c_s, u_x, u_x + c_s), \qquad M = diag(u_y - c_s, u_y, u_y + c_s), \tag{3.36}$$

and c_s is the speed of sound. Matrices S and T are given by [33]

$$S = \begin{pmatrix} c_s^2 & -c_s\rho & 0 \\ 0 & 0 & 1 \\ c_s^2 & c_s\rho & 0 \end{pmatrix}, \qquad T = \begin{pmatrix} c_s^2 & 0 & -c_s\rho \\ 0 & 1 & 0 \\ c_s^2 & 0 & c_s\rho \end{pmatrix}. \qquad (3.37)$$

Incoming and outgoing waves are identified by the sign of each eigenvalue of Λ and M, taking into account the relative position of the boundary. Given a vertical boundary parallel to the y-axis, wherever the Λ eigenvalues are positive, the corresponding waves move along the positive x-axis direction, and oppositely, the wave propagates along the negative x-axis direction if the eigenvalue is negative. So, for instance, outgoing waves will correspond to negative eigenvalues at the inlet and positive eigenvalues at the outlet. Thompson [67] proposed to annihilate the incoming waves due to the lack of information from the outside of the domain and in order to minimise the reflections,

$$\vec{L}_{x,i} = \begin{cases} \lambda_i \vec{\ell}_i^\intercal \frac{\partial \vec{U}}{\partial x} & \text{for outgoing waves} \\ 0 & \text{for incoming waves} \end{cases} \qquad \vec{L}_x = \begin{pmatrix} L_{x,1} \\ L_{x,2} \\ L_{x,3} \end{pmatrix}, \qquad (3.38)$$

where λ_i is the ith eigenvalue and $\vec{\ell}_i^\intercal$ is the ith row of S. The wave amplitudes $\vec{L}_x$ are expressed in characteristic coordinates by means of

$$A\frac{\partial \vec{U}}{\partial x} = S^{-1}\Lambda S\frac{\partial \vec{U}}{\partial x} := S^{-1}\vec{L}_x \cdot \qquad (3.39)$$

Following the work by [35], the Local One Dimensional Inviscid (LODI) equations have been used to compute $\vec{U}$ at the boundaries. The LODI approach assumes that there are no contributions from the y-axis derivatives,

$$\frac{\partial \vec{U}}{\partial t} + S^{-1}\vec{L}_x = 0. \qquad (3.40)$$

In addition to the LODI approach, we also consider Thompson's BC. The y-derivatives of the macroscopic fluid properties are also included in the Euler hyperbolic system of equations, resulting in

$$\frac{\partial \vec{U}}{\partial t} + B\frac{\partial \vec{U}}{\partial y} + S^{-1}\vec{L}_x = 0. \qquad (3.41)$$

The x-derivatives are computed for both CBC using a one-sided second order stencil. The y-direction derivatives, instead, are computed by means of a centred second order approximation.

The last step consists in computing the equilibrium distribution functions at the boundary nodes using Eq. 2.46 and the values of $\vec{U}$ computed with the CBC procedure. Furthermore, the modified Equilibrium Boundary Condition (mEBC) approach is adopted from [33] which is expected to improve the solution at the boundary. The mEBC linearly extrapolates the non-equilibrium information ($f_i^{neq} = f_i - f_i^{eq}$) from the two lattice nodes nearest to the boundary,

$$f_i(\vec{x}_b) = f_i^{eq}(\vec{x}_b) + 2f_i^{neq}(\vec{x}_{b+1}) - f_i^{neq}(\vec{x}_{b+2}), \tag{3.42}$$

where $\vec{x}_b$ are the boundary nodes, and $(\vec{x}_{b+1})$, $(\vec{x}_{b+2})$ correspond to the nearest two fluid nodes in the perpendicular direction to the boundary.

Chapter 4

Reflective vs non-reflective boundary conditions

Effective non-reflective boundary conditions (BC) for LBM have been proposed in several occasions [33, 35, 36, 39, 54, 61, 66]. However, beyond the initial BC tests, there is not that much investigation on the impact of using a reflecting or a non-reflecting boundary condition, at exception of [36], where the authors assess the performance of different sets of popular BC schemes on the fluctuations of the drag experienced by a square obstacle in a confined channel. In order to add scientific knowledge about the physical impact of reflected waves that arise in the simulations, we provide an extended parametric study that will mainly focus on the physical variations that can occur when dealing with one BC or another. The parametric study will be done on a well-known case: a developed flow past a square obstacle in an open channel.

4.1   Physical Model

We first show in Fig. 4.1 the physical model used for simulations. The square cylinder is located at the centerline of the y-axis and at one fifth of the total channel length L_x. We consider two different channel widths with ratios $AR = \frac{N}{L_y} = \frac{1}{8}, \frac{1}{16}$ respectively, where L_y is the total height of the channel and N the edge length of the square obstacle, respectively. This dimensionless control variable has been selected instead of the usual blockage ratio ([55, 62]) to keep the size of the channel width, regardless of the orientation of the square. Additionally, we set the square cylinder at three different angles of incidence $\theta = 0, 15.3, 45$ degrees, which correspond with a subset of the angles used by [76]. Consequently, the projected length of the obstacle h increases as the angle goes from $0°$ to $45°$. The range of Reynolds numbers is $50 \leq \text{Re} \leq 150$,
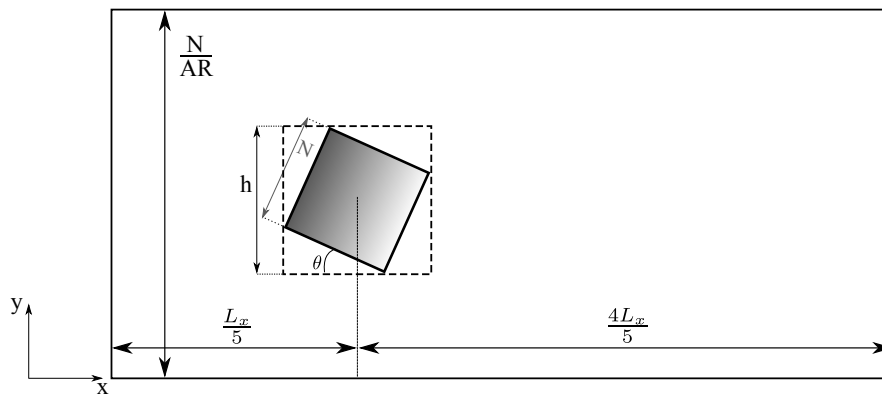
Fig. 4.1 Domain dimensions.
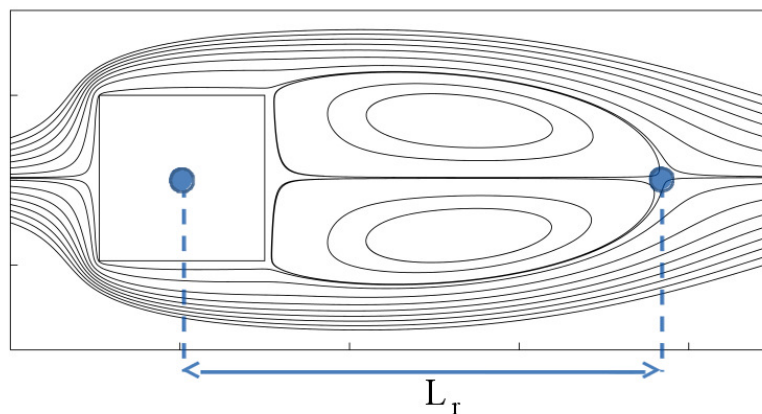
Fig. 4.2 Example on how the recirculation length is determined.

whereas the critical Re for the periodic vortex shedding regime in the nearly freestream case, is $38 \lesssim \text{Re} \lesssim 48$ ([76]). The drag and lift coefficients and Strouhal number are respectively determined with Eqs. 2.59 and 2.60. No-slip walls with simple bounce back (BB) are considered at the top and the bottom boundaries of the channel, and no-slip walls with second order BB (Sec. 3.2.2) are implemented at the obstacle boundaries. Once the simulations are finished, we calculate the time-averaged values of the velocity in a single period of vortex shedding to lay out the main features of the unsteady flow regime. The streamlines of these time-averaged velocities are used to determine the recirculation length ratio (L_r/h) (see Fig. 4.2 as an example). The used mesh is uniform and has 2080×320 and 2080×640 nodes for $AR = \frac{1}{8}, \frac{1}{16}$ respectively.

4.2   Parametric approach

The following parametric study consists in preparing a set of simulations by changing
the following parameters:

- Reynolds number: 50 to 150

- Aspect ratio of the channel: $\dfrac{1}{8}, \dfrac{1}{16}$

- Angle of incidence: 0, 15.3 and 45 degrees

- Boundary Condition configurations

    - Inlet with Zou/He. Outlet with Equilibrium: **ZH/Eq**

    - Inlet with Zou/He. Outlet with Zou/He: **ZH/ZH**

    - Inlet with Zou/He. Outlet with CBC: **ZH/CBC**

    - Inlet with CBC. Outlet with CBC: **CBC/CBC**

We choose the LODI approach [35] for the CBC in this parametric study. Velocity
is fixed at the inlet (Poiseuille flow with $u_{max} = 0.1$, avoiding a Mach number bigger
than 0.3) and the reference density is fixed at the outflow ($\rho_0 = 1$), both in lattice
units. The Reynolds number is varied by changing the value of viscosity. The chosen
values of the velocity and viscosity are in fact the same as in [36], which facilitates the
comparison. In addition, the simulation is initialised by setting the reference Poiseuille
flow

$$\vec{u}_0(y) = u_{max} \left(1 - \left(\frac{y - \dfrac{N}{2AR}}{\dfrac{N}{2AR}} \right)^2 \right), \tag{4.1}$$

along with the reference density in the domain. $N/2AR$ represents here the half of the
channel width, and y is the y-axis spatial coordinate. The probability densities $f_i(\vec{x}, t_0)$s
are initially set to their corresponding $f_i^{eq}(\rho, \vec{u})$ values, as explained at Sec. 2.2.

4.2.1   Validation

Figure 4.3 shows the mean drag coefficient C_D, the mean peak-to-peak lift coefficient
ΔC_L and the Strouhal number St versus Re, for the parameters $AR = \frac{1}{8}$ ($N = 40$) and
$\theta = 0°$. ZH-BC was applied at the inlet and Eq-BC at the outlet. Results of [36] for
the same value of AR are also included, as well as results from Ref. [11], which were
obtained at a higher $AR = 6.25\%$ and thus consistently give smaller values for the
drag coefficient. Good agreement is shown between our results and the bibliography.
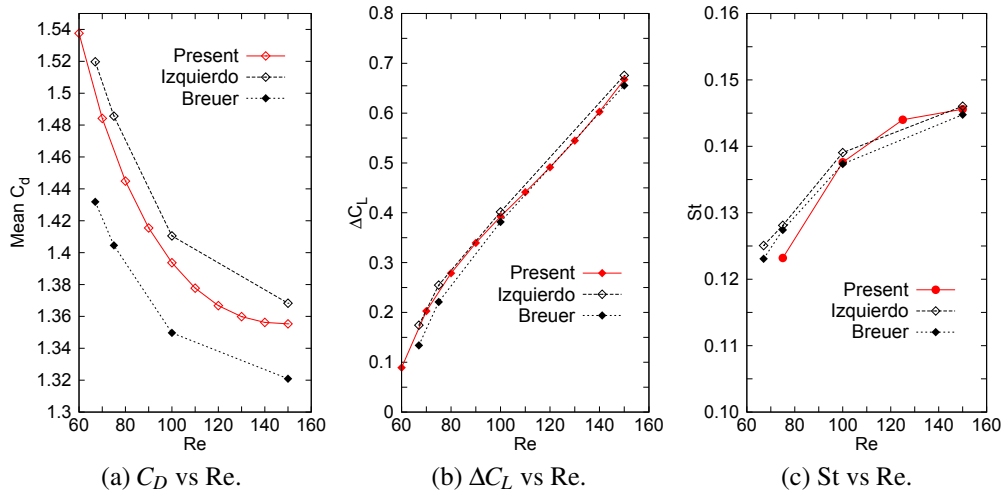
(a) C_D vs Re.   (b) ΔC_L vs Re.   (c) St vs Re.

Fig. 4.3 Plot of **a)** C_D vs Re, **b)** ΔC_L vs Re, **c)** St vs Re, along with benchmark results [11, 36].

Specifically, *St* shows a small deviation which does not exceed 4% at Re $= 75$ whereas both C_D and ΔC_L fall close to the results reported in [36].

4.2.2   Mesh independence test

A grid independence test is shown in Fig. 4.4, where the drag and lift coefficients are evaluated combining different meshes ($N = 10, 20, 30, 40$) and different reference velocities ($u_{max} = 0.1, 0.05$, which correspond to Ma$= 0.173, 0.087$, respectively). Figure 4.4 shows that the relative errors of C_D, ΔC_L obtained after diffusive scaling of the system, from $N = 20$, $u_{max} = 0.1$ to $N = 40$, $u_{max} = 0.05$, are within 1.5%. Comparing the results $N = 40$ at $u_{max} = 0.1$ and 0.05, the relative difference is about 1%, therefore for the tests presented in the following sections we have used the configuration $N = 40$ at $u_{max} = 0.1$, which saves half of the computation time with higher robustness while providing the same relevant information.

4.2.3   Time stability

Figure 4.5 demonstrates that the number of time steps used guarantees a fully converged solution in all the cases. Additionally, we can observe in Fig. 4.5c a faster stabilisation of the drag coefficient with the ZH/CBC configuration.
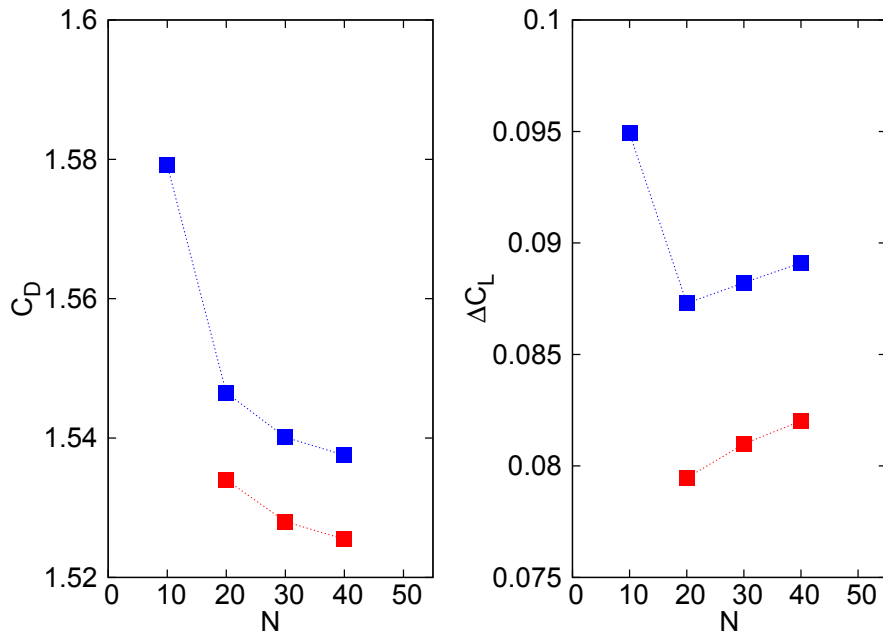
Fig. 4.4 Mesh independence test for C_D (left) and ΔC_L (right) at Re= 60, using $N = 10, 20, 30, 40$, $u_{max} = 0.1$ (in blue) and $u_{max} = 0.05$ (in red). The ZH/ZH configuration is considered for the test.

4.2.4 CBC inlet velocity correction

We saw in Sec. 3.4 that CBC-LODI does not fix neither the density nor the velocity as it has a dynamic response which depends on the information of the neighbour nodes and the previous (in time) values of the magnitudes. Therefore, it is a priori not possible to fix the inlet velocity with a CBC approach. Nevertheless, we can neglect this problem by considering two facts. Firstly, it is crucial to remark that CBC-LODI (Eq. 3.40), unlike Thompson BC, only considers the spatial derivatives on the perpendicular direction to the boundary and therefore the flow is unaffected by the information carried by the y-axis nodes in our inlet boundary configuration, where there obviously exists a velocity gradient due to the initially imposed developed Poiseuille flow. Secondly, from the inlet up to the obstacle, the macroscopic variables remain mostly unaltered, as in this part of the flow there is no influence from the obstacle. As a result, throughout our simulations, the flow near the inlet does only experiment significant axial fluctuations at the beginning of the simulation, when the initial pressure wave caused by the square obstacle reaches the inlet boundary (see Fig. 4.6). Under the aforementioned assumptions, we analysed the CBC-LODI behaviour at the inlet by running a set simulations. The tested parameters are: $AR = \frac{1}{8}$, $\theta = (0°, 15.3°)$, CBC-LODI at inlet/outlet and Re $= (50, 100, 150)$. Analysing the simulation outputs, we found that the values of the velocity and the density at the
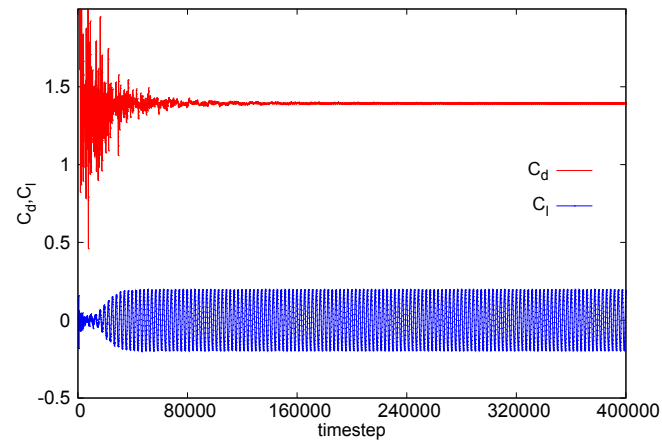
(a) ZH/Eq configuration.
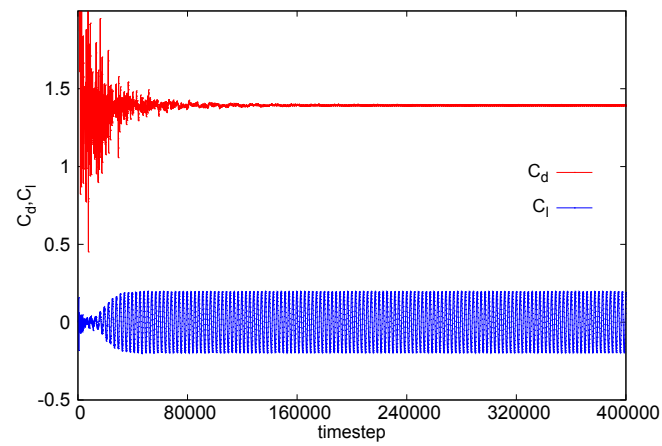
(b) ZH/ZH configuration.
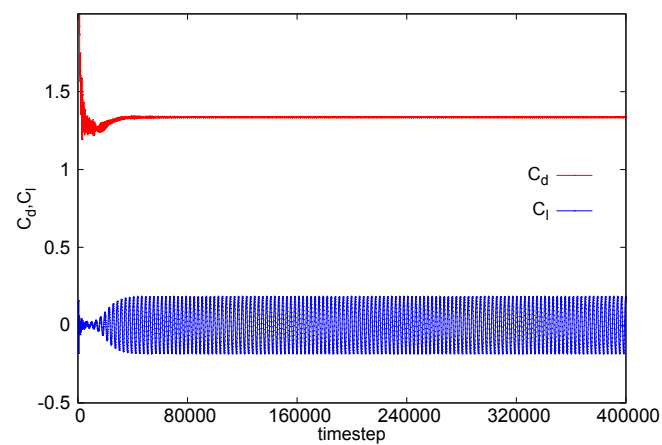
(c) ZH/CBC configuration.

Fig. 4.5 Time evolution of the drag and lift coefficients for a test case, with Re= 100, $AR = \frac{1}{8}$ and $\theta = 0°$.
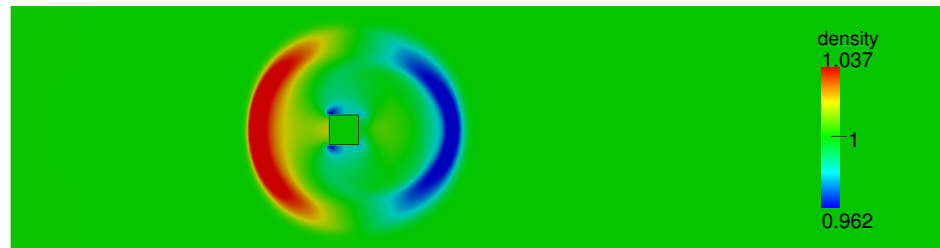
(a) Test example: pressure wave instants after initialisation.
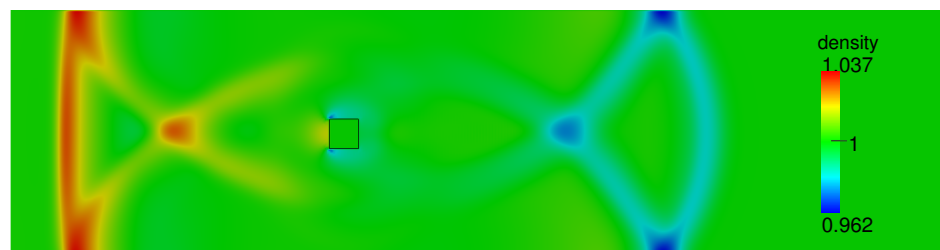
(b) Test example: pressure wave approaching the inlet.
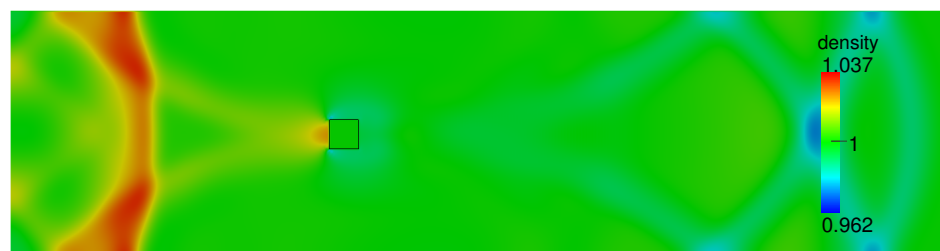
(c) Test example: reflected pressure wave coming from the inlet.

Fig. 4.6 Example of a initial pressure wave after initialisation (zoomed). Zou/He inlet test case with Re $= 50$, $AR = \frac{1}{8}$ and $\theta = 0°$

inlet fluctuated to mitigate the incoming pressure waves, acting as an open boundary condition. After absorbing the first pressure wave produced by the initial condition around the obstacle, we observed a general reduction of the velocity around 1-3.5% at the centerline. After waiting until the simulation was periodic, the inlet velocity remained parabolic, with fluctuations not bigger than 0.05% at the centerline, and with the aforementioned velocity reduction.

To compensate for this undesired velocity offset, we first ran every possible CBC-LODI/CBC-LODI simulation until the first big wave passed through and the velocity profile at the inlet was quasi-constant (showing only small fluctuations). Then, we individually calculated this deviation with respect to the theoretical velocity $u_0(y)$ according to the parabolic flow. Subsequently, we introduced a correction on the real initial velocity condition to counteract the effects of the initial wave as seen in Eq. 4.2. After applying this procedure, we greatly neutralised the velocity offset problems originated from the first pressure wave, and we obtained the velocity inlet profiles in all cases with a maximum deviation of 0.08% with respect to the initial Poiseuille flow at the centerline.

$$u_0'(y) = u_0(y) + \Delta u_{corr}(y) \tag{4.2}$$

where $u_0'(y)$ is the corrected initial velocity profile and $\Delta u_{corr}(y)$ is the difference between the analytic velocity and the velocity value obtained at the inlet after applying the CBC at the inlet without any correction. By judging Fig. 4.7, we assume that the magnitude of these perturbations is greatly diminished up to negligible discrepancies with the analytic solution when compared with the uncorrected inlet profile. Analysing the near wall values we can observe that the errors grow rapidly, but the impact of those on the parabolic velocity is still small and we will consider them negligible as there is still room for a complete development of the flow before the fluid takes contact with the obstacle. Additionally, it is worth to mention that the errors are minimal at the centerline, which is in fact the most important part of our study as it is where the obstacle lies.

Furthermore, we will observe later in Sec. 4.4.1 that the fluctuations of the drag and lift coefficients are two or three orders of magnitude higher, which guarantees that the results are not significantly perturbed by the implementation of the CBC at the inlet.

4.3   Analysis of the flow

In this section we will briefly describe the typical flow patterns of this problem, which will serve not only as references for validation by comparing them with other known
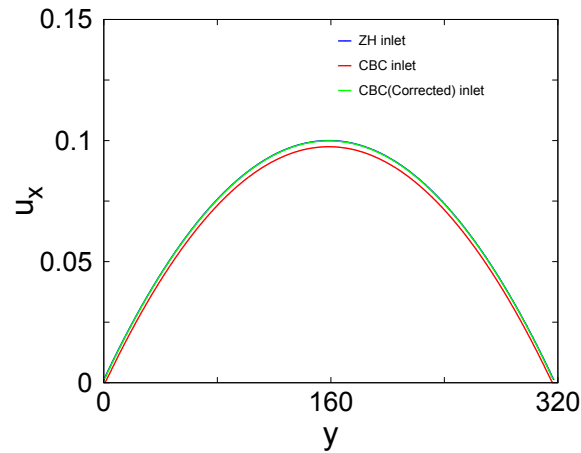
(a) Plots of analytic parabolic velocity, inlet CBC and
corrected inlet CBC profiles.
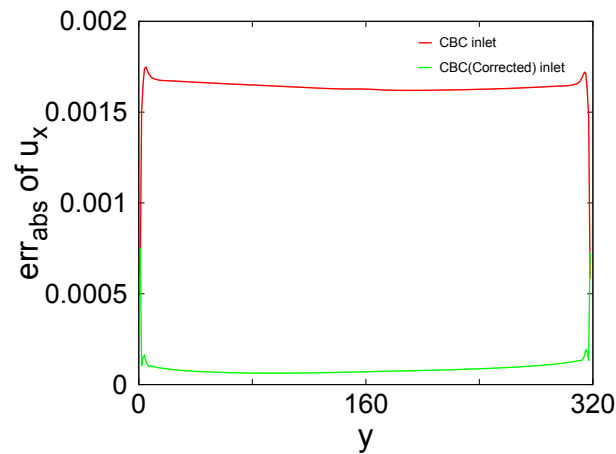
(b) Plots of velocity, inlet CBC and corrected inlet CBC
profiles. Absolute errors.
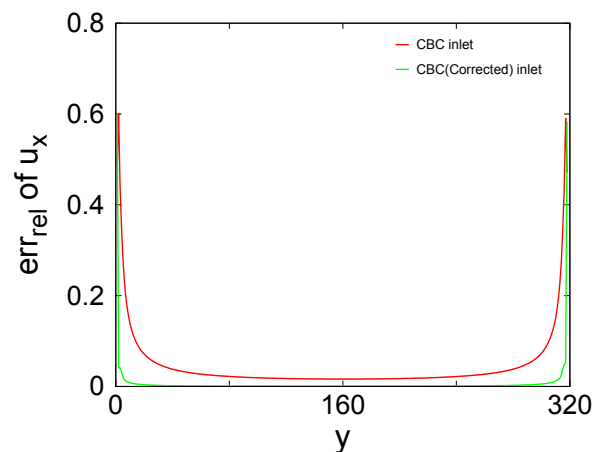
(c) Plots of velocity, inlet CBC and corrected inlet CBC
profiles. Relative errors.

Fig. 4.7 Velocity obtained at the inlet applying CBC, with respect to the Poiseuille
velocity profile and its errors before and after the correction has been applied. Re =
100, $AR = \frac{1}{8}$ and $\theta = 0°$

(a) Re = 60.   (b) Re = 90.   (c) Re = 150.
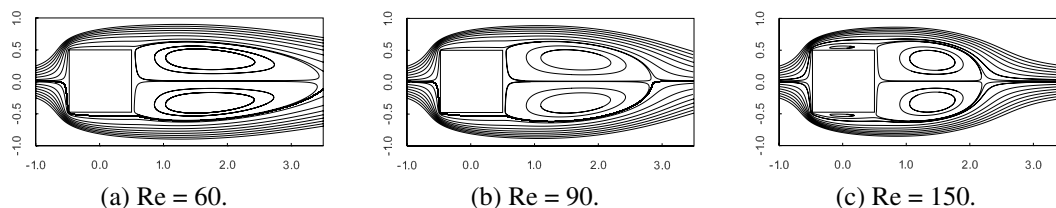
Fig. 4.8 Zoomed part of the simulation domain where the wake of the obstacle is formed. Both *x* and *y* axes are normalised with the projected length of the obstacle *h*. Time-averaged streamlines for $\theta = 0°$ and $AR = \frac{1}{8}$ and different Reynolds numbers. **a)** Re = 60, **b)** Re = 90, **c)** Re = 150

(a) $\theta = 0°$.   (b) $\theta = 15°$.   (c) $\theta = 45°$.
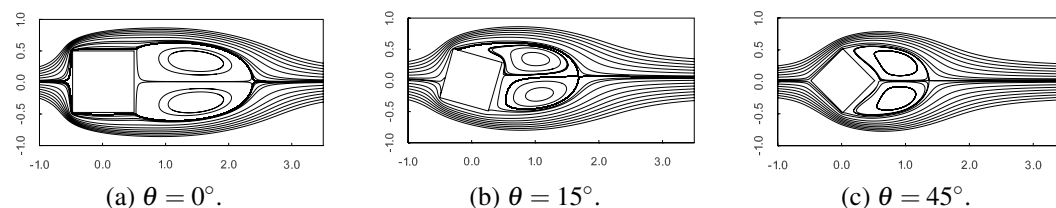
Fig. 4.9 Zoomed part of the simulation where the wake of the obstacle is formed. Both *x* and *y* axes are normalised with the projected length of the obstacle *h*. Time-averaged streamlines for Re = 120, $AR = \frac{1}{8}$ and different angles of incidence, **a)** $\theta = 0°$, **b)** $\theta = 15°$ and **c)** $\theta = 45°$.

benchmarks ([76]), but also will give us a good perspective of how the wake of the flow responds to the considered parameters.

Figure 4.8 shows the time-averaged velocity streamlines for $\theta = 0°$, at different Re. The streamlines are used to determine L_r/h (see Sec. 4.1 for details of L_r/h and Sec 2.6 for how it is obtained).

Figures 4.8a and 4.8b constitute a clear example of main separation pattern. In addition, in Fig. 4.8c a new pair of secondary vortexes appear on the upper and lower edges of the square obstacle. This dual secondary vortex pattern is typical for $\theta = 0°$ and $Re > 130$ conditions. Figure 4.9c shows the wakes behind the obstacle for the different angles of incidence θ. We observe that as θ increases, the wake is visibly reduced. Moreover, Fig. 4.9b shows that the separation point on the upper edge shifts to the left corner. All these flow patterns are also reported in [76] for the freestream case.

4.4 The effect of the boundary conditions

In the following study we focus on the comparative analysis of the different BCs considered in Sec. 4.2 by studying different outputs: C_D and ΔC_L (difference between

maximum and minimum lift coefficients), instantaneous C_d and C_l, and recirculation length ratio L_r/h.

4.4.1 Mean drag and lift coefficients

Figure 4.10 shows the plots of the time-averaged C_D and ΔC_L within a vortex shedding cycle *vs*. Re, as compared with results from [11, 36]. Since no significant differences were observed between the two reflective BCs (ZH/Eq vs ZH/ZH), only the values for ZH/ZH, ZH/CBC and CBC/CBC configurations are reported. Fig. 4.10 shows that the deviations of C_D and ΔC_L for configurations of the type ZH/ZH (red-squared dots) and ZH/CBC (blue-circled dots) are clearly negligible. The maximum deviation obtained for C_D is 0.365% and for ΔC_L is 3.71%, and both occur for $\theta = 45°$ and $AR = 1/8$. In contrast, when CBC are implemented at the inlet (green-lines), the C_D is significantly smaller. We observe that the magnitude of this mismatch depends directly on AR, which is more pronounced when AR is increased. In parallel, ΔC_L is also slightly diminished when a non-reflective BC is implemented at the inlet at exception of $\theta = 0°$.

From these observations, we can state that there is no significant effect on the mean time-averaged forces by changing reflective (ZH) to non-reflective (CBC) at the outlet. However by applying non-reflective BC at the inlet, the suppression of the incoming pressure waves at the inlet eventually modifies the forces downstream, and as a result, lesser values of both C_D and ΔC_L are obtained (green lines from Fig. 4.10). The proximity of the channel walls, controlled by the parameter AR, enhances the effect of the reflective contributions —reflections from a distant boundary will reach the obstacle more attenuated. Therefore, the differences of the drag and lift coefficients between the ZH/CBC and the CBC/CBC combinations increase, as the channel becomes narrower. For instance, for $AR = 1/8$, the net drag reduction after applying CBC at the inlet is relatively bigger than the drag reduction in a channel of $AR = 1/16$. The increase of the angle of incidence from $\theta = 0$ to $45°$, which exemplifies changes in the shape of the object, even magnifies the deviations (however increasing θ for the same channel width, effectively brings the obstacle slightly closer to the channel walls as the projected length of the square cylinder is bigger).

4.4.2 Phase diagrams of drag and lift coefficients

Phase diagrams of the instantaneous C_l vs C_d for each incidence angle and for each AR are presented in Fig. 4.11. They are useful to assess how the fluctuations of the lift and drag forces within a vortex cycle are modified as a function of the chosen BC set.

UNIVERSITAT ROVIRA I VIRGILI
REVIEW OF BOUNDARY CONDITIONS AND INVESTIGATION TOWARDS THE DEVELOPMENT OF A GROWTH MODEL: A LATTICE
BOLTZMANN METHOD APPROACH
Albert Puig Arànega

66   Reflective vs non-reflective boundary conditions

(a) Plot of C_D vs Re for $\theta = 0°$

(b) Plot of ΔC_L vs Re for $\theta = 0°$

(c) Plot of C_D vs Re for $\theta = 15.3°$

(d) Plot of ΔC_L vs Re for $\theta = 15.3°$

(e) Plot of C_D vs Re for $\theta = 45°$

(f) Plot of ΔC_L vs Re for $\theta = 45°$
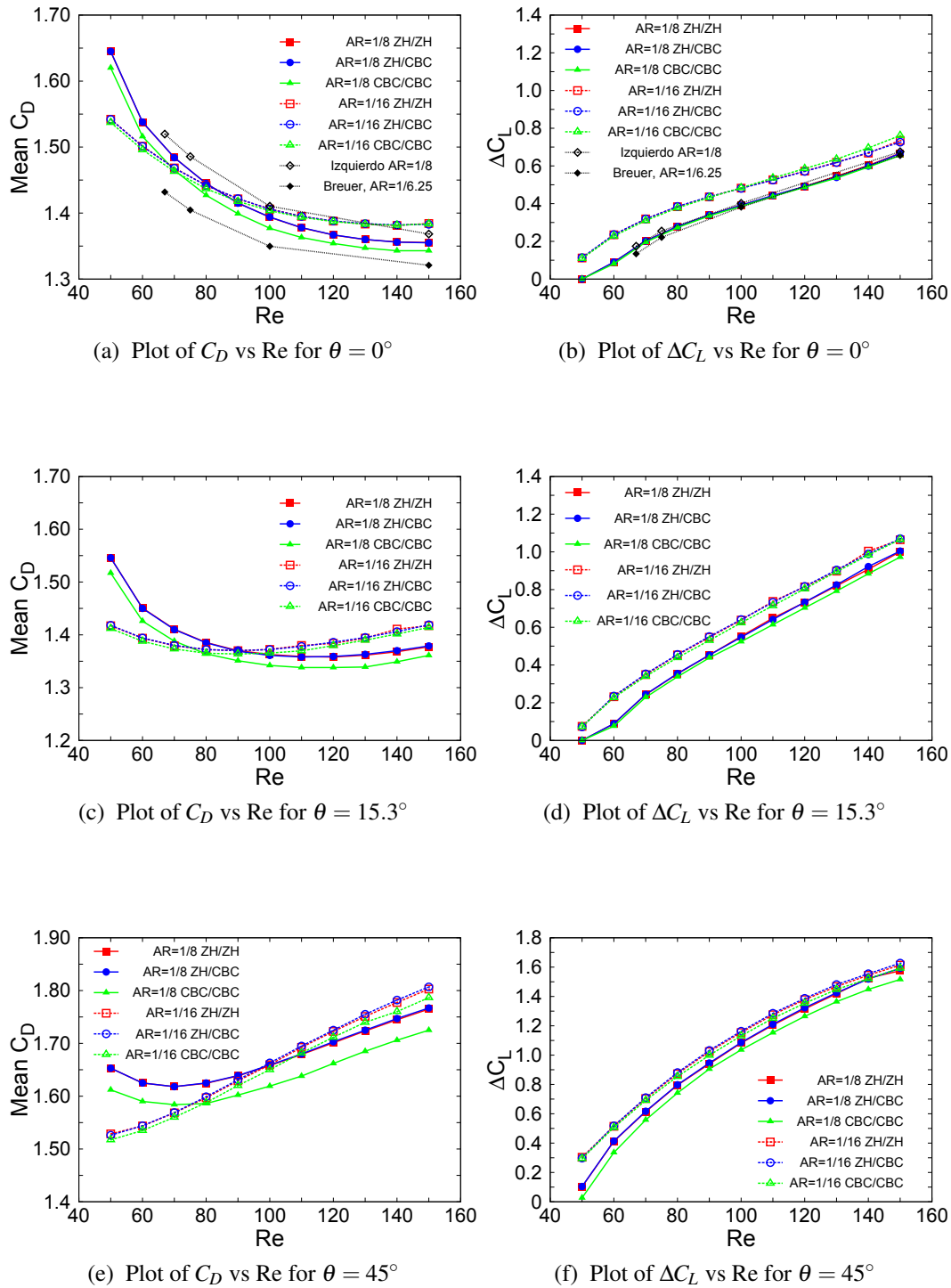
Fig. 4.10 Plots of C_D vs Re and ΔC_L vs Re for $\theta = 0, 15.3$ and $45°$. Coloured lines: present data; black lines: reference values ([11, 36]). Filled and empty symbols represent $AR = 1/8$ and $AR = 1/16$, respectively. We use red squares for the ZH/ZH configuration, blue circles for ZH/CBC and green triangles for CBC/CBC.

In each figure, ZH/ZH, ZH/CBC and CBC/CBC configurations are plotted for $70 \leq$ Re ≤ 150. The patterns of the ZH/Eq (black-dashed line) configuration are added in Figs. 4.11a-4.11b only, as this is the only case where some noticeable differences are worth to report. Figure 4.11 shows that the oscillations of C_d and C_l increase in amplitude as the Reynolds number increases (the arrows indicate the direction of the increase of Re). The shape of the phase diagram depends on the angle of incidence; for symmetric geometries (0 and 45°), the pattern is symmetric with respect to the horizontal axis at $C_l = 0$, and reveals the biperiodicity of C_d, feature not observed in the phase diagrams for the intermediate angle $\theta = 15.3°$.

An increase of the Reynolds number reduces the values of the drag coefficient for $\theta = 0°$. We find the opposite effect regarding $\theta = 45°$, where the values of C_d are augmented, whereas for the intermediate angle 15.3°, the shift is not as remarkable when Re increases. The behaviour of C_l is more obvious: in all cases we find higher peak-to-peak lift fluctuations as Re increases. These results are consistent with those shown in Fig. 4.10 and were also reported in [76].

As shown in Fig. 4.11, the effect of applying CBC at the outlet (cyan/blue lines) is to reduce the instantaneous drag fluctuations, specially at high Re. It is also worth to mention that the overall values of the drag are slightly reduced when the CBC is applied at the inlet (blue-solid line). This effect is in agreement with the overall drop of C_D already observed in Fig. 4.10. When Re> 110, the shape of the patterns of the reflective and non-reflective conditions at the outlet differ considerably. Particularly, $\theta = 0°$ shows a different phase shift. The use of a reflective BC at the outlet produces also wider C_d oscillations. Moreover, consistently with the reduction of the drag pointed out above, the use of a non-reflective BC at the inlet shifts the phase diagrams to the left. In other words, CBC at the outlet results in diminished perturbations on the wake past the object and the oscillations of the drag are diminished. In contrast, CBC implementation at the inlet reduces the reflections produced by the upstream faces of the obstacle, and net drag is thus reduced, without further diminishing the drag oscillations.

4.4.3   Recirculation Length Ratio

We have seen throughout the analysis how the width of the channel influences the forces experienced by the immersed object, and one expects a similar effect on the recirculation length, which is a measure of the time-averaged topology of the flow around the obstacle.

A comparison of the results of the recirculation length ratio L_r/h (in a time-averaged vortex cycle) obtained for the different BC configurations is presented in

(a) $\theta = 0°$ and $AR = 1/8$

(b) $\theta = 0°$ and $AR = 1/16$

(c) $\theta = 15.3°$ and $AR = 1/8$

(d) $\theta = 15.3°$ and $AR = 1/16$

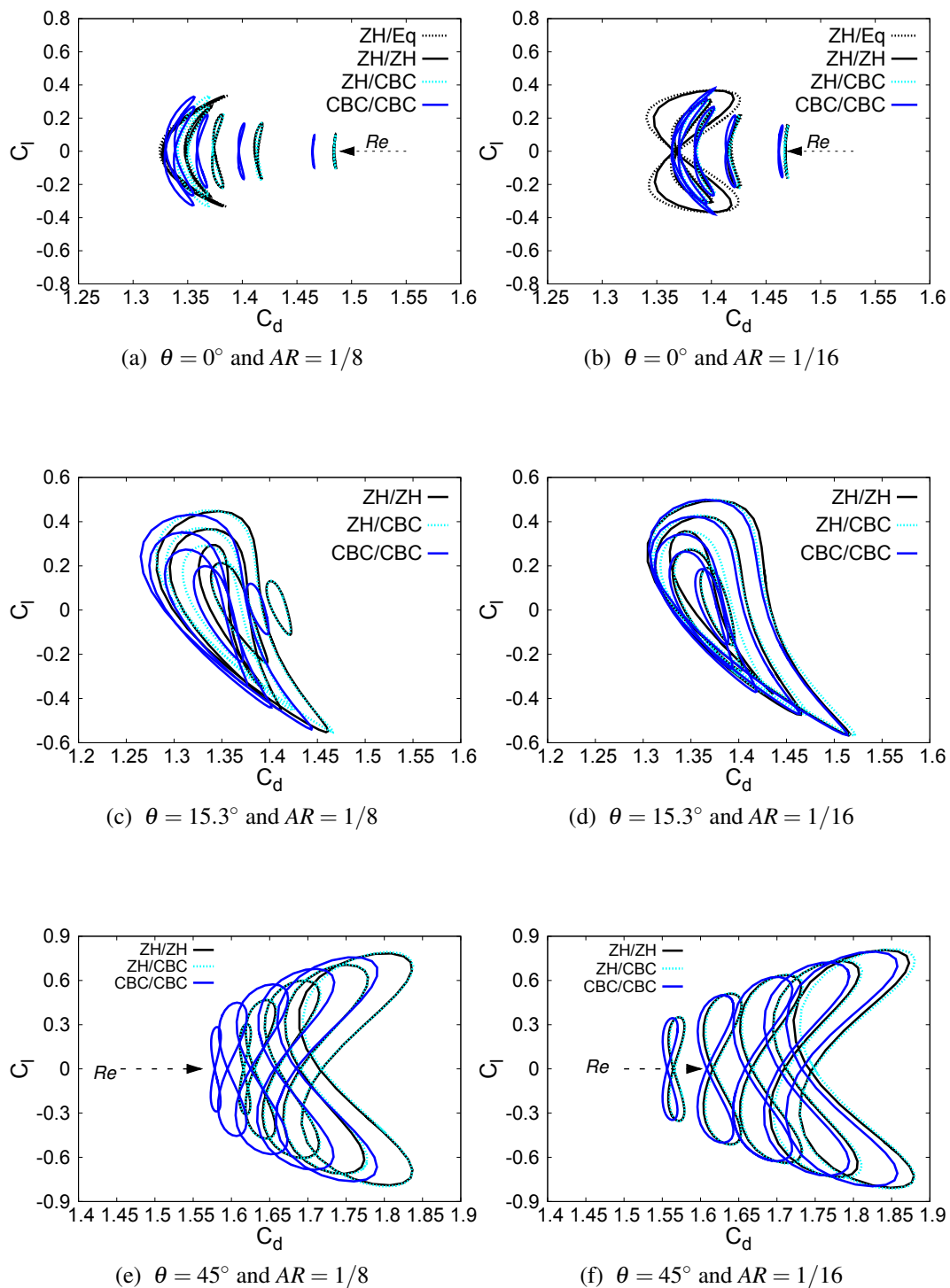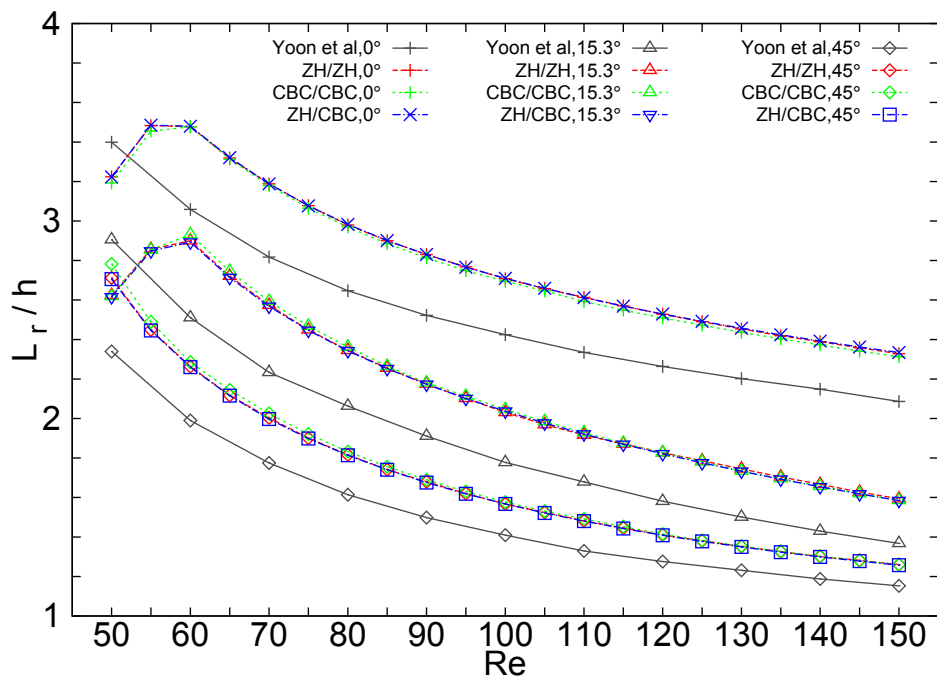(e) $\theta = 45°$ and $AR = 1/8$

(f) $\theta = 45°$ and $AR = 1/16$

Fig. 4.11 Phase diagrams for $\theta = 0, 15.3$ and $45°$ for the four BC configurations studied: ZH/Eq (black-dashed), ZH/ZH (black-solid), ZH/CBC (cyan-dashed) and CBC/CBC (blue-solid lines), for a) $AR = 1/8$ and b) $AR = 1/16$.

Figs. 4.12a, 4.12b, for $AR = 1/8$ and $1/16$ respectively. Again, the results for the ZH/Eq configuration have been omitted as they do not significantly differ from those of ZH/ZH. The reference values by [76] are also shown mainly as a guide because they were obtained at a very different blockage ratio (1%) which means nearly freestream conditions, far from our channel aspect ratios. Yet one can observe how the results for $AR = 1/16$ get closer to the results of [76]; as a matter of fact, simulations made with even wider channels should confirm a much closer agreement. For the present discussion, however, it is more informative to focus our attention onto bigger values of AR. The ZH/ZH and ZH/CBC trend lines do not show significant differences in from Fig. 4.12. In Fig. 4.12a, the CBC/CBC combination renders slight L_r/h differences, with respect to either ZH/ZH or ZH/CBC, specially at low Reynolds numbers. In addition, in Fig. 4.12b, the biggest differences between CBC/CBC and the inlet-reflective combinations are detected for $\theta = 0°$ when the Reynolds number is increased. In this case, the non-reflecting nature of the CBC has a greater impact on L_r/h if applied at the inlet than at the outlet. This layout of the obstacle walls might be an important factor to take into account due to the fact that the obstacle and channel walls are parallel. The pressure waves that propagate in the y-direction between the channel walls and the obstacle will bounce repeatedly until viscous dissipation damps them. As an example, we can observe in Fig. 4.12b that the trends of CBC/CBC with the angle of incidence equal to zero significantly differ from those with reflecting BC at the inlet beyond $\text{Re} \gtrsim 80$. On top of that, while the relative difference between the values of CBC/CBC and the values reported in [76] remains similar for all the different blockages, the ZH/CBC and ZH/ZH values show an increasing relative difference with the Reynolds number if they are compared with the reference values. We infer that this reported divergence of recirculation length at high Reynolds numbers ($\text{Re} \gtrsim 80$) and for $\theta = 0°$ between reflective and non-reflective BCs at the inlet is a consequence of the reflection of pressure waves at this particular angle of incidence plus the fact that it is incremented with less blockage effect. Nevertheless, a deeper study of this phenomenon should be considered.

4.4.4 Thompson vs LODI CBCs

We now carry out a comparison of the flow variables for two types of characteristic BCs applied at the outlet: LODI- and Thompson-CBC. The density, x-velocity and y-velocity are shown respectively in Fig. 4.13. To provide an additional perspective, the reflecting BC values are also included.

Both reflective boundary conditions (Eq and ZH) set a constant density at the boundary and, in the case of ZH, the y-velocity vanishes at the outlet. As a result,

UNIVERSITAT ROVIRA I VIRGILI
REVIEW OF BOUNDARY CONDITIONS AND INVESTIGATION TOWARDS THE DEVELOPMENT OF A GROWTH MODEL: A LATTICE
BOLTZMANN METHOD APPROACH
Albert Puig Arànega

70   Reflective vs non-reflective boundary conditions

(a) Plot of L_r vs Re, $AR = 1/8$
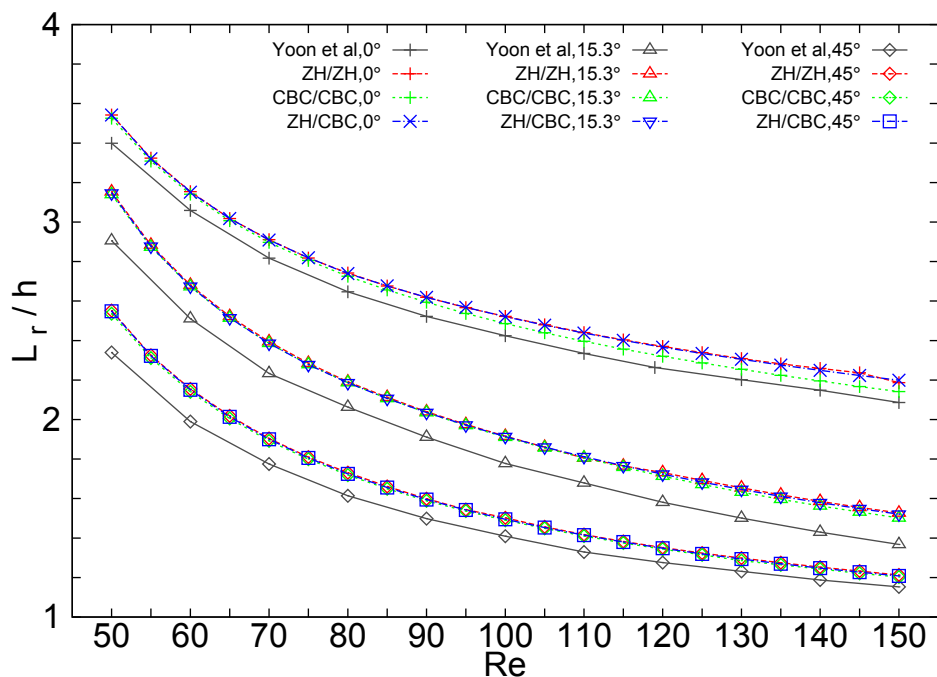
(b) Plot of L_r vs Re, $AR = 1/16$

Fig. 4.12 Plot of L_r vs Re for a)$AR = 1/8$, and b)$AR = 1/16$. for the four different BC configurations studied, ZH/ZH (red-short-dashed lines), ZH/CBC (blue-long-dashed) and CBC/CBC (green-dot-dashed lines). Different symbols correspond to the three angles considered: $\theta = 0°$ (plus and crosses), $15.3°$ (triangles and inverted triangles) and $45°$ (squares and diamonds), and solid black lines refer to the results of [76].

Fig. 4.13 y-profiles of the averaged macroscopic quantities at the outlet for Re = 100 and $\theta = 0°$: density (a), x-velocity (b) and y-velocity components (c).

the macroscopic quantities display a discontinuity at the outlet. That is why, in order to compare relevant information from the four different BC scenarios, the *y*-profiles shown in Fig. 4.13 are not for the boundary nodes (the last column of the domain), but for the previous column. The *y*-profile of the cycle-averaged density at the outlet i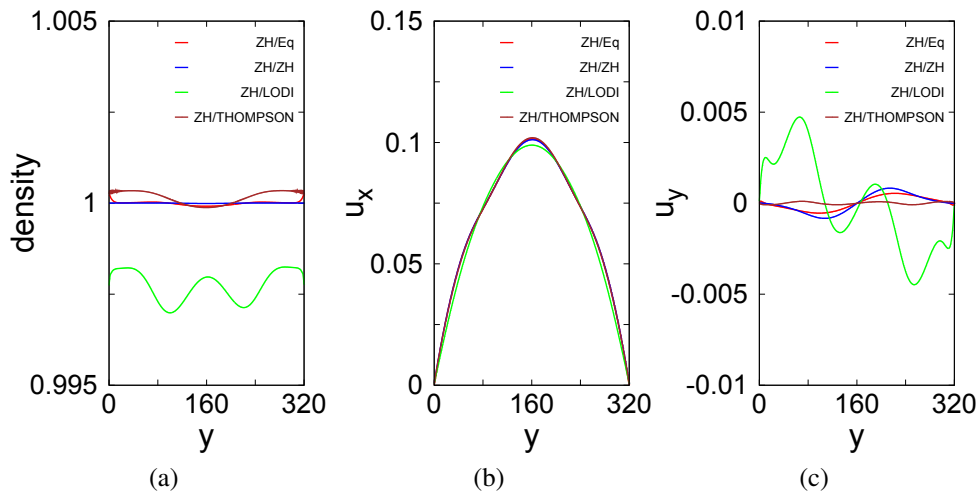s shown in Fig. 4.13a, where three facts are worth a comment. Firstly, the density profiles of the non-reflecting boundary conditions (LODI and Thompson) oscillate along the y-section, while the ZH and Equilibrium BCs show a constant density at the outlet. In addition, the LODI-CBC density values are visibly shifted downwards about 0.35-0.20% from the reference density at $\rho = 1$. Remarkably, the Thompson-CBC density values fall much closer to the reference density.

The cycle-averaged profiles of the x-velocity u_x are shown in Fig. 4.13b. At exception of the LODI, which reaches a more parabolic-like profile, the shape of the u_x profiles is not fully parabolic in the rest of the cases studied.

The net flow along the *y*-direction tends to zero as the antisymmetry of all the profiles shown in Fig. 4.13c indicates but, unlike the density and the x-velocity, the solution for the LODI-CBC cycle-averaged y-velocity (u_y) profile differs significantly from the rest. The Thompson u_y profile shows small averaged u_y velocities, which are similar to those obtained with the two reflective boundary conditions. The LODI values instead, differ from all the rest, showing spurious contributions to the averaged u_y throughout the entire profile.

In order to understand the extent and nature of these irregular LODI values in Fig. 4.13c, a zoomed view of the cycle-averaged u_y contours for LODI and Thompson approaches is illustrated in Fig. 4.14. The coloured shades are scaled to a maximum

UNIVERSITAT ROVIRA I VIRGILI
REVIEW OF BOUNDARY CONDITIONS AND INVESTIGATION TOWARDS THE DEVELOPMENT OF A GROWTH MODEL: A LATTICE
BOLTZMANN METHOD APPROACH
Albert Puig Aranega

72   Reflective vs non-reflective boundary conditions

value of 0.001 in LB units, which is two orders of magnitude below the maximum value of u_y in the whole domain. In other words, the scale is magnified in order to detect minimal perturbations. Additionally, the velocity vector field is zoomed and included as an inset. Fig. 4.14b shows the Thompson solution with barely visible averaged u_y at the outlet, whereas the LODI solution displays the unnatural behaviour mentioned above: in Fig. 4.14a, artificial u_y contributions have their origin at the boundary, distorting the cycle-averaged velocity field. The zoomed view of the velocity vectors confirms that the velocities slightly deviate from the x-axis direction, for the LODI-CBC case.

Note that the CBC method is also a Dirichlet type of BC, with macroscopic values of density and velocity updated at each timestep. The reduced density values in the LODI density profile are related to the one-dimensional basis of the LODI equations, as the y-derivatives are omitted in the LODI-CBC algorithm. The same applies to the velocity profiles, which show unrealistic behaviour (Fig. 4.13c). The flow structures that propagate from the obstacle are greatly damped when they reach the outlet, but the vorticity is still significant and the averaged x-velocity profiles should not necessarily be parabolic (Fig. 4.13b). Additionally, the averaged outlet y-velocities should fall close to zero everywhere, but this is not the case for the LODI-CBC results. It is important then to consider the Thompson CBC treatment and incorporate the derivatives in the y-direction in problems with spatial structures leaving the boundaries. Notwithstanding this evidence, the distorted velocity field at the outlet is of a very local character and its effect on the forces, when the obstacle is far away from the boundary as in our case, is negligible (the averaged C_D not showing deviations larger than 0.3% for the range of Re considered).

4.5   Conclusions

Within the framework of the Lattice Boltzmann Method, a comparison of reflective and non-reflective boundary conditions has been presented by means of a parametric study of the drag and lift forces and the characteristics of the flow past a square obstacle in a channel. In addition to this, an analysis focused on Thompson-CBC and LODI-CBC has been carried out at the outlet.

By applying non-reflective boundary conditions at both inlet and outlet, both the cycle-averaged drag coefficient and its amplitude oscillations are reduced. This reduction is more relevant as Re increases.

We have shown that both LODI and Thompson CBC methods are worth to consider within the low-Reynolds number regime, in problems where objects are immersed in
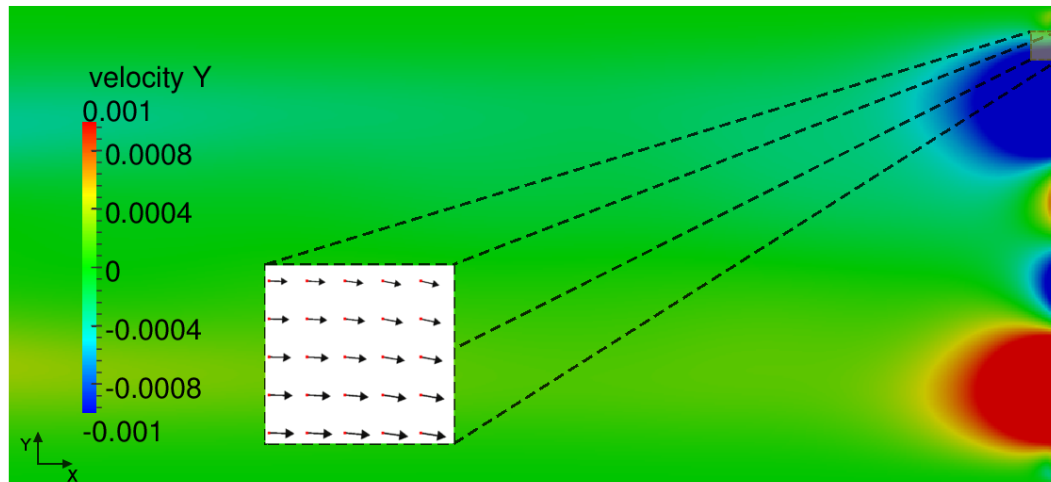
(a) LODI-CBC at the outlet
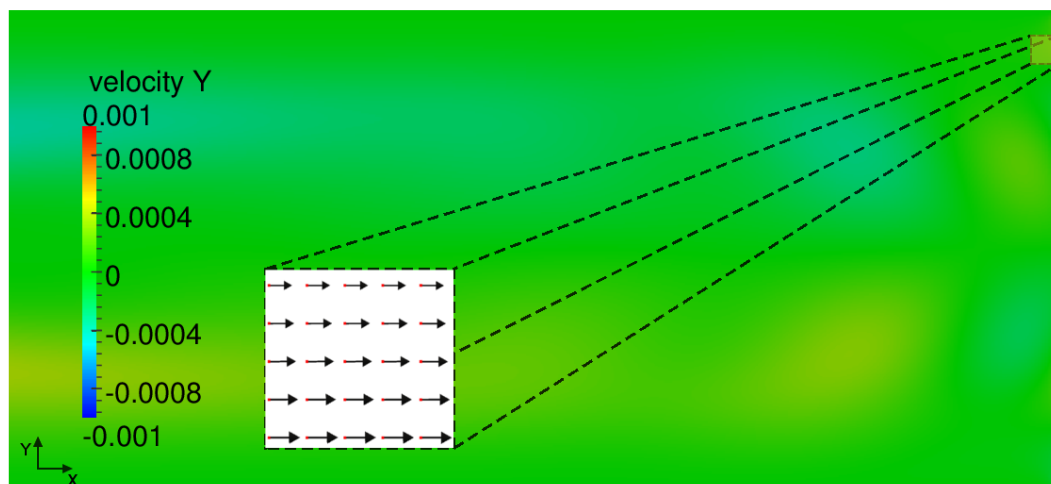
(b) Thompson at the outlet

Fig. 4.14 Cycle-averaged u_y at the channel outlet, covering the full section from node 1380 to node 2080 in the x-axis. Re= 100, $\theta = 0°$, $AR = \frac{1}{8}$. Inset: zoomed area of the velocity vector field from the top highlighted area of the outlet.

the flow and vortex structures propagate to the outlet boundary. At higher Re, where viscous effects become less important, the effect of CBC may become even more determinant, as the trend of the results presented indicates. CBC at the inlet indeed absorb persistent pressure waves that propagate close to the inlet, specially when the top/bottom walls of the obstacle are parallel to the walls of the channel.

We have observed remarkable differences when analysing LODI vs Thompson approaches. While both provide the expected drag and lift forces and remove pressure wave reflections, the LODI-CBC approach becomes inappropriate when the dimensionality of the flow increases, producing abnormal velocity profiles at the outlet. In these cases we observe that the Thompson characteristic approach provides a more accurate flow solution.

Chapter 5

Platelet modelling

We have described the blood platelets, its function in the coagulation process and the motivation for the scientific community to numerically simulate such phenomenon in Sec. 2.5.2. In the same section, we additionally proposed a margination model with a drift term to reproduce the platelet margination by means of a drift force term added to the evolution equation that led to Eq. 2.81.

Furthermore, we briefly explained the thrombosis phenomenon, the key role that platelets play, and proposed a surface reaction model at Secs. 2.5.3 and 3.2.1. The proposed equation (see Eq. 3.10) can be used to develop a preliminary platelet binding model. Once this step is validated, we could implement a computational region algorithm to enable the thrombus growth in the simulation (see Fig. 2.7). Hence, it is of prime importance to first validate the reaction rates in order to correctly reproduce a hypothetical thrombus growth.

In this section, the margination drift term described in Chapter 2 and the platelet binding model with a surface reaction described in Secs. 2.5.3 and 3.2.1 are examined. We will first expose the used physical model and subsequently analyse the features of the described tools on the former chapters. We will finally show the obtained outputs and compare them with the available literature.

5.1 Numerical and physical details

The physical domain consists of a closed channel where we consider a developed Poiseuille flow (Eq. 4.1) at the inlet and a fixed pressure condition at the outlet. Both conditions are applied with the aid of ZH-BC Eq. 3.20. The top and bottom walls are no-slip using the mid-way BB. The grid considered is uniform, 100×500. Typical lumen diameters for coronary arteries are ranged from 0.5 to 5mm in normal men [17]. We choose a physical diameter of 0.003m and a length of 0.015m for
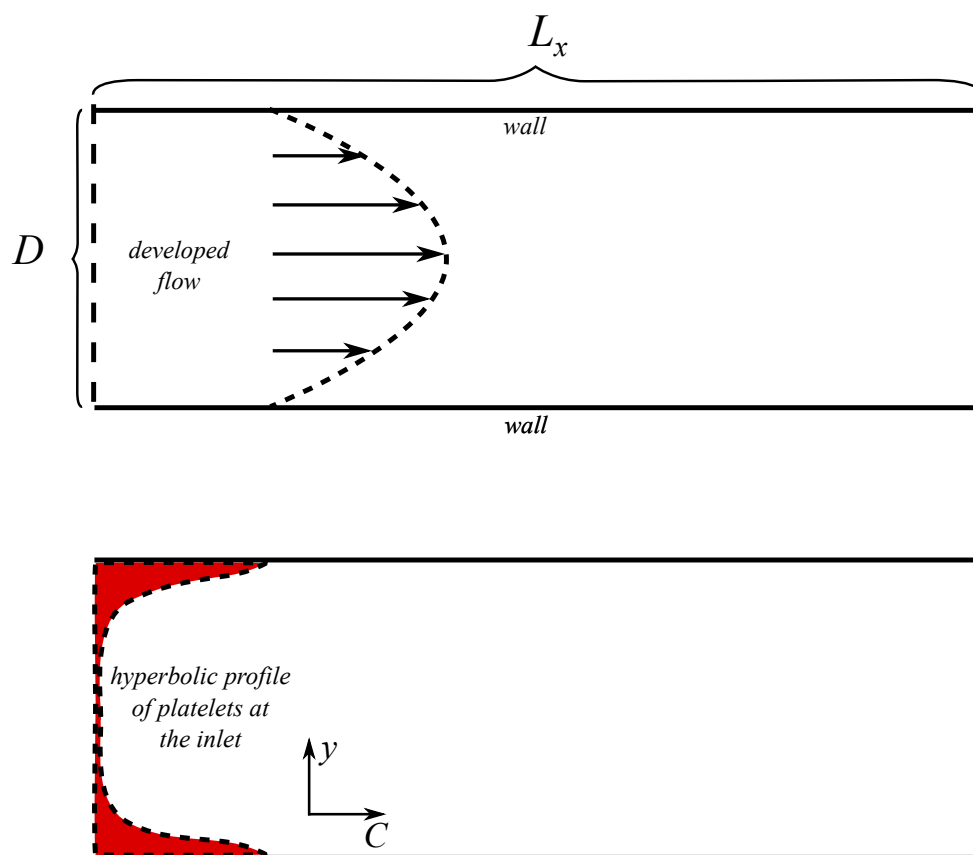
Fig. 5.1 The upper figure shows the flow conditions, with a developed flow at the inlet and a pressure condition at the outlet, both using ZH approach. The bottom figure shows the passive scalar initial condition. At the inlet, we set the hyperbolic platelet concentration profile from Eq. 2.80, and at the outlet, the unknown distributions are calculated with an equilibrium boundary condition.

this study. We as well set a common blood flow rate for this artery diameter [38]. Table 5.1 gathers the used parameters for the simulations. For this study, the diffusivity is artificially increased in order to speed up the simulations and to avoid possible numerical instabilities (also explained in Sec. 2.5).

The inlet concentration profile is set as in Eq. 2.80 with a Dirichlet condition (Eq. 3.8). Figure 5.1 depicts the hydrodynamic (upper figure) and the passive scalar (bottom figure) models used with this domain.

5.2   Validation of the passive scalar LBM

5.2.1   Validation of the advection-diffusion equation

We first validate the ADE with the following set up: a square domain $L_x = L_y = 2m$ with periodic boundaries and a fixed velocity of $u_x = u_y = 0.8m/s$. An initial concentration

Table 5.1 Constants used in the model

Nomenclature	Value	Description
a	$4\mu m$	Particle scale collisions of the order of a RBC
k	0.15	Constant for the enhanced diffusion model
D_{th}	3.1×10^{-14} m²/s	Thermal diffusion coefficient
D_p	1.55×10^{-7} m²/s	Arbitrary thermal diffusion coefficient
D_e	3.04×10^{-9} m²/s	Enhanced thermal diffusion of coefficient
β	-7.87	Constant for the tanh function used in the platelet profile
δ_p	0.77	Constant for the tanh function used in the platelet profile
k_{th}	1.38×10^{-23} m² kg/s²	Boltzmann constant
k_{rt}	$10^{-3}, 10^{-4}$	binding constant rates used at Sec. 5.2.2 and Sec. 5.4, respectively [38].
ρ	1025kg/m³	plasma density
μ	0.0038kg/m/s	dynamic viscosity of blood at high shear rates
R	0.0015m	radius of the channel
L_x	0.015m	Length of the channel
δ_f	$0.6L_x$	Length of the reacting surface
Q_0	2ml/s	Blood flow at the channel
R_{eq}	$1.9\mu m$	Equivalent radius of a sphere of a platelet
T	310K	Temperature

field is applied as a Gaussian-like pulse [51] with the following form

$$C_0(x_d, y_d) = \exp\left(-\frac{(x_d - x_{d,0})^2}{D_{d,x}} - \frac{(y_d - y_{d,0})^2}{D_{d,y}}\right), \tag{5.1}$$

where Eq. 5.1 is non-dimensionalised. Both x and y indexes are $x_d, y_d \in [0,2]$, the initial position $(x_{d,0}, y_{d,0}) = (0.5, 0.5)$ and $D_{d,x}$ and $D_{d,y}$ are the diffusion coefficients in each axis direction. We define the diffusion to be isotropic with $D_d = 0.01$. We run a simulation up to time $t = 1.25s$ and we compare the results with the analytic solution for this problem,

$$C(x_d, y_d, t_d) = \left(\frac{1}{1 + 4t_d}\right) \exp\left(-\frac{(x_d - u_{d,x}t_d - x_{d,0})^2}{D_x(1 + 4t_d)} - \frac{(y_d - u_{d,y}t_d - y_{d,0})^2}{D_y(1 + 4t_d)}\right). \tag{5.2}$$

Equation 5.2 is the two-dimensional analytic solution of a Gaussian pulse with certain diffusion coefficients D_x, D_y, advected with a certain velocity (u_x, u_y) [51].

We use uniform grids with 80×80 and 120×120 nodes. The obtained results are displayed in Fig. 5.2 and show a combination of the different meshes and relaxation time schemes (MRT and SRT) used for the validation. In Fig. 5.2b we can appreciate the second norm error for the considered parameters. We can observe that there is a significant reduction of the error when MRT is used, and these discrepancies are further reduced by refining the mesh 1.5 times. With this validation, we decided to use the MRT scheme for the simulation.
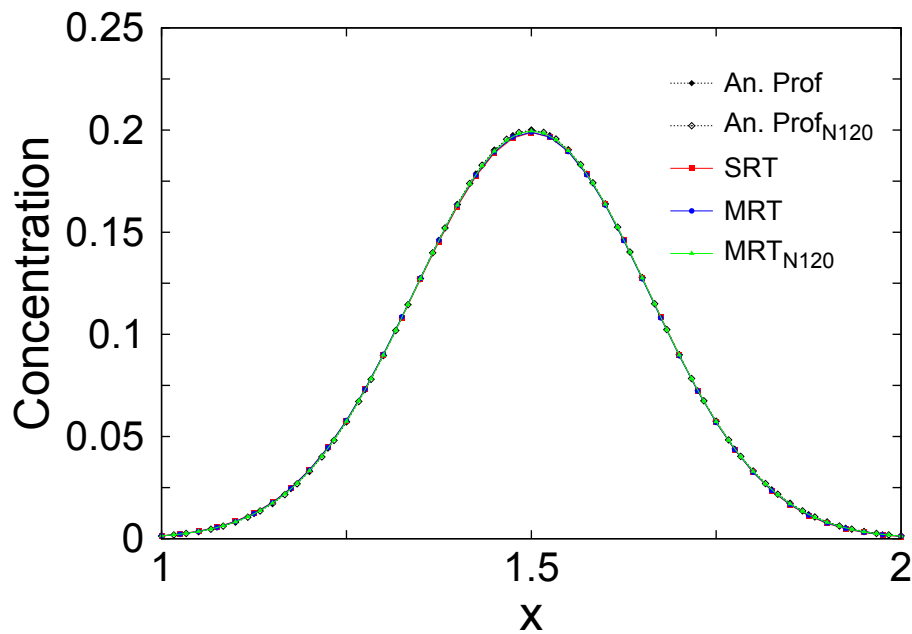
(a) Numerical results of concentration of the Gaussian pulse after $t = 1.25$.
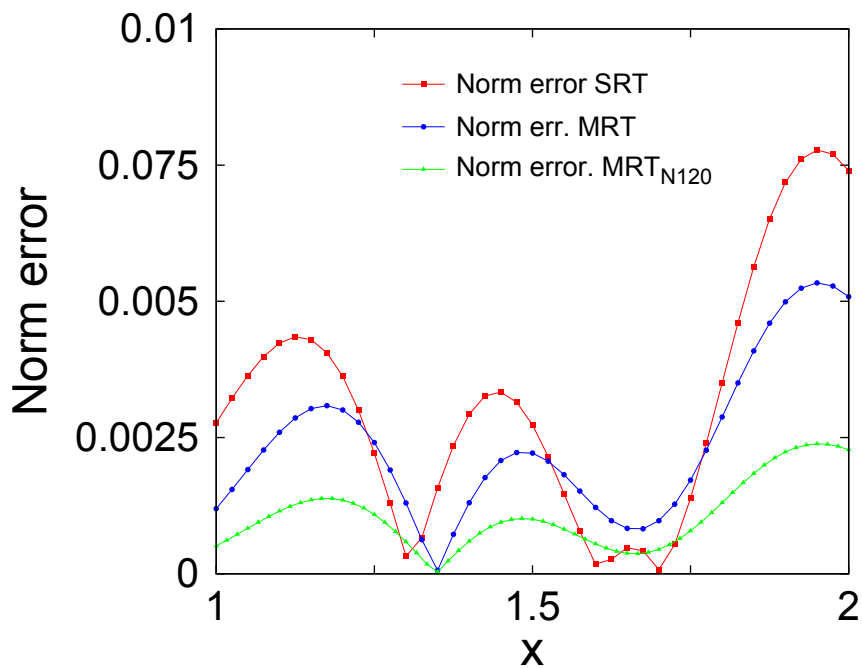
(b) Local norm errors from Fig. 5.2a.

Fig. 5.2 Plot concentration profiles and its local norm errors in the region $x = [1,2]$ and $y = 1.5$. Numerical tests include: N80 with SRT, N80 with MRT, N120 with MRT. a) Concentration profiles. Black dotted lines are the analytic solution profiles, red line is the SRT profile with N80 grid, blue line is the MRT profile with N80 grid and the green line is the MRT concentration profile with 1.5 times refined grid. b) Local norm error of Fig. 5.2a values. Red is SRT errors, blue is MRT errors and green is MRT with a grid 1.5 times refined

5.2.2 Validation of the reaction kinetics model

We consider a preliminary kinetic reaction in the bulk fluid as a sink term in the ADE equation that governs the passive scalar dynamics.

We consider a first order reaction rate of $k_{rt} = 10^{-3}\text{s}^{-1}$. This parameter is also considered at [38]. The total time for the reaction is 10^4 seconds, which is arbitrarily set to give enough reaction time to completely remove the reactant with concentration C. The analytic formulation can be straightforwardly derived from the following expression,

$$C(t) = e^{-k_{rt}t}. \tag{5.3}$$

Figure 5.3a shows the agreement of our simulations with the analytic results, which is enhanced with a lower δt as seen in Fig. 5.3b, as the norm errors are sensibly decreased.

5.3 Margination parameter of the drift term

In this section we aim at determining the value of the optimal margination parameter M_{cd} (described in Sec. 2.5.2) for the model described in Sec. 5.1. The value of M_{cd} is directly related to the magnitude of the drift force in Eq.2.79. For this purpose, we do not implement any reaction at the boundary. The optimal M_{cd} is determined by trying a set of different values within a range, and selecting the one which 1) keeps the near-wall concentration *constant* and 2) *closest to the values of the potential field concentration taken as a reference*. The range of reported values is $M_{cd} \in [8, 11]$, which corresponds to the range of better platelet cross-sectional concentration profiles, according to the two aforementioned criteria. Figure 5.4 shows the evolution of the near-wall platelet concentration along the channel. In this figure, we can observe the importance of the drift term ζ for the specified values of the M_{cd} parameter. The black dashed line corresponds to the reference value of the concentration on the wall, which should keep constant along the channel, while the black line line corresponds to the wall concentration without the margination term implemented. A general drop of the concentration is observed near the inlet, and a similar phenomenon occurs at the outlet. This phenomenon is due to the fact that the boundary conditions do not include the drift term, combined with the effect of a relatively large material diffusivity (see data in Table 5.1). Thus, the vertical g_is streaming from the limiting wall-nodes of the domain make a noticeable impact on the inner nodes. These two factors end up in an initial decay of the concentration near the wall. The contribution of the drift term does not fully revert this first diffusive flux, but still, if a high enough M_{cd} is chosen, the wall concentration gradually recovers.
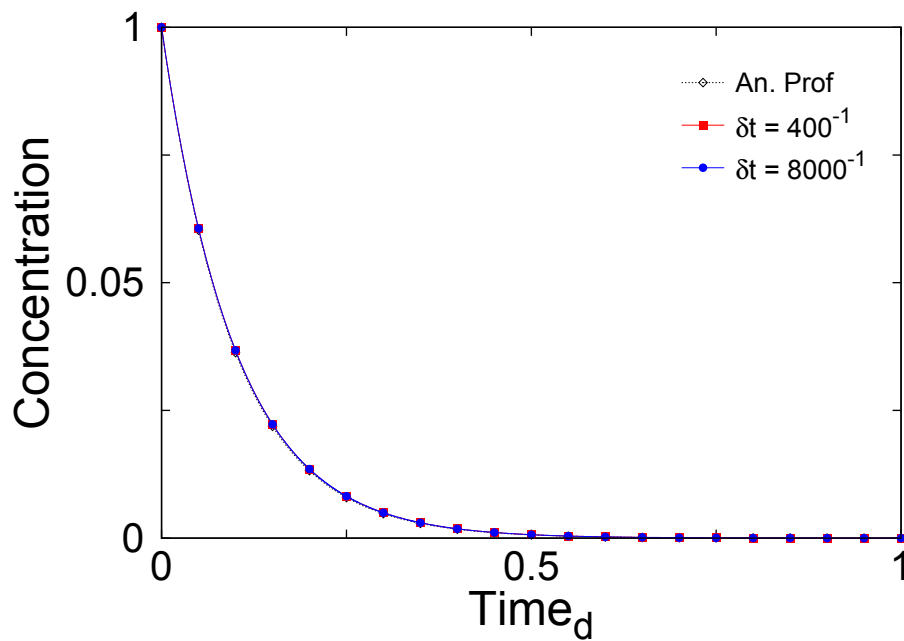
(a) Test example: Concentration of reactant *C vs*. time.
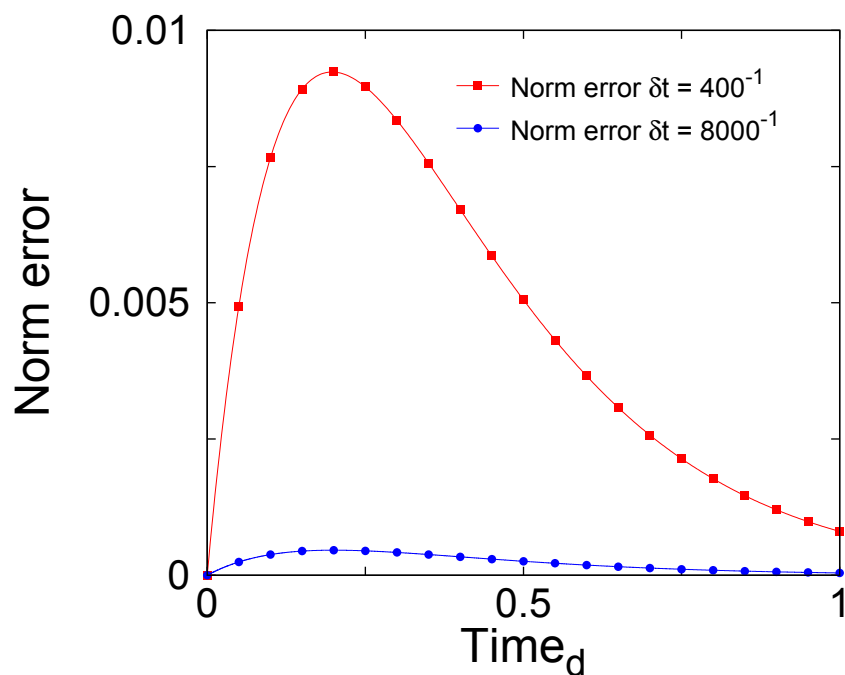
(b) local norm errors from Fig. 5.3a.

Fig. 5.3 Test case. Concentration evolution in time. a) Concentration versus time. Black dotted line is the analytic solution, red line is the done with a $\delta t = 400-1$ and blue line with a $\delta t = 8000-1$. b) Local norm error of Fig. 5.3a values. Red line are the errors using the $\delta t = 400^{-1}$, blue line are the errors using the $\delta t = 8000-1$
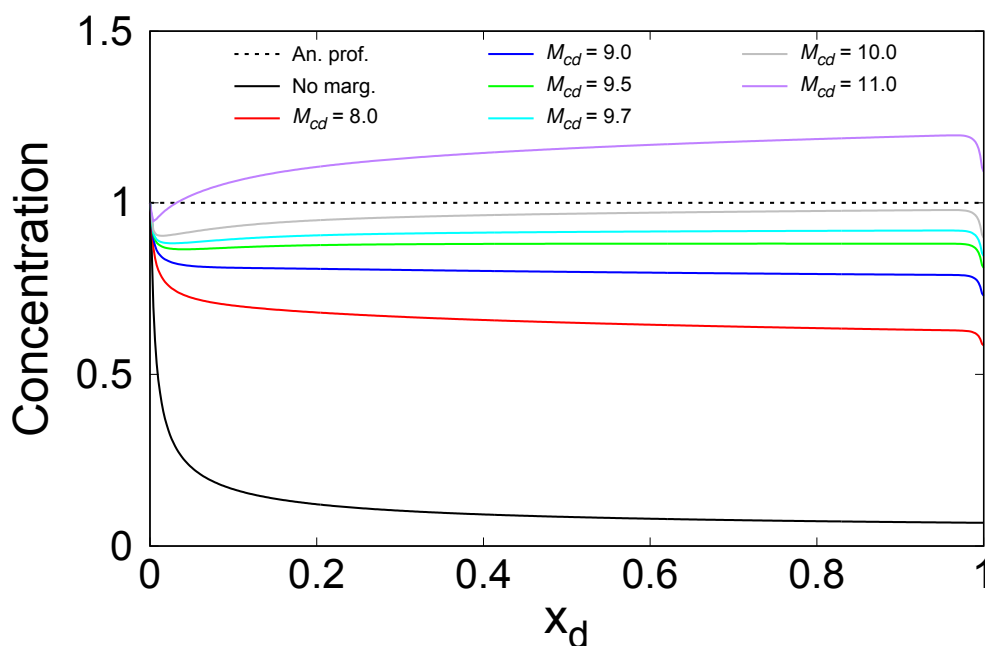
Fig. 5.4 Platelet concentration on the wall as a function of the x_d coordinate along the channel. Different margination parameters were used, $M_{cd} = [8.0, 9.0, 9.5, 9.7, 10, 11]$.

When $M_{cd} = 8$ (red line), the diffusion flux close to the wall is clearly larger than the drift term, as the wall concentration keeps diminishing along the channel. The same happens but at a less extent when $M_{cd} = 9$. Nonetheless, the wall concentration is kept fairly constant for $x_d \in [0.4, 0.9]$ for $M_{cd} = 9.5$. As the margination parameter is increased beyond $M_{cd} > 9.7$, the concentration raises after the initial decay at the inlet, without reaching a constant value along the studied channel. Nevertheless, the trend of the margination values of $M_{cd} > 9.7$ suggests that the concentration would eventually achieve an constant asymptotic concentration value with a longer channel. Specifically, when $M_{cd} = 10.0$, we can foresee that the concentration at the wall would reach an asymptotic value that would be much closer to the analytic platelet concentration profile than the asymptotic value obtained at $M_{cd} > 9.7$. However, we only considered this particular channel length to preserve a fine mesh with a good computational performance. Additionally, in a more advanced scenario, it would be inefficient to simulate a very long channel upstream just to reach a perfect platelet profile at the moment that the flow crosses the active area of study (e.g.,a hypothetical surface reaction or an obstacle).

We now take a closer look at the cross-sectional distribution of the concentration for different longitudinal coordinates. The three plots in Fig. 5.5 show the zoom of the cross-sectional concentration for the values of the margination parameter that present a better behaviour near the wall (according to our previously established criteria)

$M_{cd} = [9.0, 9.5, 9.7]$. We can see that all the plotted concentration profiles follow the potential field values C_{eq} (C_{eq} values correspond the initial condition, when $x_d = 0$) with a reasonable agreement everywhere with the exception of the wall, where the desired concentration specified by the potential field is not reached. This phenomenon occurs due to the fact that the concentration gradients on the wall are extreme for this C_{eq} profile.

We additionally observe in Fig. 5.5b that $M_{cd} = 9.5$ is the optimal value because it best keeps the concentration at the walls constant in the desired channel region ($x_d \in [0.4, 0.8]$). In fact, the relative difference between the concentration at $x_d = 0.4$ and $x_d = 0.8$ is below 0.05%. This constant longitudinal concentration is indeed a critical attribute to take into account if we want the model to be steady. On the other hand, if the margination parameter is increased, for $M_{cd} = 9.7$ a progressive increase of the wall concentration along the channel is obtained, (Fig. 5.5c, whereas the values of the wall concentration are closer to the potential field values C_{eq} than those obtained with $M_{cd} = 9.5$.

One possible simple solution to overcome the concentration decay near the walls observed in Fig. 5.4 would be to supply the initial concentration profile with a higher concentration at the wall. This procedure could be applied by taking the results from Fig.5.5 as a feedback to correct the concentration decay on the walls, similarly as it was done for the velocity correction used in Sec. 4.2.4. Nevertheless, more research should be done on this feature with different longitudes of the channel to improve the results and to optimise the M_{cd} parameter. Additionally, the algorithm should be also improved in order to minimise the first early decay.

5.4   Reaction on a surface

We enable a surface sink reaction in the cent er of the channel wall with a total length of $x_d \in [0.2, 0.8]$, where we apply the reaction using Eq. 3.10. The numerical model is the same as in Sec. 5.3. Initially, we set for the whole channel the same inlet concentration ($C_0 = 1$), and we fix a developed velocity field. We do not activate neither the thrombosis computational region algorithm (illustrated in Fig. 2.7) nor the enhanced diffusion model (See 2.5.1) as we seek to firstly validate the surface reaction model. Therefore, we set a constant diffusivity for the passive scalar that is high enough to let the simulation run smoothly whether the simulation is coupled with the hydrodynamic model or not (the problem of coupling both the hydrodynamic and material transport models has been explained in Sec. 2.5). At the same time, we keep a high Péclet number in the channel (see Table 5.1 for the rest of the parameters used).
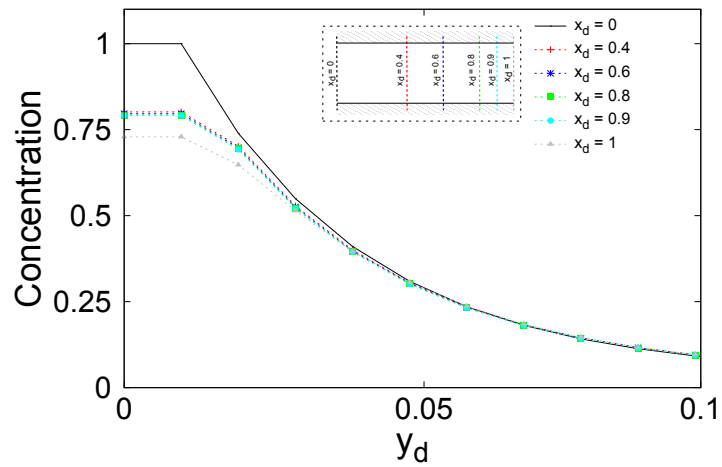
(a) $M_{cd} = 9.0$.
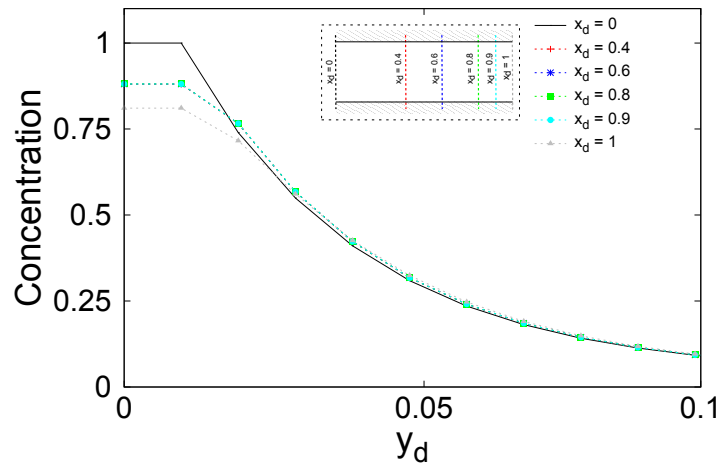
(b) $M_{cd} = 9.5$.
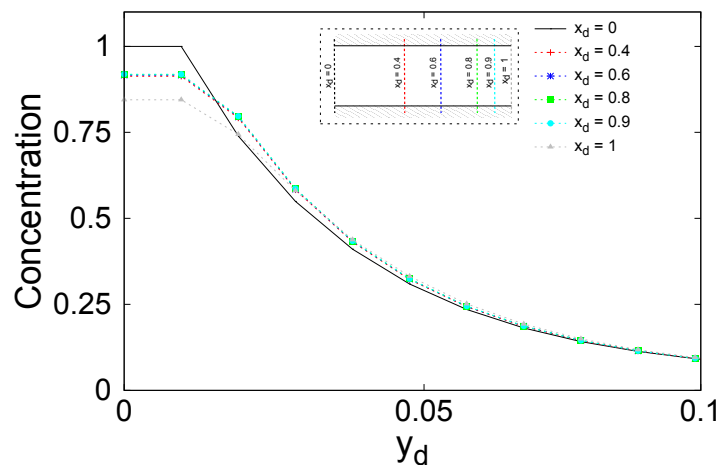
(c) $M_{cd} = 9.7$.

Fig. 5.5 Cross-sectional concentration profiles at different longitudinal levels of the channel. a) $M_{cd} = 9.0$ b) $M_{cd} = 9.5$ c) $M_{cd} = 9.7$

Fig. 5.6 Test case for a Schmidt number of 23, Péclet number of around 446 (based on the shear rate and reacting surface) and a constant reaction rate $k_{rt} = 10^{-4} m/s$. This is a qualitative image to show the steady mass transport boundary layer thickness.

We would like to emphasise that this reaction model is not considering the platelet deposition step. Instead, we consider a plain first order reaction as in Sec. 5.2.2, with a kinetic reaction constant for the binding platelets of $K_{rt} = 10^{-4} m/s$ [38] that has also been used for the platelet aggregation step. To speed up the simulation to its steady state, we have reduced the number of computational nodes to a half by applying a symmetric BC (see Eq. 3.7) at the centerline of the channel. Fig. 5.6 shows the concentration field in the steady state. One can see from Fig. 5.6 that around the Péclet number of 450, the boundary layer is very small if compared with the hydrodynamic boundary layer, where the latter covers the whole radius of the channel in a laminar developed flow. This fact lets us assume a constant shear rate in the area covered by the mass transport boundary layer. We therefore change the hydrodynamic field of the simulations from a Poiseuille flow to a Couette flow. With this assumption, we use the wall shear rate (calculated as explained in Sec. 2.3.3) as an input for the constant shear rate of the Couette flow. With this transformation of the physical model, we can compare the results of the Sherwood number obtained from our simulations with the analytic ones, Eq. 2.84. Additionally, the physical domain of the simulation can be significantly reduced with this transformation. Fig. 5.7 shows the discrepancies between the analytic and numerical solution of the Sherwood number characterising the mass transport at the reactive wall, using different mesh refinements. A general good agreement is observed. Such agreement is even more explicit as the grid density is increased. In order to speed up the simulations with the higher grid resolutions, the domain size was gradually divided by lowering the height. This procedure has been applied taking into account that the mass transport boundary layer does not reach the upper boundary of the considered domain (see the sketch of this reduction procedure in Fig. 5.8).

The averaged relative errors of the Sherwood number with respect to the analytic values are displayed in Table 5.2. Table 5.2 confirms that the relative error of the averaged Sherwood number starts to converge on the finer $N = [150, 200]$ meshes,
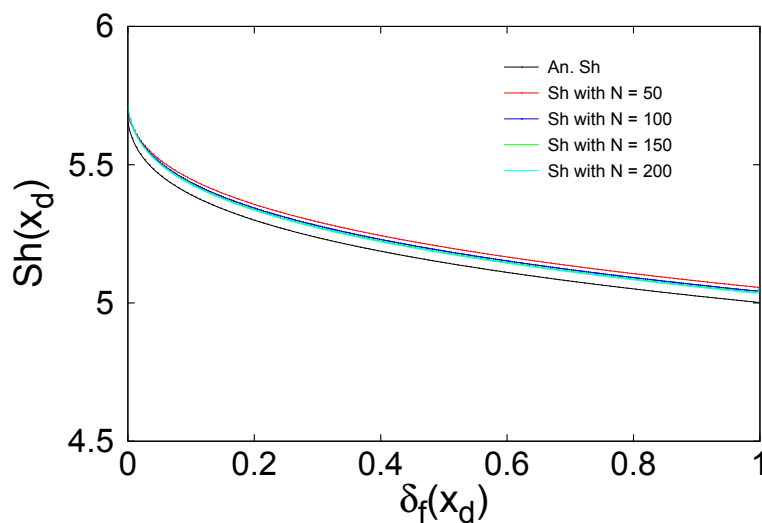
Fig. 5.7 Local Sherwood number on the reactive wall of the channel, along the channel length. Four different mesh refinements and the theoretical solution (Eq. 2.84, black line) are shown.

Table 5.2 Relative errors of the averaged Sh with different mesh refinements.

Number nodes of radius N	Relative error (%)
50	1.367
100	0.8825
150	0.721
200	0.638

which means that the numerical solution can be assumed to be mesh independent for $N = 200$ with a relative error below 0.65%.

To put these values in the context of the application, the shear rate used for the simulations is of approximately $380s^{-1}$. This shear rate, used in the Couette flow configuration was actually the wall shear rate of the developed flow in the channel, simulated using the parameters of Table 5.1. The magnitude of this shear rate is sensibly higher than the shear rates typical of a healthy coronary artery [60]. In fact, to extrapolate our model to an ill artery, such as a stenosed artery or an eventual thrombosis, one must take into account that the shear rates may experiment increments from one to three orders of magnitude [38]. We also have to take into account that the diffusivity of the fluid used for these simulations (Table 5.1) was trivially set in order to avoid possible numerical instabilities, but yet it was low enough to be in the range of high Péclet and Schmidt numbers ($Re_{\delta_f}Sc^{1/2} \approx 445$), which enable the assumption made in Sec. 2.5.3 and 3.2.1 regarding a very thin mass transport boundary layer.
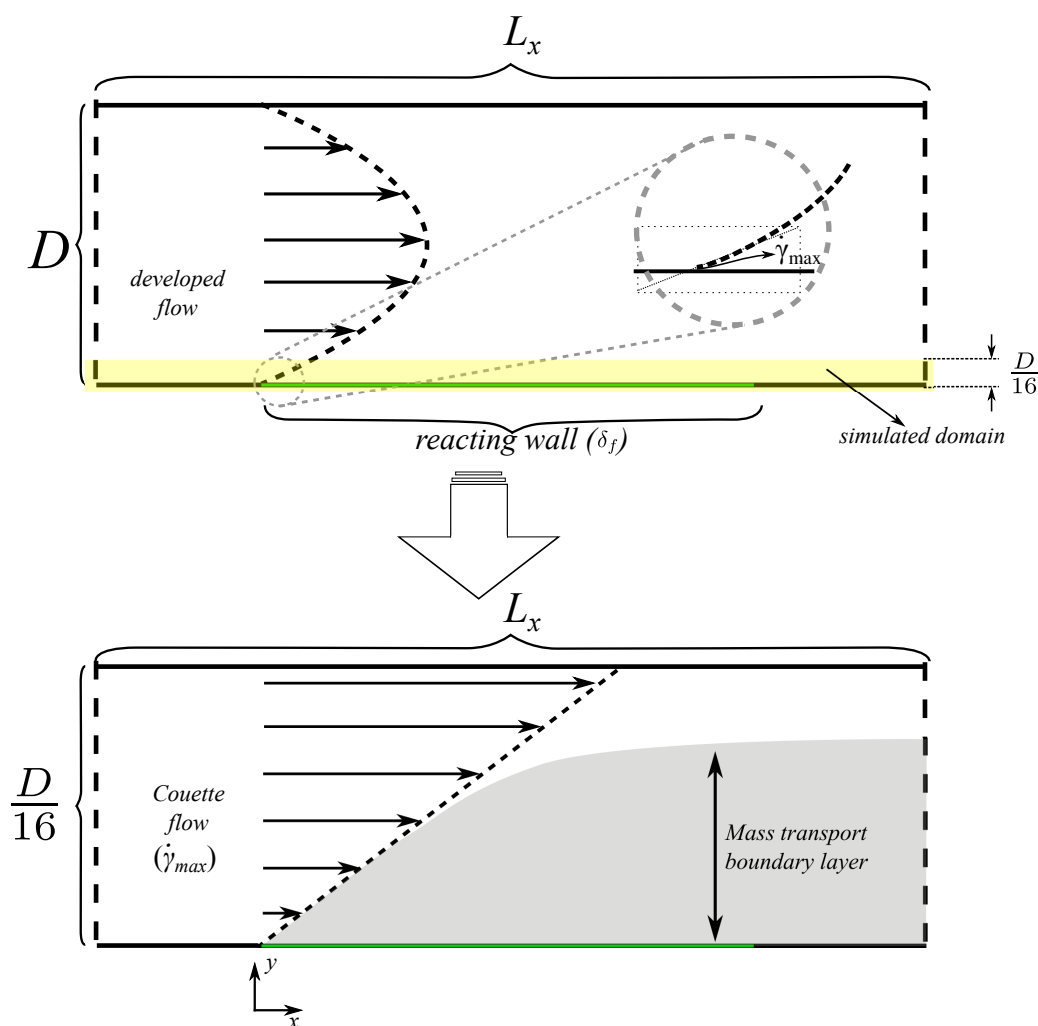
Fig. 5.8 Sketch of the domain reduction. The zoomed inset from the first image displays the wall shear rate, which is the one used for the Couette flow simulation. At the bottom image we describe the dimensions of the simulated physical domain.

As an example of the narrower case of an ill artery, we set up another Couette flow simulation using the enhanced diffusion model (Eq. 2.78) to calculate the real diffusion of the colloidal mixture. As this enhanced diffusion model is shear rate-dependent, the diffusion is kept constant in the whole domain. In order to keep the relaxation time for the concentration within appropriate values, the mesh is refined up to $N = 400$. Additionally, the shear rate is increased by ten times ($\dot{\gamma} = 3800^{-1}$) in order to mimic the same shear rate that would be found in a mildly stenosed artery. To speed up the simulation, the real domain has been reduced eight times with respect to the radius (see Fig. 5.8), so only the closest part to the wall is simulated. By using the enhanced diffusion model (with an homogeneous constant hematocrit of $\phi = 0.45$ for Eq. 2.78), and considering a shear rate of 3800^{-1}, the Schmidt number becomes ≈ 1220. This value represents a value of the diffusivity about 53 times higher than the

Fig. 5.9 Local Sherwood number computed on the active portion of the wall and its analytic solution Eq. 2.84. The Schmidt number is 1220, the Péclet number, based on the shear rate and the reacting surface is around 10000, and the reaction rate is constant, $k_{rt} = 10^{-4} m/s$.

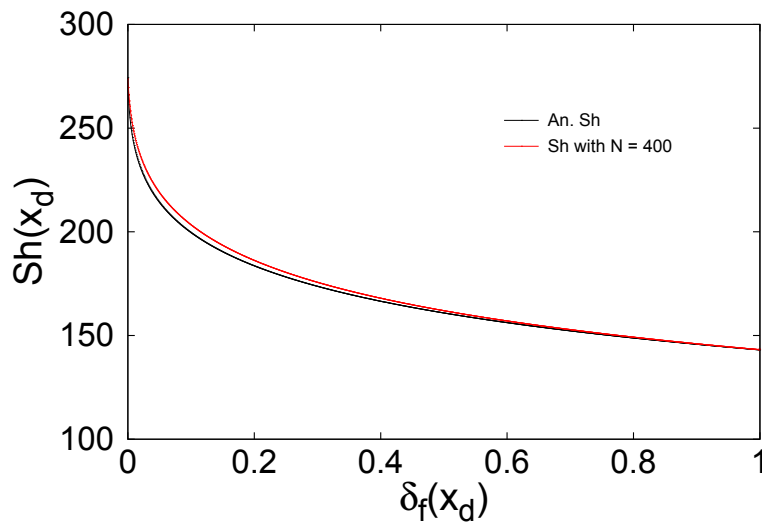previous value set arbitrarily, meaning that the mass transport boundary layer becomes much thinner, which at the same time needs a much higher grid resolution to simulate it. Figure 5.9 shows the increase of the Sherwood number by nearly two orders of magnitude with respect to the previous setup, Fig. 5.7. This is due to the fact that the diffusion coefficient is inversely proportional to the Damkhöler number, which at the same time denotes the reaction rate over the diffusion rate. Additionally, the shear rate increment also enhances the flow advection, and thus, the mass transfer rate at the wall is favoured with higher shear rates. The relative error for the averaged Sherwood number does not exceed the 0.93%. The accuracy in this latter case is remarkable as we are pushing the simulation to the relaxation time limits ($\tau \approx 0.5003$) and we have not increased the mesh resolution proportionally to the boundary layer thickness reduction ($Re_{\delta_f} Sc^{1/2} \approx 10^4$).

One has to note that, from this latter conditions of the model, we were able to significantly reduce the amount of physical domain space. This can only be done under the Couette flow assumption plus the fact that we should have enough vertical space to correctly develop the mass transport boundary layer. On the other hand, if we keep the enhanced diffusion model on Eq. 2.78, we will not be able to reduce the boundary layer any further, and thus we will not be able to crop the physical domain from this latter point. The reason behind this issue is the dual dependence of the mass transport boundary layer with both the shear rate and the diffusion coefficient. For the considered conditions, Pallarès and Grau [57] propose an estimation of the mass
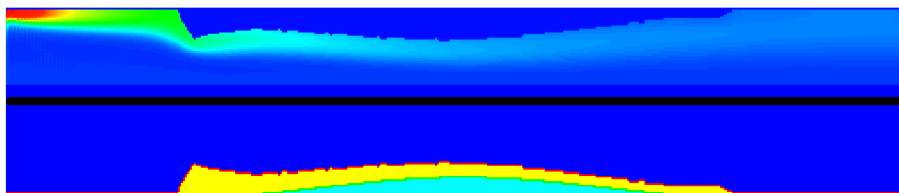
Fig. 5.10 Output from a growth simulation with the computational region algorithm. Arbitrary simulation with two divided contours: upper half shows a concentration contour with blue to red (low to high) colour code; the lower half shows the different computational regions. The yellow coloured region is the formed thrombus. Cyan coloured part is the stenosed region. Red surface is the liquid phase attached to a solid wall. Green surface is the solid wall attached to a liquid phase.

transport boundary layer thickness (Eq. 5.4). We can see that if we increase the shear rate, automatically, the diffusion will be proportionally increased by the same amount (the thermal diffusion on Eq. 2.78 is negligible).

$$\delta_c \approx \left(\frac{\delta_f D}{S} \right)^{\frac{1}{3}} \tag{5.4}$$

5.5 Computational Region Algorithm

We perform a simulation test with the computational region algorithm explained at Sec. 2.5.3 to prove that the algorithm works properly. Figure 2.7 displays a preliminary simulation output that shows the growth effect after applying the computational region algorithm with the reaction surface. The output is divided into two separated variable contours. The upper half of the figure displays the concentration contour and the lower half is the region-types contour. Both hydrodynamic and reaction-transport variables are arbitrarily set for this test which its main purpose is to verify that the growth occurs. Additionally, this particular domain has been reduced to the half with a symmetry at the center of the *x*-axis artery with a mild stenosis at the central part of wall the cylinder. The stenosis domain is represented with the cyan coloured part and it is essentially a no-slip wall. The yellow coloured region above the stenosis is the thrombus region that acts as a solid wall and has been formed from the reacted platelets that were close to the surface of the blood vessel or other thrombus.

From Fig. 2.7 one can infer that the computational region works and only will need to be correctly calibrated.

5.6 Conclusions and future work

We presented a work towards the development of an integral growth model in the framework of the Lattice Boltzmann Method. We propose a set of tools and their corresponding validations which include: a passive scalar particle distribution function model, a shear rate-dependent diffusion coefficient model for the species, a proposal for a vertical force term to mimic the margination phenomenon that the platelets experiment on the arteries which is based on a phenomenological model and a steady state validation of a wall surface reaction which could be the initial step to model a thrombosis event.

We have successfully simulated, in a LBM environment, the concentration distribution and the wall mass transfer of a two dimensional channel that has similar physical, hydrodynamic and platelet transport conditions than a human coronary artery.

We have contributed to a more accurate and realistic LBM model for platelet distribution based on the passive scalar approach. As a novelty, we have proposed a method to introduce a lateral drift term for the LBM based in Bark's drift term [38]. This model is not fully satisfactory and presents some limitations. For example, the model requires a predefined potential field, and presents an early wall concentration decay that is gradually corrected, away from the inlet and the outlet. Despite its limitations and with an appropriate conditioning it can maintain a constant peak concentration near the wall even with high concentration gradients. Such gradients would rapidly disperse the near wall-excess platelet concentration towards the uniform solution without the drift term.

The presented results of this part of the thesis, although preliminary, are relevant in numerous fields and can digress from the original thrombus growth model idea of this thesis. If we focus on the validated first order reaction, we can find many medical or industrial applications and other processes that can be simulated with a surface reaction in the LBM hydrodynamic regime. For instance, one could model the electrochemical reactions on the surface of an electrode, a heterogeneous reaction on a catalytic surface or even one can calculate the exchange of chemicals in a biological surface. The versatility of the presented work can be reoriented to the development or improvement of microfluidic devices, such as the surface-based biosensors [63]. Additionally, this surface reaction model can be directly used to test and predict the deposition rate of platelets in other proposed phenomenological models [58].

However, there is still work to do to fulfil the target of developing a growth model. Firstly, we need to improve the performance of the drift term for platelets. From thereon, the model is prepared to computationally implement the clogging/thrombosis process (see Sec. 2.5.3). The model will be no longer reducible (as we have done in

Sec. 5.4) due to the fact that the hydrodynamic field will change in time with the shape of the thrombus/wall, which at the same time will change both the mass transport and hydrodynamic conditions. The full model, supplied with the appropriate parameter values, will demand a significant amount of computational resources. That is why the following step has to be writing the corresponding parallel code, preferably in GPU.

With an effective parallel computing tool, enabling a local refining feature near the mass transport layer, and a fine optimisation of the code, we could have a simple and effective growth model. A long-term goal would be to carry out a parametric study on the dependence of the thrombus production rates as a function of parameters like the shear rate, the kinetic reaction constant rate, the physical degree of stenosis, margination term parameter, etc. Other future ideas include the comparison of the obtained numerical growth rates with other different computational models, such as in Bark et al. [38], or even with *in vitro* [40] or *ex vivo* [4, 5] experiments.

Chapter 6

Conclusions and remarks

We will collect the most important conclusions of the thesis and provide some personal remarks in this chapter.

We have developed a code able to reproduce the Navier-Stokes and the advection-diffusion-reaction governing equations under isothermal flow conditions through the lattice Boltzmann method. The code has been applied to study two different topics.

The first part of the study was devoted to the understanding of the impact of different combinations of inlet/outlet boundary conditions on the forces over a blunt body with different orientations with respect to the main flow direction. The analysis was completed with a full parametric study on different domain dimensions and different Reynolds numbers. The results of using reflective or non-reflective boundary conditions have been reported, highlighting the significant differences shown by the forces exerted on the obstacle. As a novelty (even though it is an ill-posed condition), we have set a non-reflective boundary condition at the inlet by means of a feedback-type algorithm. With this feature, the inlet velocity profile showed minimal deviations from the analytic parabolic flow. We concluded this part of the work by comparing two different non-reflective boundary condition: Thompson BC and LODI BC. Results of this analysis were focused on the outlet of the domain and showed that the Thompson BC provides a better numerical solution when the flow presents a strong two-dimensional movement –for example, this is observed when vortexes are present.

In the second part of the thesis we explored the advantages and limits of the passive scalar modelling of platelets in hemodynamics using the LBM. We ran LBM simulations in a domain that mimics a human coronary artery. The blood flow was simplified by considering the platelets as a continuum. We developed a novel way (and still improvable) to reproduce the platelet migration effect by considering a potential field used in other simulations performed with other CFD methods. We additionally validated both solute transport and surface reaction. The combination of all these

aforementioned implementations with other sophistications reported in Chapter 2 settle the seed to develop an integral growth model in LBM that might be considered as a tool to model thrombosis and other hemodynamics phenomena.

To address the initial objective of the thesis, we derived and presented the fundamental LBM equations and described its origins. Additionally, we studied two topics that are currently under debate: the analysis of the boundary conditions and hemodynamics applications. Both studies were performed within the LBM framework with the aim to bring an added value to their respective topics.

References

[1] Aarts, P. A., van den Broek, S. A., Prins, G. W., Kuiken, G. D., Sixma, J. J., and Heethaar, R. M. (1988). Blood platelets are concentrated near the wall and red blood cells, in the center in flowing blood. *Arteriosclerosis, Thrombosis, and Vascular Biology*, 8(6):819–24.

[2] Andrews, R., Lopez, J., and Berndt, M. (1997). Molecular mechanisms of platelet adhesion and activation. *International Journal of Biochemistry and Cell Biology*, 29(1):91–105.

[3] Apelblat, A. (1980). Mass transfer with a chemical reaction of the first order: Analytical solutions. *The Chemical Engineering Journal*, 19(1):19–37.

[4] Badimon, L., Badimon, J., Galvez, A., Chesebro, J., and Fuster, V. (1986). Influence of arterial damage and wall shear rate on platelet deposition. ex vivo study in a swine model. *Arteriosclerosis*, 6(3):312–320.

[5] Badimon, L., Padro, T., and Vilahur, G. (2012). Extracorporeal assays of thrombosis. *Methods in Molecular Biology*, 788:43–57.

[6] Bark, D. L., Para, A. N., and Ku, D. N. (2012). Correlation of thrombosis growth rate to pathological wall shear rate during platelet accumulation. *Biotechnology and Bioengineering*, 109(10):2642–2650.

[7] Bedekar, A., Pant, K., Ventikos, Y., and Sundaram, S. (2005). A computational model combining vascular biology and haemodynamics for thrombosis prediction in anatomically accurate cerebral aneurysms. *Food and Bioproducts Processing*, 83(2 C):118–126.

[8] Bennett, S. (2013). *A Lattice Boltzmann model for diffusion of binary gas mixtures*. PhD thesis, King's College, Cambridge.

[9] Bernsdorf, J., Harrison, S., Smith, S., Lawford, P., and Hose, D. (2008). Applying the lattice boltzmann technique to biofluids: A novel approach to simulate blood coagulation. *Computers & Mathematics with Applications*, 55(7):1408 – 1414.

[10] Bouzidi, M., Firdaouss, M., and Lallemand, P. (2001). Momentum transfer of a boltzmann-lattice fluid with boundaries. *Physics of Fluids*, 13(11):3452–3459.

[11] Breuer, M., Bernsdorf, J., Zeiser, T., and Durst, F. (2000). Accurate computations of the laminar flow past a square cylinder based on two different methods: Lattice-boltzmann and finite-volume. *International Journal of Heat and Fluid Flow*, 21(2):186–196.

94   References

[12] Chapman, S. and Cowling, T. (1970). *The Mathematical Theory of Non-uniform Gases: An Account of the Kinetic Theory of Viscosity, Thermal Conduction and Diffusion in Gases*. Cambridge Mathematical Library. Cambridge University Press.

[13] Chen, S. and Doolen, G. D. (1998). Lattice boltzmann method for fluid flows. *Annual Review of Fluid Mechanics*, 30(1):329–364.

[14] Cito, S., Mazzeo, M., and Badimon, L. (2013). A review of macroscopic thrombus modeling methods. *Thrombosis Research*, 131(2):116–124.

[15] Crowl, L. and Fogelson, A. (2010). Computational model of whole blood exhibiting lateral platelet motion induced by red blood cells. *International Journal for Numerical Methods in Biomedical Engineering*, 26(3-4):471–487.

[16] d'Humières, D. (2002). Multiple–relaxation–time lattice boltzmann models in three dimensions. *Philosophical Transactions of the Royal Society of London A: Mathematical, Physical and Engineering Sciences*, 360(1792):437–451.

[17] Dodge, J. T., Brown, B. G., Bolson, E. L., and Dodge, H. T. (1992). Lumen diameter of normal human coronary arteries. influence of age, sex, anatomic variation, and left ventricular hypertrophy or dilation. *Circulation*, 86(1):232–246.

[18] d'Humiéres, D. and Ginzburg, I. (2009). Viscosity independent numerical errors for lattice boltzmann models: From recurrence equations to "magic" collision numbers. *Computers & Mathematics with Applications*, 58(5):823 – 840.

[19] Eckstein, E. and Belgacem, F. (1991). Model of platelet transport in flowing blood with drift and diffusion terms. *Biophysical Journal*, 60(1):53–69.

[20] Eckstein, E., Bilsker, D., Waters, C., Kippenhan, J., and Tilles, A. (1987). Transport of platelets in flowing blood. *Annals of the New York Academy of Sciences*, 516:442–452.

[21] Feng, Z.-G. and Michaelides, E. E. (2004). The immersed boundary-lattice boltzmann method for solving fluid–particles interaction problems. *Journal of Computational Physics*, 195(2):602 – 628.

[22] Feng, Z.-G. and Michaelides, E. E. (2005). Proteus: a direct forcing method in the simulations of particulate flows. *Journal of Computational Physics*, 202(1):20 – 51.

[23] Filippova, O. and Hänel, D. (1998). Grid refinement for lattice-bgk models. *Journal of Computational Physics*, 147(1):219 – 228.

[24] Fogelson, A. (1984). A mathematical model and numerical method for studying platelet adhesion and aggregation during blood clotting. *Journal of Computational Physics*, 56(1):111–134.

[25] Gábor, Z. and György, P. (2014). Numerical investigation of the hemostasis process in transient blood flow. *Biomechanica Hungarica*, 7(2):22–28.

[26] Ginzbourg, I. and Adler, P. (1994). Boundary flow condition analysis for the three-dimensional lattice Boltzmann model. *Journal de Physique II*, 4(2):191–214.

[27] Goldsmith, H. (1971). Red cell motions and wall interactions in tube flow. *Federation Proceedings*, 30(5):1578–1590.

[28] Guo, Z., Shi, B., and Zheng, C. (2002). A coupled lattice bgk model for the boussinesq equations. *International Journal for Numerical Methods in Fluids*, 39(4):325–342.

[29] Hänel, D. (2004). *Molekulare Gasdynamik: Einführung in die kinetische Theorie der Gase und Lattice-Boltzmann-Methoden*. Springer Berlin Heidelberg.

[30] Harrison, S., Bernsdorf, J., Hose, D., and Lawford, P. (2008). A lattice boltzmann framework for simulation of thrombogenesis. *Progress in Computational Fluid Dynamics, an International Journal*, 8(1-4):121–128.

[31] Harrison, S., Smith, S., Bernsdorf, J., Hose, D., and Lawford, P. (2007). Application and validation of the lattice boltzmann method for modelling flow-related clotting. *Journal of Biomechanics*, 40(13):3023 – 3028.

[32] He, X. and Luo, L.-S. (1997). Theory of the lattice boltzmann method: From the boltzmann equation to the lattice boltzmann equation. *Phys. Rev. E*, 56:6811–6817.

[33] Heubes, D., Bartel, A., and Ehrhardt, M. (2014). Characteristic boundary conditions in the lattice boltzmann method for fluid and gas dynamics. *Journal of Computational and Applied Mathematics*, 262:51 – 61.

[34] Higuera, F. J., Succi, S., and Benzi, R. (1989). Lattice gas dynamics with enhanced collisions. *EPL (Europhysics Letters)*, 9(4):345.

[35] Izquierdo, S. and Fueyo, N. (2008). Characteristic nonreflecting boundary conditions for open boundaries in lattice boltzmann methods. *Phys. Rev. E*, 78:046707.

[36] Izquierdo, S., Martínez-Lera, P., and Fueyo, N. (2009). Analysis of open boundary effects in unsteady lattice boltzmann simulations. *Computers and Mathematics with Applications*, 58(5):914–921.

[37] Jami, M., Moufekkir, F., Mezrhab, A., Fontaine, J. P., and Bouzidi, M. (2016). New thermal {MRT} lattice boltzmann method for simulations of convective flows. *International Journal of Thermal Sciences*, 100:98 – 107.

[38] Jr., D. B. and Ku, D. N. (2013). Platelet transport rates and binding kinetics at high shear over a thrombus. *Biophysical Journal*, 105(2):502 – 511.

[39] Kam, E., So, R., and Leung, R. (2006). Non-reflecting boundary conditions for one-step lbm simulation of aeroacoustics. volume 1, pages 205–213.

[40] Kulkarni, S., Dopheide, S., Yap, C., Ravanat, C., Freund, M., Mangin, P., Heel, K., Street, A., Harper, I., Lanza, F., and Jackson, S. (2000). A revised model of platelet aggregation. *Journal of Clinical Investigation*, 105(6):783–791.

[41] Ladd, A. J. (1994). Numerical simulations of particulate suspensions via a discretized boltzmann equation. part 1. theoretical foundation. *Journal of Fluid Mechanics*, 271:285–309.

[42] Lallemand, P. and Luo, L.-S. (2000). Theory of the lattice boltzmann method: Dispersion, dissipation, isotropy, galilean invariance, and stability. *Phys. Rev. E*, 61:6546–6562.

[43] Latt, J. (2008). Choice of units in lattice boltzmann simulations.

[44] Liu, Q., He, Y.-L., and Li, Q. (2015). Multiple-relaxation-time lattice boltzmann modeling of incompressible flows in porous media. *Physica A: Statistical Mechanics and its Applications*, 429:215 – 230.

[45] Liu, Q., He, Y.-L., Li, Q., and Tao, W.-Q. (2014). A multiple-relaxation-time lattice boltzmann model for convection heat transfer in porous media. *International Journal of Heat and Mass Transfer*, 73:761 – 775.

[46] Malaspinas, O. (2006). Lattice boltzmann sample, written in fortran 90. http://wiki.palabos.org/numerics:codes.

[47] McNamara, G. R. and Zanetti, G. (1988). Use of the boltzmann equation to simulate lattice-gas automata. *Phys. Rev. Lett.*, 61:2332–2335.

[48] Mei, R., Luo, L.-S., and Shyy, W. (1999). An accurate curved boundary treatment in the lattice boltzmann method. *Journal of Computational Physics*, 155(2):307 – 330.

[49] Mei, R., Yu, D., Shyy, W., and Luo, L.-S. (2002). Force evaluation in the lattice boltzmann method involving curved geometry. *Phys. Rev. E*, 65:041203.

[50] Miller, W., Succi, S., and Mansutti, D. (2001). Lattice boltzmann model for anisotropic liquid-solid phase transition. *Phys. Rev. Lett.*, 86:3578–3581.

[51] Moaty Sayed, A., Hussein, M., and Becker, T. (2010). An innovative lattice boltzmann model for simulating michaelis-menten-based diffusion-advection kinetics and its application within a cartilage cell bioreactor. *Biomechanics and Modeling in Mechanobiology*, 9(2):141–151.

[52] Mostaghimi;, A. F. A. N. J. (2014). Study of curved boundary treatments in lattice boltzmann method.

[53] Moussaoui, M., Mezrhab, A., and Naji, H. (2011). A computation of flow and heat transfer past three heated cylinders in a vee shape by a double distribution mrt thermal lattice boltzmann model. *International Journal of Thermal Sciences*, 50(8):1532 – 1542.

[54] Najafi-Yazdi, A. and Mongeau, L. (2012). An absorbing boundary condition for the lattice boltzmann method based on the perfectly matched layer. *Computers and Fluids*, 68:203–218.

[55] Okajima, A., Yi, D., Sakuda, A., and Nakano, T. (1997). Numerical study of blockage effects on aerodynamic characteristics of an oscillating rectangular cylinder. *Journal of Wind Engineering and Industrial Aerodynamics*, 67-68:91–102.

[56] Ouared, R. and Chopard, B. (2005). Lattice boltzmann simulations of blood flow: Non-newtonian rheology and clotting processes. *Journal of Statistical Physics*, 121(1):209 – 221.

[57] Pallarès, J. and Grau, F. (2014). Mass transfer rate of a first-order chemical reaction on a wall at high schmidt numbers. *International Journal of Heat and Mass Transfer*, 69:438–442.

[58] Pallarès, J., Senan, O., Guimerà, R., Vernet, A., Aguilar-Mogas, A., Vilahur, G., Badimon, L., Sales-Pardo, M., and Cito, S. (2015). A comprehensive study on different modelling approaches to predict platelet deposition rates in a perfusion chamber. *Scientific Reports*, 5.

[59] Rahmati, A. R., Ashrafizaadeh, M., and Shirani, E. (2014). A multi-relaxation-time lattice boltzmann method on non-uniform grids for large eddy simulation of rayleigh-bénard convection using two sub-grid scale models. *Journal of Applied Fluid Mechanics*, 7(1):89–102.

[60] Samady, H., Eshtehardi, P., McDaniel, M. C., Suo, J., Dhawan, S. S., Maynard, C., Timmins, L. H., Quyyumi, A. A., and Giddens, D. P. (2011). Coronary artery wall shear stress is associated with progression and transformation of atherosclerotic plaque and arterial remodeling in patients with coronary artery disease. *Circulation*, 124(7):779–788.

[61] Schlaffer, M. B. (2013). *Non-reflecting Boundary Conditions for the Lattice Boltzmann Method*. PhD thesis, Technische Universität München, Ingenieurfakultät Bau Geo Umwelt.

[62] Sohankar, A., Norberg, C., and Davidson, L. (1998). Low-reynolds-number flow around a square cylinder at incidence: Study of blockage, onset of vortex shedding and outlet boundary condition. *International Journal for Numerical Methods in Fluids*, 26(1):39–56.

[63] Squires, T., Messinger, R., and Manalis, S. (2008). Making it stick: Convection, reaction and diffusion in surface-based biosensors. *Nature Biotechnology*, 26(4):417–426.

[64] Succi, S. (2001). *The lattice Boltzmann equation: for fluid dynamics and beyond*. Oxford university press.

[65] Suiker, A. S. and Chang, C. S. (2000). Application of higher-order tensor theory for formulating enhanced continuum models. *Acta Mechanica*, 142(1-4):223–234.

[66] Tekitek, M., Bouzidi, M., Dubois, F., and Lallemand, P. (2009). Towards perfectly matching layers for lattice boltzmann equation. *Computers and Mathematics with Applications*, 58(5):903–913.

[67] Thompson, K. (1987). Time dependent boundary conditions for hyperbolic systems. *Journal of Computational Physics*, 68(1):1–24.

[68] Tilles, A. W. and Eckstein, E. C. (1987). The near-wall excess of platelet-sized particles in blood flow: Its dependence on hematocrit and wall shear rate. *Microvascular Research*, 33(2):211 – 223.

[69] Turitto, V. T., Benis, A. M., and Leonard, E. F. (1972). Platelet diffusion in flowing blood. *Industrial & Engineering Chemistry Fundamentals*, 11(2):216–223.

[70] Wang, J., Wang, D., Lallemand, P., and Luo, L.-S. (2013). Lattice boltzmann simulations of thermal convective flows in two dimensions. *Computers & Mathematics with Applications*, 65(2):262 – 286.

[71] Wang, N.-H. L. and Keller, K. (1985). Augmented transport of extracellular solutes in concentrated erythrocyte suspensions in couette flow. *Journal of Colloid and Interface Science*, 103(1):210 – 225.

[72] Wooton, D. M. (1998). *Mechanistic modeling of occlusive arterial thrombosis*. PhD thesis, Georgia Institute of technology.

[73] X. Nie, X. Shan, H. C. (2009). A lattice-boltzmann / finite-difference hybrid simulation of transonic flow.

[74] Xu, Z., Kamocka, M., Alber, M., and Rosen, E. D. (2011). Computational approaches to studying thrombus development. *Arteriosclerosis, Thrombosis, and Vascular Biology*, 31(3):500–505.

[75] Yang, Z. (2007). *Analysis of Lattice Boltzmann Boundary Conditions*. PhD thesis, Universität Konstanz, Konstanz.

[76] Yoon, D.-H., Yang, K.-S., and Choi, C.-B. (2010). Flow past a square cylinder with an angle of incidence. *Physics of Fluids*, 22(4):1–12.

[77] Yoon, H., Kang, Q., and Valocchi, A. J. (2015). Lattice boltzmann-based approaches for pore-scale reactive transport. *Reviews in Mineralogy and Geochemistry*, 80(1):393–431.

[78] Yu, D., Mei, R., and Shyy, W. (2003). A Unified Boundary Treatment in Lattice Boltzmann Method.

[79] Zou, Q. and He, X. (1997). On pressure and velocity boundary conditions for the lattice boltzmann bgk model. *Physics of Fluids*, 9(6):1591–1598.

[80] Zydney, A. L. and Colton, C. K. (1988). Augmented solute transport in the shear flow of a concentrated suspension. *PCH. Physicochemical hydrodynamics*, 10(1):77–96.